

1  
2

CONNECTING OBSERVED MICROBURST PRECIPITATION WITH ITS  
SCATTERING MECHANISM

3

by

Mykhaylo Sergeevich Shumko

4

A dissertation submitted in partial fulfillment  
of the requirements for the degree

of

Doctor of Philosophy

in

Physics

5

MONTANA STATE UNIVERSITY  
Bozeman, Montana

October 2019

6

7

©COPYRIGHT

8

by

Mykhaylo Sergeevich Shumko

2019

All Rights Reserved

## DEDICATION

<sup>9</sup> I dedicate this to all MSU students who use L<sup>A</sup>T<sub>E</sub>X. Dedication is optional  
<sup>10</sup> and may be no longer than one page, single spaced, and should precede the  
<sup>11</sup> acknowledgments page.

## ACKNOWLEDGEMENTS

<sup>12</sup> I would like acknowledge the countless engineers, technicians, and scientists who  
<sup>13</sup> made the FIREBIRD, AC-6, and RBSP missions a success. This work was supported  
<sup>14</sup> by Montana State University and by NASA Headquarters under the NASA Earth and  
<sup>15</sup> Space Science Fellowship Program - Grant 80NSSC18K1204. **Add co-author support.**

## TABLE OF CONTENTS

16	1. INTRODUCTION .....	1
17	Charged Particle Motion in Electric and Magnetic Fields .....	2
18	Particle Populations and Their Interractions in the Magnetosphere .....	8
19	Inner Magnetosphere Populations.....	11
20	Plasmasphere.....	13
21	Ring Current .....	15
22	Radiation Belts.....	16
23	Radiation Belt Particle Sources and Sinks .....	20
24	Adiabatic Heating .....	20
25	Wave Resonance Heating .....	21
26	Particle Losses .....	25
27	Microbursts .....	26
28	Scope of Reserach .....	29
29	2. CHAPTER TWO	
30	EVIDENCE OF MICROBURSTS OBSERVED NEAR THE EQUA-	
31	TORIAL PLANE IN THE OUTER VAN ALLEN RADIATION	
32	BELT .....	31
33	Contribution of Authors and Co-Authors .....	31
34	Manuscript Information .....	32
35	Key Points .....	33
36	Abstract .....	33
37	Introduction .....	33
38	Spacecraft Instrumentation .....	36
39	Observations .....	37
40	Analysis .....	40
41	Microburst and Source PSD .....	40
42	Motion of resonant electrons in phase space .....	43
43	Comparing the microburst PSD to diffusion theory .....	46
44	Discussion and Conclusions .....	48
45	Acknowledgments .....	49
46	3. CHAPTER THREE	
47	MICROBURST SCALE SIZE DERIVED FROM MULTIPLE BOUNCES	
48	OF A MICROBURST SIMULTANEOUSLY OBSERVED WITH	
49	THE FIREBIRD-II CUBESATS .....	51
50	Contribution of Authors and Co-Authors .....	51

## TABLE OF CONTENTS – CONTINUED

51	Manuscript Information .....	52
52	Key Points .....	53
53	Abstract .....	53
54	Introduction .....	54
55	Spacecraft and Observation .....	56
56	Analysis.....	59
57	Electron Bounce Period .....	60
58	Microburst Energy Spectra .....	62
59	Microburst Scale Sizes .....	62
60	Discussion and Conclusions .....	65
61	Acknowledgments .....	67
62	4. CHAPTER FOUR	
63	MICROBURST SIZE DISTRIBUTION DERIVED WITH AEROCUBE-	
64	6 .....	68
65	Contribution of Authors and Co-Authors .....	68
66	Manuscript Information .....	69
67	5. CONCLUSIONS AND FUTURE WORK .....	70
68	REFERENCES CITED.....	71
69	APPENDIX: Appendix A.....	80
70	APPENDIX: Appendix B .....	83

## LIST OF FIGURES

Figure	Page
71      1.1 The three periodic motions of charged particles 72      in Earth's dipole magnetic field. These motions 73      are: gyration about the magnetic field line, bounce 74      motion between the magnetic poles, and azimuthal 75      drift around the Earth. Figure from (Baumjohann 76      and Treumann, 1997). ....	2
77      1.2 Charged particle motion in a uniform magnetic field 78 $\vec{B}$ . Panel (A) shows the geometry defining the 79      pitch angle, $\alpha$ . Panel (B) and (C) show two helical 80      electron trajectories with dashed lines assuming a 81      large and small $\alpha$ (corresponding to a small and large 82      parallel velocity $v_{  }$ ), respectively. ....	6
83      1.3 Contours of constant gyration, bounce, and drift 84      frequencies for electrons and protons in a dipole field. 85      Figure from Schulz and Lanzerotti (1974). ....	7
86      1.4 Macroscopic structures in the outer magnetosphere. 87      The solar wind with its frozen-in interplanetary 88      magnetic field is shown on the left and is traveling 89      supersonically towards the right. The solar wind 90      envelops Earth's magnetic field to create the mag- 91      netosphere cavity. Since the solar wind is traveling 92      supersonically, it creates a bow shock up stream. 93      Downstream of the bow shock the shocked solar wind 94      plasma inside the magnetosheath flows around the 95      magnetopause, a boundary between the solar wind 96      and magnetosphere. Figure from Baumjohann and 97      Treumann (1997). ....	9
98      1.5 Macroscopic structures in the inner magnetosphere 99      most relevant to this dissertation. The plasmas- 100     phere, and the radiation belts are shown and ring 101     current is co-located there as well. Sun is to the left. 102     Figure from Baumjohann and Treumann (1997). ....	10
103     1.6 The series of steps involved in magnetic reconnection 104     with a southward IMF. Figure from Baumjohann 105     and Treumann (1997). ....	12

## LIST OF FIGURES – CONTINUED

Figure	Page
106      1.7 Equipotential lines and electric field arrows due to 107      the superposition of the co-rotation and convection 108      electric fields. Electrons in the shaded region execute 109      closed orbits. Outside of the shaded regions the 110      electrons are not trapped and will escape. The 111      region separating the two regimes is called the Alfvén 112      layer. Figure from Baumjohann and Treumann (1997).....	14
113      1.8 The DST index during the St. Patrick's Day 2015 114      storm. This storm was caused by a coronal mass 115      ejection on March 15th, 2015. The storm phases 116      are: initial phase, main phase, and recovery phase. 117      The initial phase occurred when the Dst peaked at 118      +50 nT on March 17th during which the ring current 119      was eroded by the coronal mass ejection during the 120      interval shown by the red bar. Then the rapid 121      decrease to $\approx -200$ nT was during the main phase 122      where many injections from the magnetotail pumped 123      up the ring current which reduced Earth's magnetic 124      field strength at the ground and is shown with the 125      green bar. Lastly, the recovery phase lasted from 126      March 18th to approximately March 29th during 127      which the ring current particles were lost and the 128      ring current returned to its equilibrium state. The 129      recovery phase is shown with the blue bar.....	17
130      1.9 The two radiation belts with a the locations of 131      various satellites and orbits. Figure from (Horne 132      et al., 2013). .....	18
133      1.10 The dynamics of the outer radiation belt in 1997 134      from the POLAR satellite. Top panel shows the 1.2- 135      2.4 MeV electron flux as a function of L and 1997 day 136      of year. The middle panel shows the DST index, and 137      bottom panel shows the solar wind velocity. Figure 138      from (Reeves et al., 2003). .....	19

## LIST OF FIGURES – CONTINUED

Figure	Page
139      1.11 The trajectories of an electron and a right-hand circularly polarized wave during a cyclotron resonance. The electron's $v_{\parallel}$ and the wave's $k_{\parallel}$ are in opposite directions such that the wave's frequency is Doppler shifted to an integer multiple of the electron cyclotron frequency. Figure from (Tsurutani and Lakhina, 1997). ....	22
140 141 142 143 144      1.12 Various wave modes in the magnetosphere. Ultra low frequency waves occur throughout the magnetosphere. Chorus waves are typically observed in the 0-12 midnight-dawn region. EMIC waves are typically observed in the dusk MLT sector. Hiss waves are observed inside the plasmasphere. Figure from Millan and Thorne (2007). ....	24
152 153 154 155 156 157 158      1.13 An example train of microbursts observed by FIREBIRD-II unit 4 on February 2nd, 2015. The colored curves show the differential energy channel count rates in six channels from $\approx 200$ keV to greater than 1 MeV. The x-axis labels show auxiliary information such as time of observation and the spacecraft position in L, MLT, latitude and longitude coordinates. ....	27
159 160 161 162 163 164 165      1.14 Relativistic ( $> 1$ MeV) distribution of microburst occurrence rates as a function of L and MLT. The three panels show the microburst occurrence rate dependence on geomagnetic activity, parameterized by the auroral electrojet (AE) index for (a) $AE < 100$ nT, (b) $100 < AE < 300$ nT and (c) $AE > 300$ nT. Figure from Douma et al. (2017)....	28

## LIST OF FIGURES – CONTINUED

Figure	Page
166      2.1 Electron and wave conditions from the MagEIS-A 167      and EMFISIS WFR sensors for the microburst time 168      interval. Panels (a), (b), and (c) are from RBSP-A 169      with its position information annotated in panel (a). 170      Panels (d), (e), and (f) are from RBSP-B with its 171      position information annotated in panel (d). Panel 172      (a) is the MagEIS-A high rate timeseries. Panels (b) 173      and (e) show the evolution of the MagEIS-A $J$ as a 174      function of $\alpha_L$ from the $\sim 40$ to $\sim 60$ keV channel. 175      Every 10th point is shown in panel (b). The solid 176      black line in panels (a) and (b) mark the end of 177      the time period used for the PSD fit extrapolation 178      analysis explained in section 3. The dashed black 179      lines in panels (a) and (b) show the time interval 180      used for the observed microburst PSD. Panels (c) 181      and (f) show the EMFISIS WFR spectra, with the 182      available burst data superposed. The red, green, and 183      cyan traces are equatorial $f_{ce0}$ , $f_{ce0}/2$ , and $f_{ce0}/10$ , 184      respectively. ....	39
185      2.2 Panel (a) shows the MagEIS-A high rate timeseries. 186      Panel (b) shows the RBSPICE EBR count rate 187      timeseries for $\zeta 19$ keV electrons. The microbursts 188      were observed between 11:17:10 - 11:17:12 UT and 189      are indicated with the vertical black arrows in panels 190      (a) and (b) for MagEIS-A times. Panel (c) shows the 191      RBSPICE EBR (family of relatively sparse sampled 192      curves) and MagEIS-A $J$ from the 29-41 keV energy 193      channel (single curve) as a function of $\alpha_L$ . The 194      vertical dashed lines show the time interval for the 195      PSD analysis.....	41

## LIST OF FIGURES – CONTINUED

Figure	Page
196      2.3 The colored annulus represents $f(p_\perp, p_{\parallel})$ in normalized momentum space, parallel and perpendicular to the background magnetic field. The microburst $f(p_\perp, p_{\parallel})$ is highlighted with the white circle. The columns show different powers of the sine extrapolation, and rows show the different magnetic latitudes of the scattering. The white dotted traces represent the boundary between the data and extrapolation. The green, red, and white solid traces are the resonance curves for $\omega = 0.2\Omega_{ce}$ , $0.4\Omega_{ce}$ , $0.6\Omega_{ce}$ , respectively. The cyan dashed traces are the diffusion curves for a $\omega = 0.4\Omega_{ce}$ wave (waves of other frequency have similar diffusion curves). The magnetic latitude of the scattering, the ratio of the plasma to the cyclotron frequency, and the power of the sine extrapolation is annotated in each panel. For the resonance and diffusion curves, the density model assumed a $n_L = 1 e^-/cm^3$ and $\psi = -1$ .....	44
214      3.1 HiRes data of the microburst observed at February 2nd, 2015 at 06:12:53 UT, smoothed with a 150 ms rolling average. The subsequent bounces showed some energy dispersion. As discussed in Appendix B, a time correction of -2.28 s was applied to FU3. While the flux from five energy channels is shown, only channels with reasonable counting statistics were used for the spatial scale analysis. Vertical colored bars show the $\sqrt{N}$ error every 10th data point and vertical black bars are lined up with the peaks in the 220-283 keV energy channel to help identify dispersion.	58

## LIST OF FIGURES – CONTINUED

Figure	Page
226      3.2 Observed and theoretical $t_b$ for electrons of energies 227 from 200 to 770 keV. The solid black line is $t_b$ 228 in a dipole magnetic field, derived in Schulz and 229 Lanzerotti (1974). The red dotted and cyan dashed 230 lines are the $t_b$ derived using the T89, and T04 231 magnetic field models with IRBEM-Lib. Lastly, 232 the blue dot-dash curve is the $t_b$ derived using the 233 Olson & Pfitzer Quiet model. The green and purple 234 rectangles represent the observed $t_b$ for FU3 and 235 FU4 using a Gaussian fit, respectively. The blue 236 rectangles represent the observed $t_b$ calculated with 237 the minima between the bounces. The width of the 238 boxes represent the width of those energy channels, 239 and the height represents the uncertainty from the fit.....	61
240      3.3 The topology of the FIREBIRD-II orbit and the 241 multiple bounces of the microburst projected onto 242 latitude and longitude with axis scaled to equal 243 distance. Attributes relating to FU3 shown in red 244 dashed lines, and FU4 with blue solid lines. The 245 spacecraft path is shown with the diagonal lines, 246 starting at the upper right corner. The labels P1- 247 4 for FU4 and P1-5 for FU3 indicate where the 248 spacecraft were when the $N^{th}$ peak was seen in 249 the lowest energy channel in the HiRes data. The 250 stars with the accompanying energy labels represent 251 the locations of the electrons with that energy that 252 started at time of P1, and were seen at the last peak 253 on each spacecraft. The rectangles represent the 254 lower bound of the microburst scale size, assuming 255 that the majority of the electrons were in the upper 256 boundary of energy channel 4.....	64

## LIST OF FIGURES – CONTINUED

Figure	Page
257 A.1 Panel (A) shows the magnetic power spectral density 258 as a function of frequency and time from the EMFI- 259 SIS WFR instrument on board RBSP-A. The “hiss- 260 like” wave used for the resonant diffusion analysis 261 was observed starting at 11:17:03 UT. In the same 262 format as panel (A), panel (B) shows the polar angle 263 of the wave vector for this time period. The wave 264 of interest had a normal wave vector, $\theta_k < 30^\circ$ . 265 Since the results in panel (B) are valid only for high 266 planarity, panel (C) shows planarity in the same 267 format as panels (A) and (B). The wave of interest 268 was found to have a planarity of $> 0.8$ . Lastly, panel 269 (D) shows the available burst mode data. ....	81
270 A.2 Ratio of the RBSPICE EBR at microburst times 271 indicated with the black vertical arrows in Fig. 2, 272 to the EBR at the same pitch angles one spin prior 273 (quiet time). The microburst flux was enhanced by 274 10-80% across $100^\circ < \alpha_L < 160^\circ$ PA, and appear to 275 be peaked closer to $\alpha_L = 90^\circ$ ....	82
276 B.1 Cross-correlation time lag analysis applied to a train 277 of microbursts. Panel (a) and (b) show the count 278 rate from the lowest energy channel. Panel (c) shows 279 the cross-correlation coefficient as a function of time 280 lag. Panel (d) shows the shifted timeseries. Clock 281 difference was 2.23 s. ....	85
282 B.2 Same analysis as Fig. B.1 on a different time period. 283 Clock difference was 2.21 s. ....	86
284 B.3 Same analysis as Fig. B.1 on a different time period. 285 Clock difference was 2.25 s. ....	87
286 B.4 Same analysis as Fig. B.1 on a different time period. 287 Clock difference was 2.27 s. ....	88

## LIST OF FIGURES – CONTINUED

Figure		Page
288	B.5 Same cross-correlation time lag analysis applied to	
289	stationary spatial structures. The cross-correlation	
290	lag between these events is a sum of the clock differ-	
291	ence and time lag due to the spacecraft separation.	
292	The lag derived at this time was 4.95 s.....	89
293	B.6 Same analysis as Fig. B.5 applied to a different	
294	stationary spatial feature. The lag derived at this	
295	time was 5.01 s. ....	90

## NOMENCLATURE

$L$	L-Shell
$MLT$	magnetic local time
$\lambda$	magnetic latitude
$\alpha$	pitch angle
$\alpha_L$	local pitch angle at the spacecraft
$\alpha_{eq}$	pitch angle maped to the magnetic equator
$c$	speed of light
$R_E$	Earth's radius
$J$	flux
$f$	phase space density
$E$	energy
$E_0$	exponential e-folding energy
$p$	momentum
$\vec{E}$	electric field
$\vec{B}$	magnetic field
$B_w$	wave amplitude
$v$	velocity
$\Omega_e$	electron gyrofrequency
$\omega_{pe}$	plasma frequency
$k$	wave vector
$D_{xx}$	diffusion coefficient
$s$	spacecraft separation
$t_b$	electron bounce period

296

297

## INTRODUCTION

298        Above Earth's atmosphere are the a pair of Van Allen radiation belts, a complex  
299        and dynamic plasma environment that effects our technology-driven society. These  
300        effects include: a higher radiation dose for astronauts and cosmonauts, higher chance  
301        of spacecraft failure due to single event upsets that can lead to catastrophic latchups,  
302        degradation of silicon (changing the silicon doping) from an extended radiation dose  
303        that can degrade a transistor to the point where it no longer function as a switch,  
304        and the degradation of the ozone layer due to the chemical production of  $\text{NO}_X$  and  
305         $\text{HO}_X$  molecules. With these effects in mind, it is no surprise that the radiation belts  
306        have been extensively studied since their discovery in the 1960s.

307        One natural phenomenon in the radiation belts that has been a topic of interest  
308        in the space physics community is wave-particle intersections that, as we will explore  
309        throughout this dissertation, can accelerate particles to very high energies (e.g.  $\approx$   
310        MeV for electrons) and scatter them into the atmosphere.

311        The goal of this dissertation is to study the wave-particle mechanism that  
312        scatters microbursts, a sub-second impulse of electrons into Earth's atmosphere.  
313        Before we dive deep into the physics of wave-particle interactions, an introduction to  
314        Earth's magnetosphere is warranted. Single charged particle motion in Earth's electric  
315        and magnetic fields will be described first. Then the major particle populations in  
316        the magnetosphere and the coupling between them will be described. Lastly, a brief  
317        overview of wave-particle interactions and their effects will be presented.

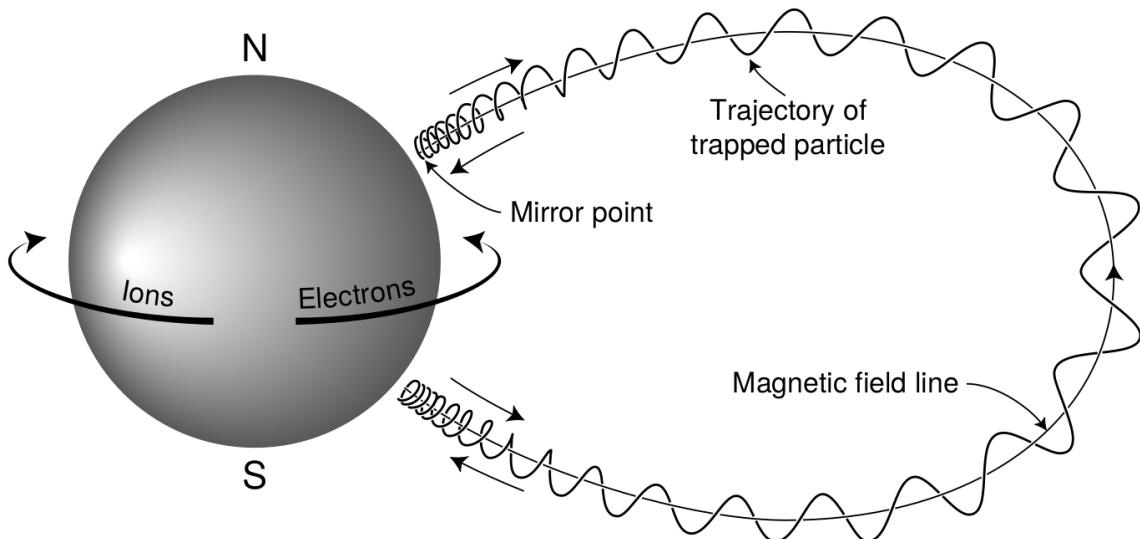


Figure 1.1: The three periodic motions of charged particles in Earth's dipole magnetic field. These motions are: gyration about the magnetic field line, bounce motion between the magnetic poles, and azimuthal drift around the Earth. Figure from (Baumjohann and Treumann, 1997).

318

### Charged Particle Motion in Electric and Magnetic Fields

A charged particle trapped in the magnetosphere will experience three types of periodic motion in Earth's nearly dipolar magnetic field. The three motions are ultimately due to the Lorentz force that a particle of momentum  $\vec{p}$ , charge  $q$ , and velocity  $\vec{v}$  experiences in an electric field  $\vec{E}$  and magnetic field  $\vec{B}$  and is given by

$$\frac{d\vec{p}}{dt} = q(\vec{E} + \vec{v} \times \vec{B}). \quad (1.1)$$

- 319 In the magnetosphere, the three periodic motions in decreasing frequency are gyration,
- 320 bounce, and drift and are schematically shown in Fig. 1.1. Each of these
- 321 motions have a corresponding conserved quantity i.e. an adiabatic invariant.

The highest frequency periodic motion is gyration about a magnetic field of

magnitude  $B$ . This motion is circular with a Larmor radius of

$$r = \frac{mv_{\perp}}{|q|B} \quad (1.2)$$

where  $m$  is the mass and  $v_{\perp}$  the particle's velocity perpendicular to  $\vec{B}$ . This motion has a corresponding gyrofrequency

$$\Omega = \frac{|q|B}{m} \quad (1.3)$$

in units of radians/second. Inside the radiation belts the electron gyrofrequency,  $\Omega_e$  is on the order of a kHz. The corresponding adiabatic invariant is found by integrating the particle's canonical momentum around the particle's path of gyration

$$J_i = \oint (\vec{p} + q\vec{A}) \cdot d\vec{l} \quad (1.4)$$

where  $J_i$  is the  $i^{th}$  adiabatic invariant and  $\vec{A}$  is the magnetic vector potential. This integral is carried out by integrating the first term over the circumference of the gyro orbit and integrating the second term using Stokes theorem to calculate the magnetic flux enclosed by the gyro orbit. With suitable integration,  $J_1 \sim v_{\perp}^2/B$  and is conserved as the frequency of the driving force,  $\omega$  satisfies  $\omega \ll \Omega_e$ .

The second highest frequency periodic motion is bouncing due to a parallel gradient in  $\vec{B}$ . This periodic motion naturally arises in the magnetosphere because Earth's magnetic field is stronger near the poles, and artificially in the laboratory in magnetic bottle machines. To understand this motion we first we need to define the concept of pitch angle  $\alpha$  as the angle between  $\vec{B}$  and  $\vec{v}$  which is schematically shown in Fig. 1.2a. The pitch angle relates  $v$  with  $v_{\perp}$ , and  $v_{||}$  (the component of the particles velocity parallel to  $\vec{B}$ ). As shown in 1.2b and c, a larger  $\alpha$  will tighten the

<sup>334</sup> particle's helical trajectory and vice versa.

Assuming the particle's kinetic energy is concerned, the conservation of  $J_1$  implies that given a particle's  $v_{\perp}(0)$  and  $B(0)$  at the magnetic equator (where Earth's magnetic field is usually at a minimum), we can calculate its  $v_{\perp}(s)$  along the particle's path  $s$  by calculating  $B(s)$  from magnetic field models. The particle's perpendicular velocity is then related via

$$\frac{v_{\perp}^2(0)}{B(0)} = \frac{v_{\perp}^2(s)}{B(s)} \quad (1.5)$$

<sup>335</sup> which can be rewritten as

$$\frac{v^2 \sin^2 \alpha(0)}{B(0)} = \frac{v^2 - v_{\parallel}^2(s)}{B(s)} \quad (1.6)$$

<sup>336</sup> and re-arranged to solve for  $v_{\parallel}(s)$

$$v_{\parallel}(s) = v \sqrt{1 - \frac{B(s)}{B(0)} \sin^2 \alpha(0)} \quad (1.7)$$

<sup>337</sup> which will tend towards 0 when the second term in the radical approaches 1.

<sup>338</sup> The location where  $v_{\parallel}(s) = 0$  is called the mirror point and is where a particle  
<sup>339</sup> stops and reverses direction. Since Earth's magnetic field is stronger towards the  
<sup>340</sup> poles, the mirroring particle will execute periodic bounce motion between its two  
<sup>341</sup> mirror points in the northern and southern hemispheres. The corresponding adiabatic  
<sup>342</sup> invariant,  $J_2$  is

$$J_2 = \oint p_{\parallel} ds \quad (1.8)$$

where  $ds$  describes the particle path between the mirror points in the northern and southern hemispheres (see Fig. 1.1).  $J_2$  is found by substituting Eq. 1.7 into Eq. 1.8 and defining the magnetic field strength at the mirror points as  $B_m$  where  $\alpha(m) = 90^\circ$ .

The  $J_2$  integral can be written as

$$J_2 = 2p \int_{m_n}^{m_s} \sqrt{1 - \frac{B(s)}{B(m)}} ds \quad (1.9)$$

343 where  $m_n$  and  $m_s$  are the northern and southern mirror points, respectively. The  
 344 bounce period can be estimated (e.g. Baumjohann and Treumann, 1997) to be

$$t_b \approx \frac{LR_e}{\sqrt{W/m}} (3.7 - 1.6 \sin \alpha(0)) \quad (1.10)$$

345 where  $L$  is the  $L$ -shell which describes the distance from the Earth's center to the  
 346 location where a particular magnetic field line crosses the magnetic equator, in units  
 347 of Earth radii,  $R_e$ .  $W$  is the particle's kinetic energy. As with gyration, a particle  
 348 bounces as long as  $\omega \ll \Omega_b$ , where  $\Omega_b$  is the bounce frequency.

349 At this stage it is instructional to introduce the notion of the loss cone pitch  
 350 angle,  $\alpha_L$ . A particle with  $\alpha \leq \alpha_L$  will mirror at or below  $\approx 100$  km altitude in the  
 351 atmosphere. A particle at those altitudes will encounter Earth's atmosphere and has  
 352 a significant probability of Coulomb scattering with atmospheric particles and be lost  
 353 to the atmosphere.

354 The slowest periodic motion experienced by charged particles in Earth's mag-  
 355 netic field is azimuthal drift around the Earth. This drift results from a combination of  
 356 a radial gradient in  $\vec{B}$  and the curvature of the magnetic field. The radial gradient drift  
 357 arises because Earth's magnetic field is stronger near the Earth where the particle's  
 358 gyroradius radius of curvature is smaller as it gyrates towards stronger magnetic field,  
 359 and larger when it gyrates outward. The overall effect is the particle gyro orbit does  
 360 not close on itself and negatively charged particles drift East and positively charged  
 361 particles drift West. The radial gradient drift is enhanced by the centrifugal force that  
 362 a particle experiences as it bounces along the curved field lines. The drift adiabatic

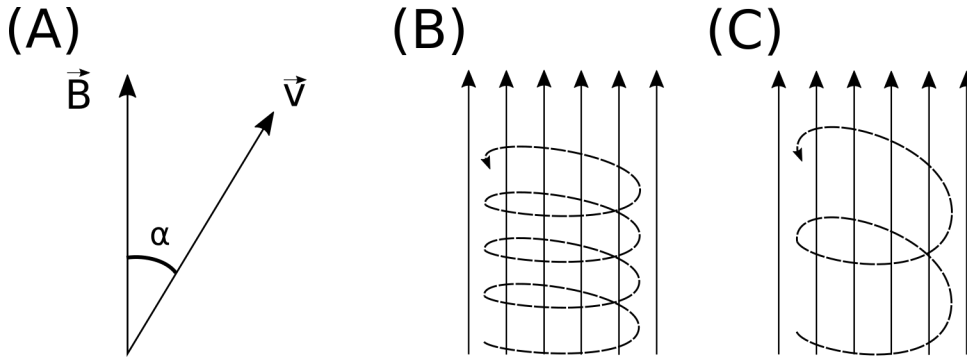


Figure 1.2: Charged particle motion in a uniform magnetic field  $\vec{B}$ . Panel (A) shows the geometry defining the pitch angle,  $\alpha$ . Panel (B) and (C) show two helical electron trajectories with dashed lines assuming a large and small  $\alpha$  (corresponding to a small and large parallel velocity  $v_{||}$ ), respectively.

363 invariant,  $J_3$  is found by integrating Eq. 1.4 over the complete particle orbit around  
 364 the Earth. The shape of this drift orbit is otherwise known as a drift shell. For  $J_3$ ,  
 365 the first term is negligible and the second term is the magnetic flux enclosed by the  
 366 drift shell,  $\Phi_m$  i.e.  $J_3 \sim \Phi_m$ .

367 Figure 1.3 from Schulz and Lanzerotti (1974) shows contours of the gyration,  
 368 bounce, and drift frequencies for electrons and protons in Earth's dipole magnetic  
 369 field.

Up until now we have considered the three periodic motions due Earth's magnetic field and the absence of electric fields. If  $\vec{E}$  is present, a particle's center of gyration i.e., averaged position of the particle over a gyration, will drift with a velocity perpendicular to both  $\vec{E}$  and  $\vec{B}$ . The drift velocity can be solved directly from Eq. 1.1 and is

$$\vec{v}_E = \frac{\vec{E} \times \vec{B}}{B^2}. \quad (1.11)$$

370 Lastly, for more detailed derivations of these motions, see the following texts:  
 371 Baumjohann and Treumann (1997); Schulz and Lanzerotti (1974); Tsurutani and  
 372 Lakhina (1997).

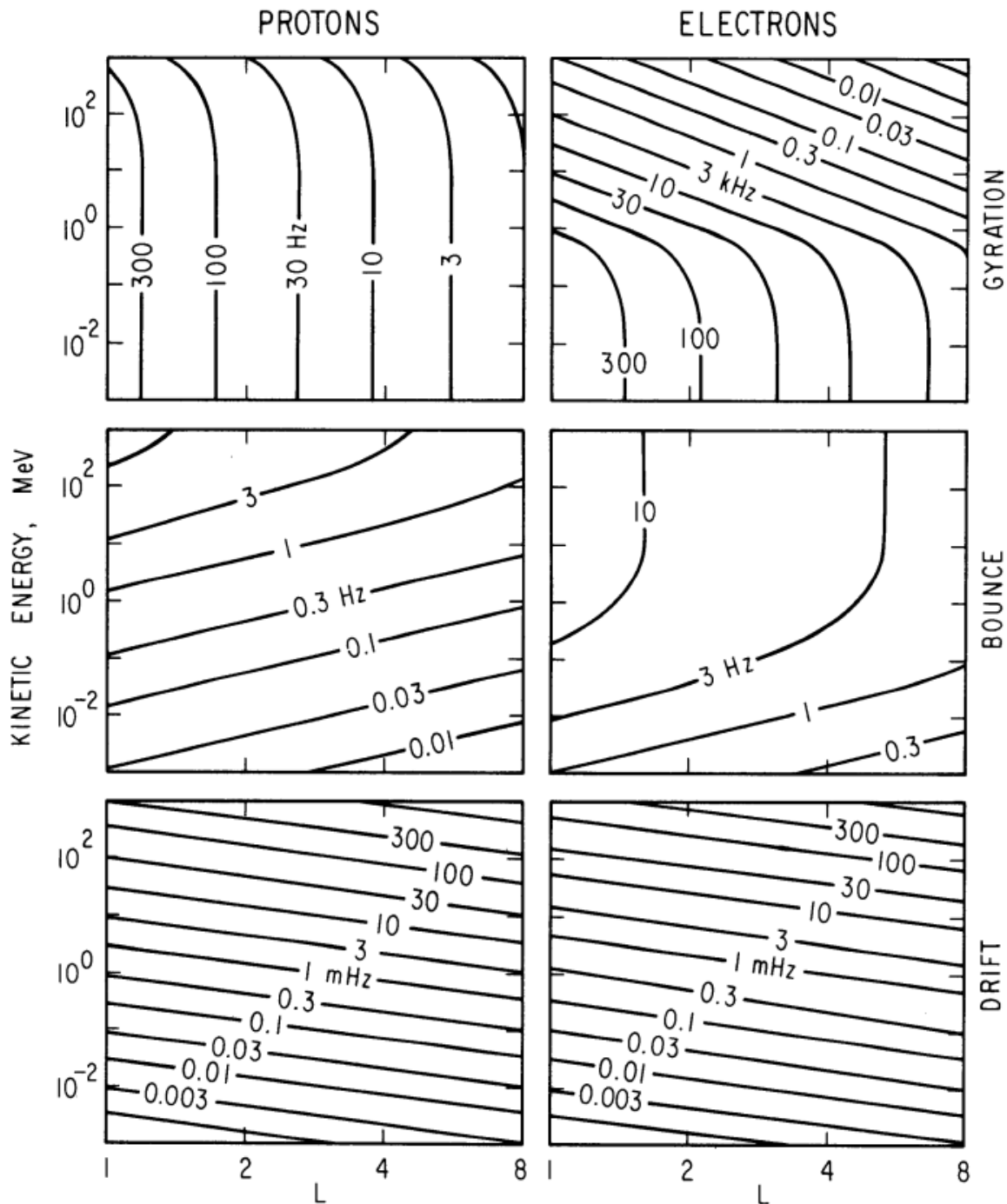


Figure 1.3: Contours of constant gyration, bounce, and drift frequencies for electrons and protons in a dipole field. Figure from Schulz and Lanzerotti (1974).

373

## Particle Populations and Their Interractions in the Magnetosphere

374        The single-particle motion in Earth's magnetic field described in the previous  
375    section is a prerequisite to understanding how magnetospheric particles organize into  
376    macroscopic populations. The structure of the outer magnetosphere is shown in Fig.  
377    1.4 and inner magnetosphere in Fig. 1.5. In this section we will introduce the various  
378    particle populations in the magnetosphere and how they couple.

379        The sun and its solar wind are ultimately the source of energy input into the  
380    magnetosphere. The solar wind at Earth's orbit is a plasma traveling at supersonic  
381    speeds with an embedded interplanetary magnetic field (IMF). When the solar wind  
382    encounters Earth's magnetic field the plasma can not easily penetrate into the  
383    magnetosphere, rather it drapes around the magnetosphere forming a cavity in the  
384    solar wind that is roughly shaped as shown in Fig. 1.4. Because the solar wind is  
385    supersonic at 1 AU, a bow shock exists upstream of the magnetosphere. The solar  
386    wind plasma, after it is shocked by the bow shock, flows around the magnetosphere  
387    inside the magnetosheath. The surface where the solar wind ram pressure and Earth's  
388    magnetic pressure balance is termed the magnetopause, which can be thought of as  
389    a boundary between the solar wind's and Earth's plasma environments. This is  
390    a slightly naive description of the magnetopause, but is nonetheless an instructive  
391    conceptual picture. The shocked plasma then flows past the Earth where it shapes  
392    the magnetotail. In the magnetotail the solar wind magnetic pressure balances Earth's  
393    magnetic field pressure in the lobes. The magnetotail extends on the order of 100  
394     $R_E$  downstream of Earth [Add citation](#), and the tailward stretching of magnetic field  
395    lines creates the plasma sheet which exists in the region of low magnetic field strength  
396    near the magnetic equator [Add citation](#). The plasma sheet flows from dusk to dawn  
397    (out of the page in Figs. 1.4 and 1.5) and this current is connected to a zoo of other

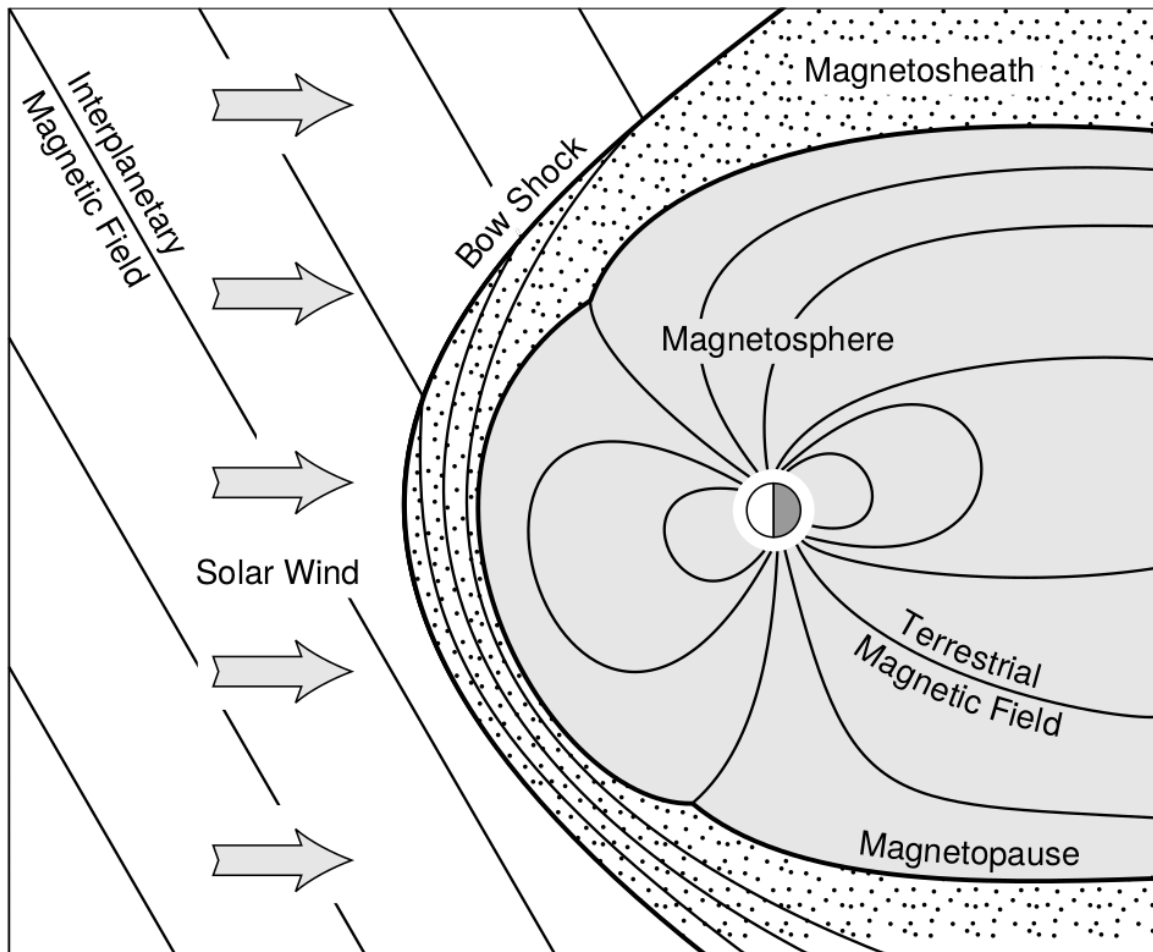


Figure 1.4: Macroscopic structures in the outer magnetosphere. The solar wind with its frozen-in interplanetary magnetic field is shown on the left and is traveling supersonically towards the right. The solar wind envelops Earth's magnetic field to create the magnetosphere cavity. Since the solar wind is traveling supersonically, it creates a bow shock up stream. Downstream of the bow shock the shocked solar wind plasma inside the magnetosheath flows around the magnetopause, a boundary between the solar wind and magnetosphere. Figure from Baumjohann and Treumann (1997).

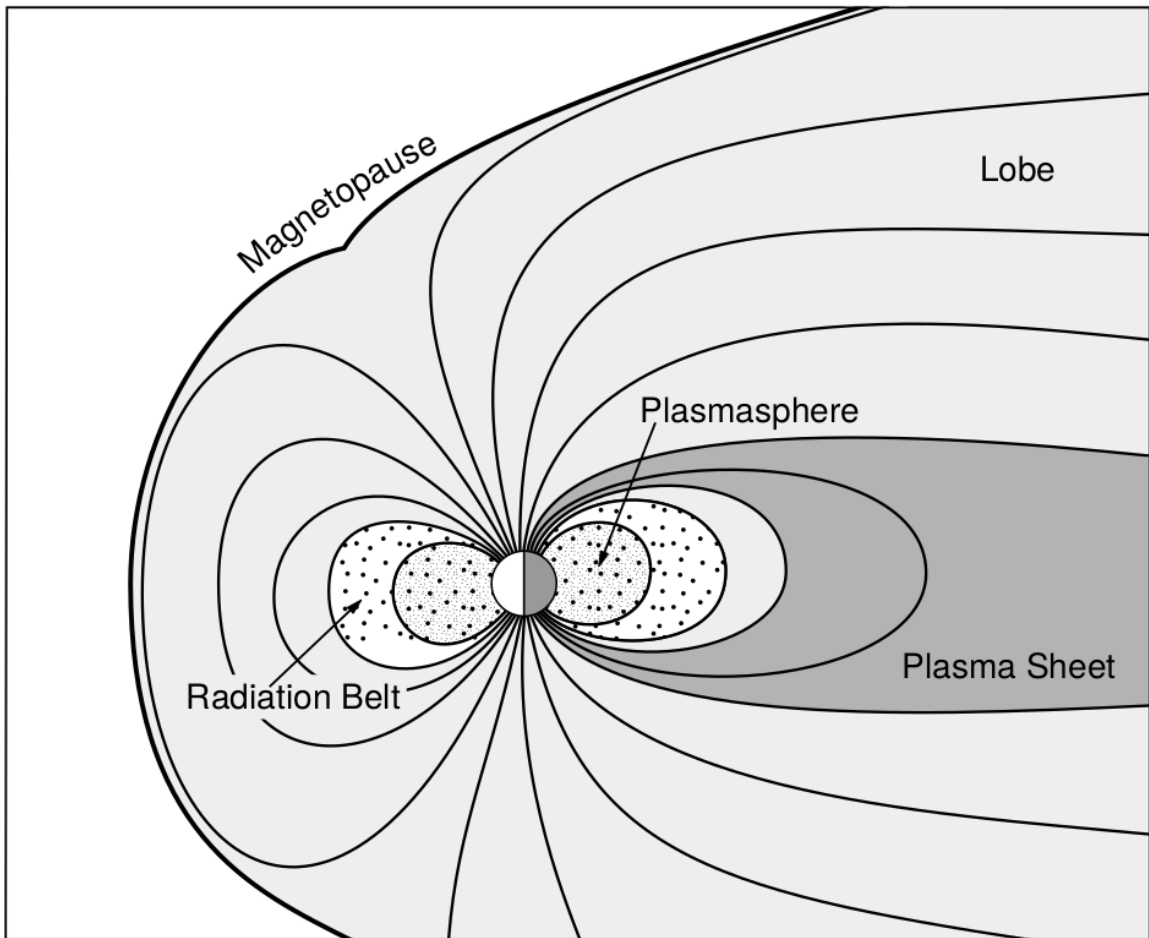


Figure 1.5: Macroscopic structures in the inner magnetosphere most relevant to this dissertation. The plasmasphere, and the radiation belts are shown and ring current is co-located there as well. Sun is to the left. Figure from Baumjohann and Treumann (1997).

398 currents in the magnetosphere which is beyond the scope of this dissertation.

399 The idea of the magnetopause as a barrier between the solar wind and  
 400 the magnetosphere is not entirely accurate due to the presence of reconnection.  
 401 Reconnection was first conceived by Dungey (1961) who described the convection of  
 402 Earth's magnetic field between the bow and tail regions of the magnetosphere. This  
 403 process is known as the Dungey cycle and is most effective when the IMF is pointing  
 404 southward as is shown in Fig. 1.6 part 1. As the IMF contacts Earth's magnetic  
 405 field it reconnects with it so that Earth's magnetic field is directly connected to the  
 406 IMF. Then as the solar wind flows tailward the IMF drags Earth's magnetic field  
 407 towards the magnetotail as shown in Fig. 1.6 parts 2-6. As more and more magnetic  
 408 field lines are draped in the magnetotail, magnetic pressure increases in the lobes  
 409 which squeezes the plasma sheet until Earth's magnetic field reconnects as is shown  
 410 in Fig. 1.6 part 7. Lastly, Fig. 1.6 part 8 shows the newly merged magnetic field  
 411 line and the plasma frozen on it moves Earthward under the magnetic tension force  
 412 to become more dipolar. This is called a dipolarization of the magnetic field, and the  
 413 plasma frozen on these field lines can be observed as injections (e.g. Turner et al.,  
 414 2015). Injection of plasma into the inner magnetosphere is one of the drivers of inner  
 415 magnetosphere dynamics. Should I talk about the K-H instability and how there  
 416 could be micro reconnection? i.e. cite a paper or two that support or refute that  
 417 idea.

418 Inner Magnetosphere Populations

419 Before we describe the inner magnetosphere particle populations, we first need to  
 420 describe the coordinate system used to organize the inner magnetosphere populations.  
 421 The first coordinate was defined in section 1 and is the L shell. L shell can be thought  
 422 of as an analogue to a radius but in a dipole geometry. The azimuthal coordinate

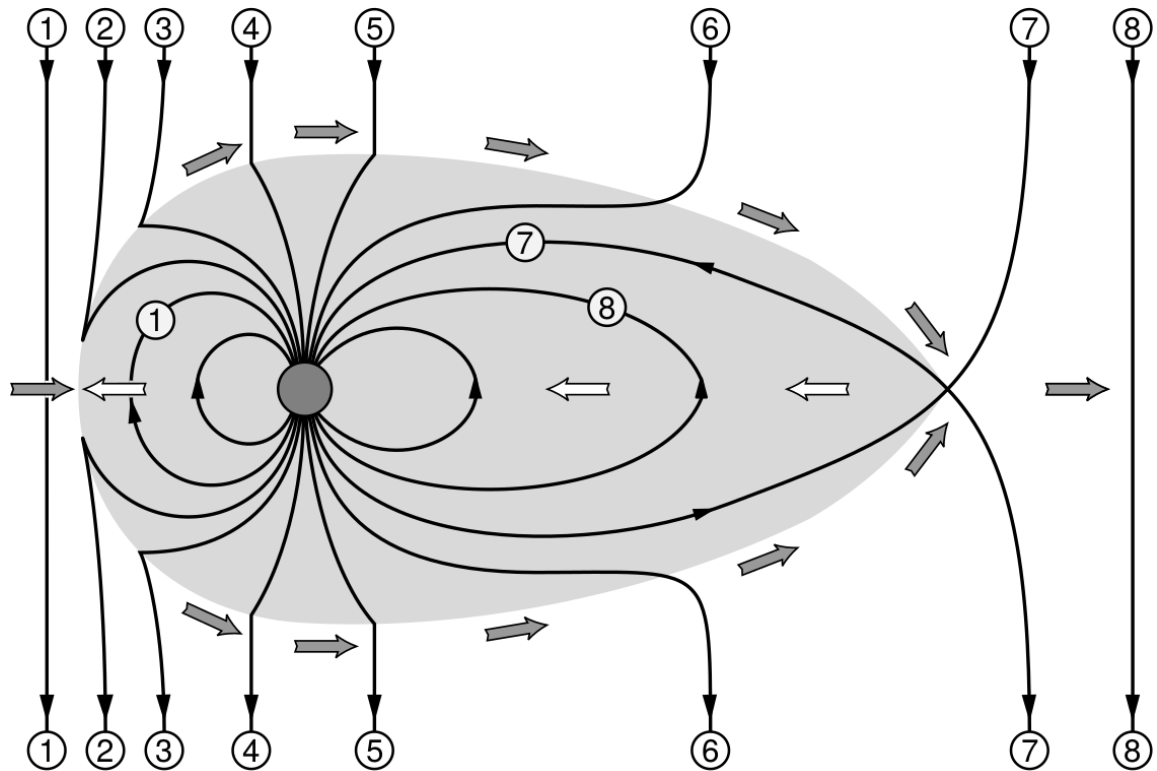


Figure 1.6: The series of steps involved in magnetic reconnection with a southward IMF. Figure from Baumjohann and Treumann (1997).

423 is the magnetic local time (MLT). For an observer above Earth's north pole looking  
 424 down, MLT is defined to be 0 (midnight) in the anti-sunward direction, and increases  
 425 in the counter-clockwise direction with 6 at dawn, 12 at noon (sunward direction),  
 426 and 18 in dusk. The last coordinate used in this dissertation is the magnetic latitude,  
 427  $\lambda$  which is analogous to the latitude coordinate and is defined to be 0 at the magnetic  
 428 equator.

429 The low energy particle dynamics in the inner magnetosphere are organized by  
 430 two electric fields: the co-rotation and the dawn-dusk electric fields. The co-rotation  
 431 electric field arises from the rotation of Earth's magnetic field. Since particles are  
 432 frozen on magnetic field lines and the plasma conductivity is effectively infinite, to  
 433 a non-rotating observer, Earth's rotation appears as a radial electric field that drops  
 434 off as  $\sim L^2$ . This electric field makes particles orbit around the Earth due to the  
 435  $\vec{E} \times \vec{B}$  drift. The other electric field, pointing from dawn to dusk is called the  
 436 convection electric field and is formed by the Earthward transport of particles from  
 437 the magnetotail that appears as an electric field to a stationary observer (with respect  
 438 to Earth). The superposition of the co-rotation and convection electric fields  
 439 results in a potential field shown in Fig. 1.7. The shaded area in Fig. 1.7 shows  
 440 the orbits on which low energy electrons are trapped, and outside are the untrapped  
 441 particles. The dynamic topology of the shaded region in Fig. 1.7 is controlled by only  
 442 the convection electric field which is dependent on the solar wind speed and the IMF.  
 443 The lowest energy particles, that are most effected by these electric fields, make up  
 444 the plasmasphere.

445 Plasmasphere The plasmasphere is a dense ( $n_e \sim 10^3/\text{cm}^3$ ), cool plasma  
 446 ( $\sim \text{eV}$ ) that extends to  $L \sim 4$  (extent is highly dependent on the solar wind and  
 447 magnetospheric conditions) and is sourced from the ionosphere. The two main

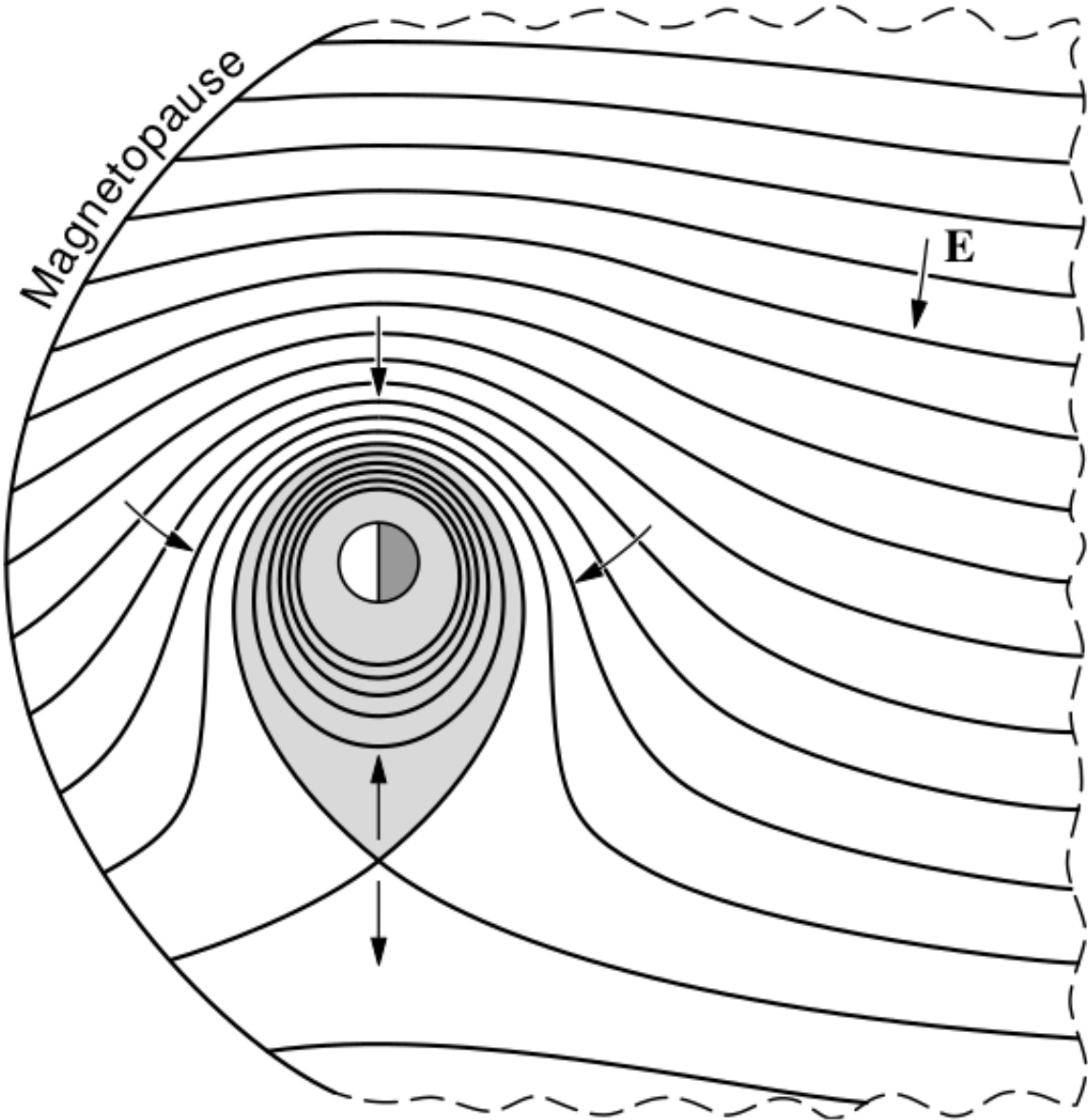


Figure 1.7: Equipotential lines and electric field arrows due to the superposition of the co-rotation and convection electric fields. Electrons in the shaded region execute closed orbits. Outside of the shaded regions the electrons are not trapped and will escape. The region separating the two regimes is called the Alfvén layer. Figure from Baumjohann and Treumann (1997).

448 mechanisms that source the cold plasma from the ionosphere are ultraviolet ionization  
 449 by sunlight and particle precipitation. The ultraviolet ionization by sunlight is  
 450 strongly dependent on the time of day (day vs night), latitude (more ionization near  
 451 the equator). The ionization due to particle precipitation, on the other hand, is highly  
 452 dependent on magnetospheric conditions, and mostly occurs at high latitudes.

453 The outer boundary of the plasmasphere is the plasmapause which is typically  
 454 identified as a steep radial gradient in plasma density from  $\sim 10^3/\text{cm}^3$  to  $\sim 1/\text{cm}^3$ . As  
 455 we will see throughout this dissertation, the location of the plasmapause is important  
 456 to model (e.g. O'Brien and Moldwin, 2003) and understand since the plasma density  
 457 strongly controls the efficiency of particle scattering (Horne et al., 2005).

458 Ring Current The next higher energy population is the ring current. This  
 459 population consists of protons and electrons between tens and a few hundred keV  
 460 that drift around the Earth. The orbits of higher energy particles are not as effected  
 461 by the convection and co-rotation electric field, rather they drift around the Earth  
 462 due to gradient and curvature drifts. Since the direction of the drift is dependent on  
 463 charge, protons drift west around the Earth and electrons drift East. This has the  
 464 effect of creating a current around the Earth.

465 The ring current generates a magnetic field which decreases the magnetic field  
 466 strength on Earth's surface and increases it outside of the ring current. The decrease  
 467 of Earth's magnetic field strength is readily observed by a system of ground-based  
 468 magnetometers and is merged into a Disturbance Storm Time (DST) index. An  
 469 example of a DST index time series from a coronal mass ejection (CME) driven 2015  
 470 St. Patrick's Day storm is shown in Fig. 1.8. The ring current is sometimes first  
 471 depleted and DST increases slightly (initial phase or sudden storm commencement).  
 472 Then the ring current is rapidly built up during which DST rapidly decreases (main

473 phase). Lastly the ring current gradually decays toward its equilibrium state over a  
 474 period of a few days and DST increases towards 0 (recovery phase). The DST index  
 475 along with other indicies are readily used by the space physics community to quantify  
 476 the global state of the magnetosphere.

477        Radiation Belts The highest energy particle populations are in the Van Allen  
 478 radiation belts. These belts were discovered by Van Allen (1959) and Vernov and  
 479 Chudakov (1960) during the Cold War and are a pair of toroidally shaped populations  
 480 of trapped electrons and protons usually within to  $L < 8$  and are shown in Fig. 1.9.  
 481 Their quiescent toroidal shape is similar to the shape of the plasmasphere and ring  
 482 current and is a result of Earth's dipole magnetic field and the conservation of the  
 483 three adiabatic invariants discussed in section 1.

484        The inner radiation belt is extremely stable on time periods of years, extends  
 485 to  $L \approx 2$ , and mainly consists of protons with energies between MeV and GeV and  
 486 electrons with energies up to  $\approx 1$  MeV (Claudepierre et al., 2019). The source of  
 487 inner radiation belt protons is believed to be due to cosmic-ray albedo neutron decay  
 488 (e.g. Li et al., 2017) and inward radial diffusion for electrons (e.g. O'Brien et al.,  
 489 2016). The gap between the inner and outer radiation belt is called the slot, which is  
 490 believed to be due to hiss waves inside the plasmasphere (described below) scattering  
 491 particles into the atmosphere (e.g. Breneman et al., 2015; Lyons and Thorne, 1973).

492        The outer radiation belt, on the other hand is much more dynamic and consists  
 493 of mainly electrons of energies up to a few MeV. The outer belt's spatial extent is  
 494 highly variable e.g. see Fig. 1.10, and is typically observed at  $4 < L < 8$ . Since  
 495 the outer radiation belt contains a dynamic population of energetic particles that  
 496 pose a threat to human and technological presence in Earth's atmosphere and space,  
 497 decades of research has been undertaken to understand and predict the outer radiation

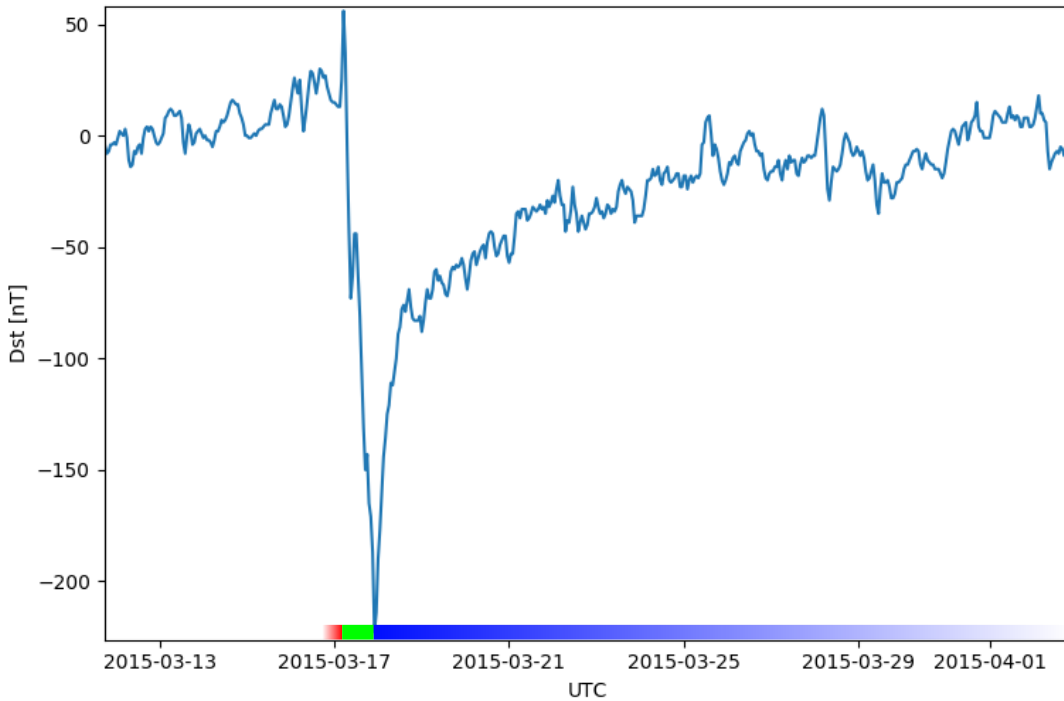


Figure 1.8: The DST index during the St. Patrick's Day 2015 storm. This storm was caused by a coronal mass ejection on March 15th, 2015. The storm phases are: initial phase, main phase, and recovery phase. The initial phase occurred when the Dst peaked at +50 nT on March 17th during which the ring current was eroded by the coronal mass ejection during the interval shown by the red bar. Then the rapid decrease to  $\approx -200$  nT was during the main phase where many injections from the magnetotail pumped up the ring current which reduced Earth's magnetic field strength at the ground and is shown with the green bar. Lastly, the recovery phase lasted from March 18th to approximately March 29th during which the ring current particles were lost and the ring current returned to its equilibrium state. The recovery phase is shown with the blue bar.

## The Earth's Electron Radiation Belts

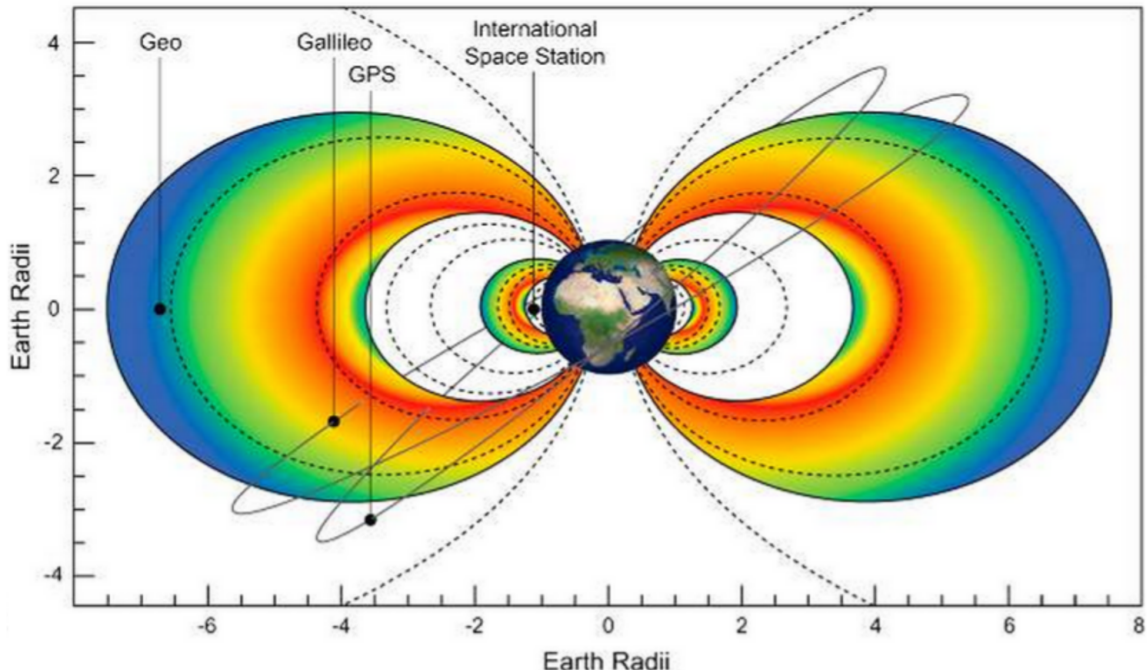


Figure 1.9: The two radiation belts with the locations of various satellites.  
Figure from (Horne et al., 2013).

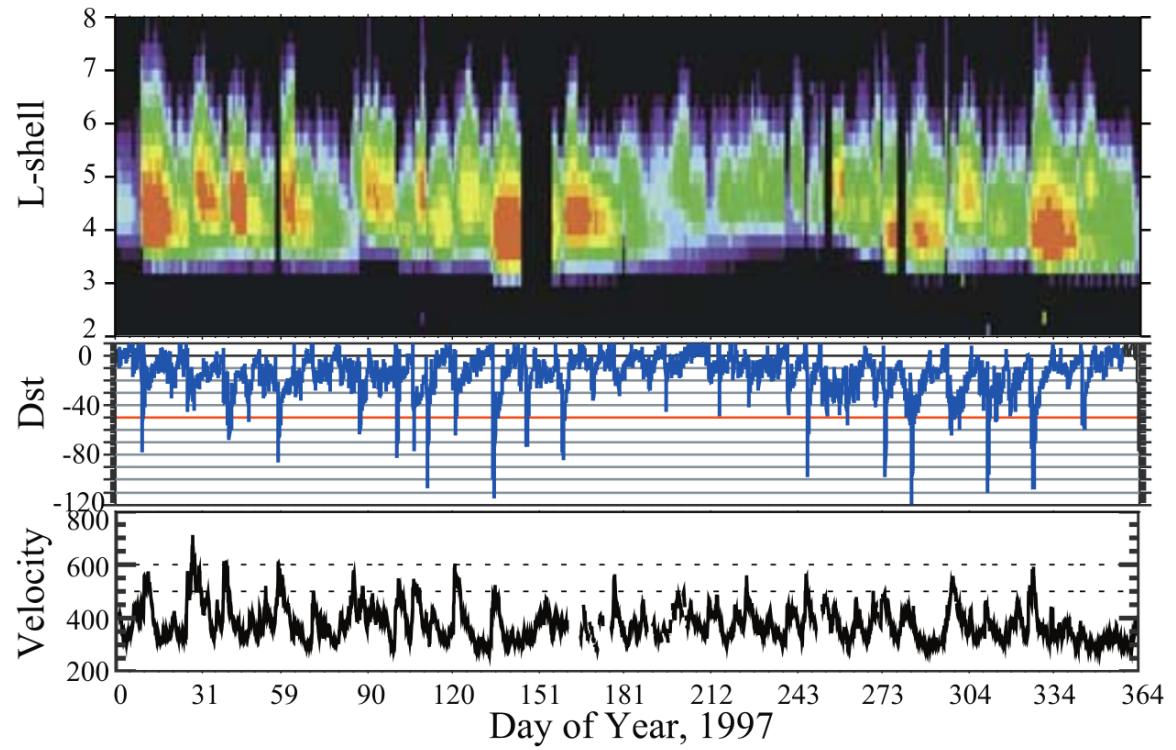


Figure 1.10: The dynamics of the outer radiation belt in 1997 from the POLAR satellite. Top panel shows the 1.2-2.4 MeV electron flux as a function of L and 1997 day of year. The middle panel shows the DST index, and bottom panel shows the solar wind velocity. Figure from (Reeves et al., 2003).

498 belt particles, waves, and wave-particle interactions. The dynamics of the outer  
 499 radiation belt can be understood by considering various competing acceleration and  
 500 loss mechanisms which will be described in the following sections.

501 Radiation Belt Particle Sources and Sinks

502 Adiabatic Heating

503 One of the particle heating and transport mechanisms arises from the Earthward  
 504 convection of particles. The conservation of  $J_1$  implies that the initial and final  $v_{\perp}$   
 505 depends on the change in the magnetic field amplitude

$$\frac{v_{\perp i}^2}{B_i} = \frac{v_{\perp f}^2}{B_f}. \quad (1.12)$$

506 As a particle convects Earthward,  $B_f > B_i$  thus  $v_{\perp}$  must increase. The dipole  
 507 magnetic field amplitude can be written as

$$B(L, \theta) = \frac{31.2 \mu\text{T}}{L^3} \sqrt{1 + 3 \cos^2 \theta} \quad (1.13)$$

508 which implies that

$$\frac{v_{\perp f}^2}{v_{\perp i}^2} = \left( \frac{L_i}{L_f} \right)^3. \quad (1.14)$$

509 .

510 In addition, as the particle convects Earthward the distance between the  
 511 particle's mirror points decrease. If  $J_2$  is conserved, the shrinking bounce path implies  
 512 that  $v_{||}$  must increase by

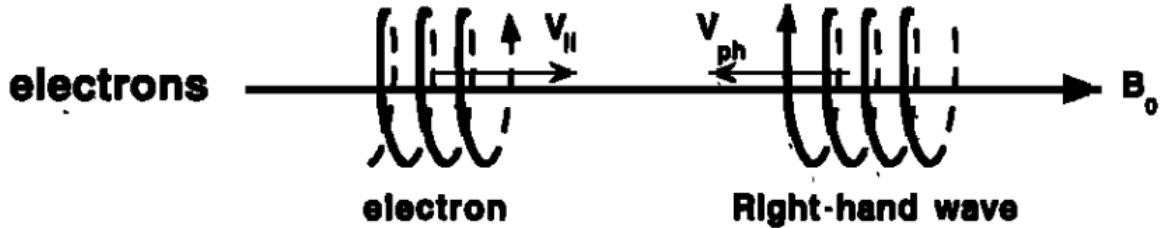
$$\frac{v_{|| f}^2}{v_{|| i}^2} = \left( \frac{L_i}{L_f} \right)^k \quad (1.15)$$

513 where  $k$  ranges from 2 for equatorial pitch angles,  $\alpha_{eq} = 0^\circ$ , to 2.5 for  $\alpha_{eq} = 90^\circ$   
 514 (Baumjohann and Treumann, 1997). Since the rate of adiabatic heating is greater in  
 515 the perpendicular direction than heating in the parallel direction, an initially isotropic  
 516 particle distribution will become anisotropic during its convection. These isotropic  
 517 particles can then become unstable to wave growth and generate waves in order to  
 518 reach equilibrium.

519 Wave Resonance Heating

520 Another mechanism that heats particles is due to particles resonating with  
 521 plasma waves. A few of the electromagnetic wave modes responsible for particle  
 522 acceleration (and deceleration) relevant to radiation belt dynamics are hiss, whistler  
 523 mode chorus (chorus), and electromagnetic ion cyclotron (EMIC) waves. These waves  
 524 are created by the loss cone instability that driven by an anisotropy of electrons  
 525 for chorus waves, and protons for EMIC waves. The level of anisotropy can be  
 526 quantified by the ratio of the perpendicular to parallel particle temperatures ( $T_\perp/T_{||}$ ).  
 527 A particle distribution is unstable when  $T_\perp/T_{||} > 1$  which facilitates wave growth.  
 528 Since electrons gyrate in a right-handed sense, the chorus waves also tend to be right  
 529 hand circularly polarized (Tsurutani and Lakhina, 1997). The same argument applies  
 530 to protons and left hand circularly polarized EMIC waves as well.

531 These circularly polarized waves can resonate with electrons and/or protons  
 532 when their combined motion results in a static  $\vec{E}$ . One example of a resonance  
 533 between a right hand circularly polarized wave and an electron is shown in Fig. 1.21  
 534 and is termed the cyclotron resonance. An electron's  $v_{||}$  and the wave's parallel wave  
 535 vector,  $k_{||}$  are in opposite directions such that the wave frequency  $\omega$  is Doppler shifted  
 536 to an integer multiple of the  $\Omega_e$  at which point the electron feels a static electric  
 537 field and is accelerated or decelerated. This acceleration happens when a resonance



$$\omega + k_{\parallel} V_{\parallel} = \Omega^-$$

Figure 1.11: The trajectories of an electron and a right-hand circularly polarized wave during a cyclotron resonance. The electron's  $v_{\parallel}$  and the wave's  $k_{\parallel}$  are in opposite directions such that the wave's frequency is Doppler shifted to an integer multiple of the electron cyclotron frequency. Figure from (Tsurutani and Lakhina, 1997).

538 condition is satisfied between a wave and a particle for which we will now derive an  
539 illustrative toy model.

540 Assume a uniform magnetic field  $\vec{B} = B_0 \hat{z}$  with a parallel propagating ( $k = k \hat{z}$ ),  
541 right-hand circularly polarized wave. The wave's electric field as a function of position  
542 and time can be written as

$$\vec{E} = E_0 (\cos(\omega t - kz) \hat{x} + \sin(\omega t - kz) \hat{y}) \quad (1.16)$$

which is more clearly expressed by taking the dot product to find  $\vec{E}$  in the  $\hat{\theta}$  direction

$$E_{\theta} = \vec{E} \times \hat{\theta} = E_0 \cos(\omega t - kz + \theta). \quad (1.17)$$

543 Now assume that the electron is traveling in the  $-\hat{z}$  direction with a velocity  $\vec{v} = -v_0 \hat{z}$   
544 so its time dependent position along  $\hat{z}$  is

$$z(t) = -v_0 t \quad (1.18)$$

545 and gyrophase is

$$\theta(t) = -\Omega t + \theta(0) \quad (1.19)$$

546 where the first negative sign comes from the electron's negative charge. Now we put  
547 this all together and express the electric field and the force that the electron will  
548 experience

$$m \frac{dv_\theta}{dt} = qE_\theta = qE_0 \sin((\omega + kv_0 - \Omega)t + \theta(0)). \quad (1.20)$$

549 This is a relatively complex expression, but when the time dependent component,

$$\omega + kv_0 - \Omega = 0, \quad (1.21)$$

550 the electron will be in a static electric field which will accelerate or decelerate the  
551 electron depending on  $\theta_0$ , the phase between the wave and the electron. **Show Bortnik**  
552 **2008 plot?** The expression in Eq. 1.21 is commonly referred to as the resonance  
553 condition and is more generally written as

$$\omega - k_{||}v_{||} = \frac{n\Omega_e}{\gamma} \quad (1.22)$$

554 where  $n$  is the resonance order, and  $\gamma$  is the relativistic correction (e.g. Millan and  
555 Thorne, 2007). In the case of the cyclotron resonance,  $\omega \approx \Omega_e$  thus  $J_1$  is violated.  
556 Since  $J_1$  is violated,  $J_2$  and  $J_3$  are also violated since the conditions required to  
557 violate  $J_2$  and  $J_3$  are less stringent than  $J_1$ . It is important to remember that along  
558 the particle's orbit it will encounter and experience the effects of many waves along  
559 its orbit. The typical MLT extent of a handful of waves that are capable of resonating  
560 with radiation belt electrons are shown in Fig. 1.12.

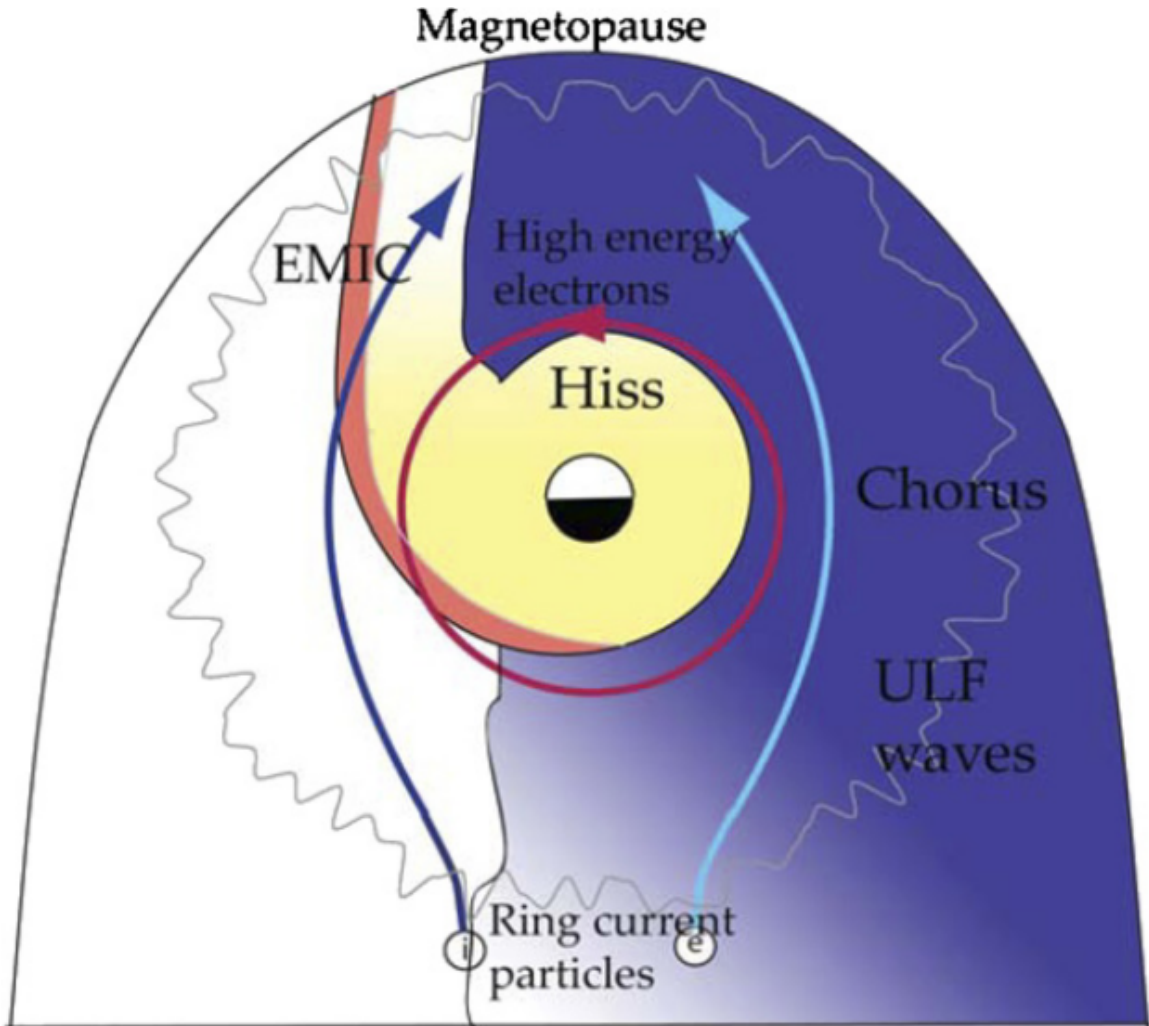


Figure 1.12: Various wave modes in the magnetosphere. Ultra low frequency waves occur through the magnetosphere. Chorus waves are typically observed in the 0-12 midnight-dawn region. EMIC waves are typically observed in the dusk MLT sector. Hiss waves are observed inside the plasmasphere. Figure from Millan and Thorne (2007).

561 Particle Losses

562 Now that we have seen two general mechanisms with which particles are  
 563 accelerated and transported in the magnetosphere, we will now consider a few  
 564 specific mechanisms with which particles are lost to the atmosphere or the solar  
 565 wind. One particle loss mechanism into the solar wind is magnetopause shadowing  
 566 (e.g. Ukhorskiy et al., 2006). Particles are sometimes lost when the ring current is  
 567 strengthened and Earth's magnetic field strength is increased outside of the ring  
 568 current (and reduced on Earth's surface). If the time scale of the ring current  
 569 strengthening is slower than a particle drift,  $J_3$  is conserved. Then in order to  
 570 conserve  $J_3$  while the magnetic field strength is increased, the particle's drift shell  
 571 must move outward to conserve the magnetic flux contained by the drift shell. Then  
 572 if the particle's drift shell expands to the point that it crosses the magnetopause, the  
 573 particle will be lost to the solar wind.

574 **Move to acceleration?** Another particle loss and acceleration mechanism is driven  
 575 by ultra low frequency (ULF) waves and is called radial diffusion. Radial diffusion is  
 576 the transport of particles from high to low phase space density,  $f$ . If the transport is  
 577 radially inward, particles will appear to be accelerated. On the other hand, radially  
 578 outward radial diffusion can transport particles through the magnetopause where  
 579 they will be lost to the solar wind. Reeves et al. (2013) investigated the driver of  
 580 particle acceleration during the October 2012 storm and observationally found that  
 581 inward radial diffusion was not dominant, rather local acceleration via wave-resonance  
 582 heating (i.e. particle diffusion in pitch angle and energy which will be described below)  
 583 appeared to be the dominant acceleration mechanism.

584 The loss mechanism central to this dissertation is pitch angle and energy  
 585 scattering of electrons by waves. Some of the waves that scatter electrons in energy  
 586 and pitch angle in the inner magnetosphere are: plasmaspheric hiss (e.g. Breneman

587 et al., 2015; O'Brien et al., 2014), EMIC waves (e.g. Capannolo et al., 2019; Hendry  
 588 et al., 2017), and chorus waves (e.g. Breneman et al., 2017; Kasahara et al., 2018;  
 589 Ozaki et al., 2019). These wave-particle interactions occur when the resonance  
 590 condition in Eq. 1.22 is satisfied at which point the particle's energy and  $\alpha$  is modified  
 591 by the wave. More details regarding the theory of pitch angle and energy diffusion is  
 592 given in Chapter X. If the wave changes  $\alpha$  towards 0 such that  $\alpha < \alpha_{LC}$ , the particle's  
 593 mirror point lowers to less than 100 km altitude where the particle can be lost due  
 594 collisions with air. One manifestation of pitch angle scattering of particles into the  
 595 loss cone are microbursts: a sub-second durtaison impulse of electrons.

596

### Microbursts

597 Microbursts were first identified in high altitude balloon observations of bremsstrahlung  
 598 X-rays emitted by microburst electrons impacting the atmosphere by Anderson and  
 599 Milton (1964). Since then, other balloons have observed microburst X-ray signatures  
 600 in the upper atmosphere (e.g. Anderson et al., 2017; Barcus et al., 1966; Brown et al.,  
 601 1965; Parks, 1967; Trefall et al., 1966; Woodger et al., 2015). In addition to their X-ray  
 602 signature, microbursts electrons have been directly observed in LEO with spacecraft  
 603 including the Solar Anomalous and Magnetospheric Particle Explorer (SAMPEX),  
 604 Focused Investigation of Relativistic Electron Bursts: Intensity, Range, and Dynamics  
 605 II (FIREBIRD-II), Science Technologies Satellite (STSAT-I) (e.g. Blake et al., 1996;  
 606 Blum et al., 2015; Breneman et al., 2017; Crew et al., 2016; Lee et al., 2012, 2005;  
 607 Lorentzen et al., 2001a,b; Nakamura et al., 1995, 2000; O'Brien et al., 2004, 2003).  
 608 An example microburst time series is shown in Fig. 1.13 and was observed by  
 609 Montana State University's (MSU) FIREBIRD-II CubeSats. The prominent features  
 610 of microbursts in Fig. 1.13 are their  $\pm 1$  second duration, half order of magnitude  
 611 increase in count rate above the falling background, and their approximately 200-800

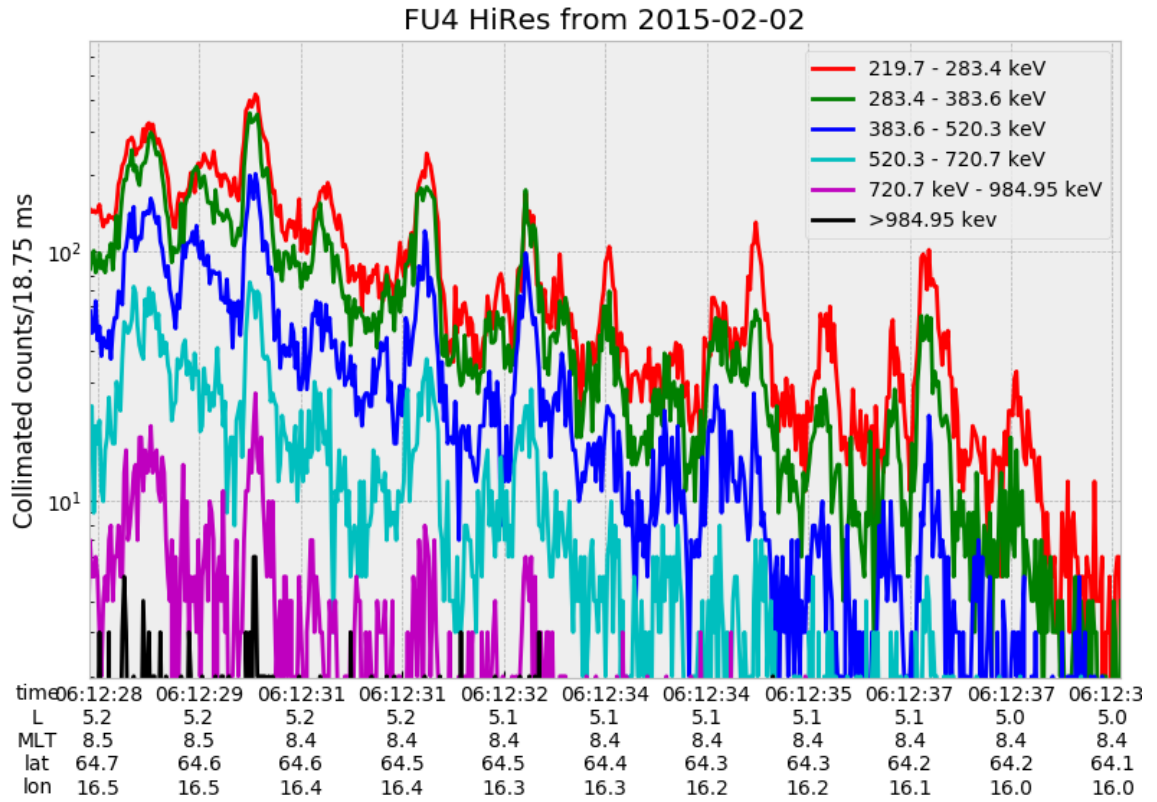


Figure 1.13: An example train of microbursts observed by FIREBIRD-II unit 4 on February 2nd, 2015. The colored curves show the differential energy channel count rates in six channels from  $\approx 200$  keV to greater than 1 MeV. The x-axis labels show auxiliary information such as time of observation and the spacecraft position in L, MLT, latitude and longitude coordinates.

612 keV energy extent.

613 Microbursts are observed on magnetic field footprints that are connected to the  
 614 outer radiation belt (approximately  $4 < L < 8$ ), and are predominately observed in  
 615 the 0-12 MLT sector with an elevated occurrence frequency during magnetospherically  
 616 disturbed times as shown in Fig. 1.14. Microbursts have been previously observed  
 617 over a wide energy range from a few tens of keV (Datta et al., 1997; Parks, 1967) to  
 618 greater than 1 MeV (e.g. Blake et al., 1996; Greeley et al., 2019). The microburst

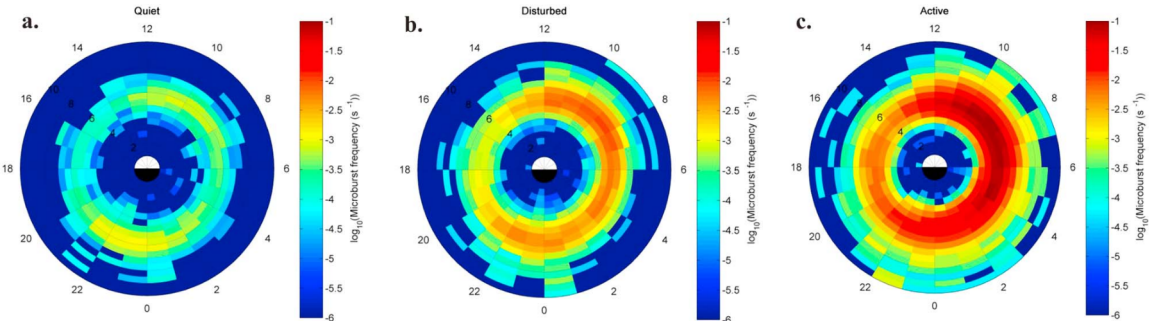


Figure 1.14: Relativistic ( $> 1\text{MeV}$ ) distribution of microburst occurrence rates as a function of  $L$  and MLT. The three panels show the microburst occurrence rate dependence on geomagnetic activity, parameterized by the auroral electrojet (AE) index for (a)  $\text{AE} < 100 \text{ nT}$ , (b)  $100 < \text{AE} < 300 \text{ nT}$  and (c)  $\text{AE} > 300 \text{ nT}$ . Figure from Douma et al. (2017).

619 electron flux ( $J$ ) falls off in energy, and the microburst energy spectra is typically  
 620 well fit to a decaying exponential

$$J(E) = J_0 e^{-E/E_0} \quad (1.23)$$

621 where  $J_0$  is the flux at 0 keV (unphysical free parameter) and  $E_0$  quantifies the  
 622 efficiency of the scattering mechanism in energy (.e.g Datta et al., 1997; Lee et al.,  
 623 2005; Parks, 1967). A small  $E_0$  suggests that mostly low energy particles are scattered  
 624 and a high  $E_0$  suggests that the scattering mechanism scatters low and high energy  
 625 electrons. Reality is a bit more messy and a high  $E_0$  may be a signature of a scattering  
 626 mechanism preferential to high energy electrons, but is hidden by the convolution of  
 627 the source particles available to be scattered (typically with a falling energy spectrum)  
 628 and the energy-dependent scattering efficiency.

629 The short duration of microbursts observed by a single LEO satellite has an  
 630 ambiguity when interpreting what is exactly a microburst. The two possible realities  
 631 are: a microburst is very small and spatially stationary so that the LEO spacecraft

632 passes through it in less than a second. Alternatively, microbursts are spatially large  
 633 with a short duration such that the microburst passes by the spacecraft in a fraction  
 634 of a second. There are a few ways to distinguish between the two possible realities,  
 635 and each one has a unique set of advantages.

636 A high altitude balloon provides essentially a stationary view of the precipitating  
 637 particles under the radiation belt footprints so a short-lived, temporal microburst  
 638 can be unambiguously identified. Spatial structures on the other hand are difficult  
 639 to identify because a balloon is essentially still on drift timescales thus a variation in  
 640 the X-rays can be due to the spatial structure or an increase of precipitating particles  
 641 over the whole area. Furthermore, if the stationary structure is drifting its particles  
 642 are not precipitating into the atmosphere so there is no X-ray signature.

643 Another solution is multi-spacecraft missions that can determine if a microburst  
 644 is spatial or temporal. As will be shown in this dissertation, if a microburst is  
 645 observed simultaneously by two spacecraft then it is temporally transient and has  
 646 a size greater than the spacecraft separation. On the other hand, if two spacecraft  
 647 observe a microburst-like feature in the same location and at different times, then it is  
 648 spatial may be a curtain (Blake and O'Brien, 2016). Both observational methods have  
 649 a unique set of strengths, and this dissertation takes the multi-spacecraft approach  
 650 to identify and study microbursts.

651

### Scope of Research

652 This dissertation furthers our understanding of the microburst scattering  
 653 mechanism by observing the scattering directly, and measuring the microburst sizes  
 654 and comparing them to the size of waves near the magnetic equator where those  
 655 electrons could have been scattered. Chapter X describes a microburst scattering  
 656 event observed by NASA's Van Allen Probes which was studied in the theoretic

657 framework of pitch angle and energy diffusion. The following two chapters will then  
658 study the size of microbursts. Chapter Y describes a bouncing packet microburst  
659 observation made by MSU's FIREBIRD-II mission where the microburst's lower  
660 bound longitudinal and latitudinal sizes were estimated. Then Chapter Z expands  
661 the case study from Ch. Y to a statistical study of microburst sizes using The  
662 Aerospace Corporation's AeroCube-6 (AC6) CubeSats. In this study, a Monte Carlo  
663 and analytic microburst size models were developed to account for the compounding  
664 effects of random microburst sizes and locations. Lastly, Ch. A will summarize the  
665 dissertation work and make concluding remarks regarding outstanding questions in  
666 microburst physics.

667

## CHAPTER TWO

668

EVIDENCE OF MICROBURSTS OBSERVED NEAR THE EQUATORIAL

669

PLANE IN THE OUTER VAN ALLEN RADIATION BELT

670

Contribution of Authors and Co-Authors

671 Manuscript(s) in Chapter(s) 1

672

673 Author: [type author name here]

674 Contributions: [list contributions here, single-spaced]

675 Co-Author: [type co-author name here]

676 Contributions: [list contributions here, single-spaced]

677 Co-Author: [type co-author name here]

678 Contributions: [list contributions here, single-spaced]

679

680

Manuscript Information

681 [Type Author and Co-author(s) Names Here]

682 Geophysical Research Letters

683 Status of Manuscript: Published in a peer-reviewed journal

684 Wiley

685 Volume 45, Issue 16

686

Key Points

- 687     ● First report of direct observation of microbursts at high altitude, near the  
 688       equatorial plane.
- 689     ● Microbursts' duration, flux enhancement, and energy spectra are similar to prior  
 690       observations in LEO.
- 691     ● Microburst generation is not consistent with a single quasi-linear gyroresonant  
 692       interaction with chorus waves.

693

Abstract

694     We present the first evidence of electron microbursts observed near the equatorial  
 695       plane in Earth's outer radiation belt. We observed the microbursts on March 31st,  
 696       2017 with the Magnetic Electron Ion Spectrometer and RBSP Ion Composition  
 697       Experiment on the Van Allen Probes. Microburst electrons with kinetic energies  
 698       of 29-92 keV were scattered over a substantial range of pitch angles, and over time  
 699       intervals of 150-500 ms. Furthermore, the microbursts arrived without dispersion in  
 700       energy, indicating that they were recently scattered near the spacecraft. We have  
 701       applied the relativistic theory of wave-particle resonant diffusion to the calculated  
 702       phase space density, revealing that the observed transport of microburst electrons is  
 703       not consistent with the hypothesized quasi-linear approximation.

704

Introduction

705     Since the Van Allen radiation belts were discovered by Van Allen (1959) and  
 706       Vernov and Chudakov (1960), decades of work has focused on understanding their  
 707       origins and effects on the near-Earth space environment and ionosphere-thermosphere

708 system. The energy content of the outer belt is dominated by energetic electrons,  
 709 with dynamics controlled by a complex interplay between various source and loss  
 710 mechanisms. One important loss and acceleration mechanism is gyroresonant  
 711 diffusion in energy and pitch angle (PA) due to scattering of electrons by plasma  
 712 waves (e.g. Bortnik et al., 2008; Horne and Thorne, 2003; Meredith et al., 2002;  
 713 Millan and Thorne, 2007; Summers et al., 1998; Thorne and Andreoli, 1981; Thorne  
 714 et al., 2005; Walker, 1993).

715 Chorus waves are commonly associated with PA and energy diffusion. These  
 716 waves are typically generated by substorm injections into the inner magnetosphere,  
 717 which lead to a temperature anisotropy of the source electrons with energies up to  
 718 tens of keV (e.g. Horne et al., 2003; Li et al., 2009a). Since these source electrons  
 719 drift eastward, chorus is most frequently observed in the dawn sector, but it has  
 720 been observed at all magnetic local times (MLT) (Li et al., 2009b). Chorus waves  
 721 are believed to generate electron microburst precipitation through wave-particle  
 722 interactions.

723 Microbursts are typically defined as an increase of electron flux in or near the  
 724 atmospheric loss cone that last < 1 s (e.g. Anderson and Milton, 1964; Blake et al.,  
 725 1996; Lorentzen et al., 2001a). Empirical and theoretical analyses indicate that  
 726 microbursts are an important loss process since they can substantially deplete the  
 727 radiation belt electrons on the order of one day (e.g. Breneman et al., 2017; Lorentzen  
 728 et al., 2001b; O'Brien et al., 2004; Thorne et al., 2005). Previously, microbursts have  
 729 been observed in the upper atmosphere in the form of bremsstrahlung X-rays (e.g.  
 730 Anderson et al., 2017; Parks, 1967; Woodger et al., 2015) and directly in low Earth  
 731 orbit (LEO) (e.g. Blake et al., 1996; Blum et al., 2015; Breneman et al., 2017; Crew  
 732 et al., 2016; Lee et al., 2012, 2005; Lorentzen et al., 2001a,b; Mozer et al., 2018;  
 733 Nakamura et al., 1995, 2000; O'Brien et al., 2004, 2003).

734 We observed for the first time, microburst-like signatures near their hypothesized  
 735 origin within the heart of the outer radiation belt. The unique microburst  
 736 observations we report here were possible with the Van Allen Probe-A's (RBSP-  
 737 A) Magnetic Electron Ion Spectrometer's (MagEIS) fast sampling rate ( $\sim$ 11 ms),  
 738 and RBSP Ion Composition Experiment's (RBSPICE) PA coverage. The observed  
 739 microbursts' duration, energy spectra, and energy dispersion signature were similar to  
 740 microbursts previously reported from LEO. Furthermore, we simultaneously observed  
 741 structureless "hiss-like" whistler mode wave power in the lower band chorus frequency  
 742 range (Li et al., 2012). From previous observations in LEO (e.g. Blake et al., 1996),  
 743 it is believed that microbursts result from the impulsive scattering of electrons into  
 744 or near the loss cone, which is on the order of a few tens of degrees in LEO. With this  
 745 assumption, high altitude microburst observations near the magnetic equator should  
 746 be very difficult to make since the atmospheric loss cone there is only a few degrees  
 747 wide. Thus, the loss cone is smaller than the angular resolution of most particle  
 748 detectors. Even when an instrument is observing the loss cone, the instrument's field  
 749 of view will include some portion of the trapped population. The trapped electron flux  
 750 is typically orders of magnitude higher than that in the loss cone, so that microbursts  
 751 scattered into the loss cone will be obscured. We present observational evidence that  
 752 suggests that the sudden impulse of electrons studied here is consistent with the  
 753 creation of microbursts. Furthermore, these microbursts were scattered over a broad  
 754 PA range outside of the loss cone, though the loss cone was not directly observed by  
 755 MagEIS and RBSICE.

756 This paper explores the properties of the observed microbursts by utilizing in-  
 757 situ RBSP measurements of waves and particles. This unique high altitude point of  
 758 view enables us to test whether the observed microburst scattering is consistent with  
 759 a quasi-linear diffusion process. We have tested this hypothesis with in-situ electron

760 phase space density (PSD) measurements and the relativistic theory of wave-particle  
 761 resonant diffusion (Summers et al., 1998; Walker, 1993) to determine if the microburst  
 762 electrons diffused in PA and energy.

763 Spacecraft Instrumentation

764 NASA's RBSP mission (Mauk et al., 2013), launched on August 30th, 2012,  
 765 consists of a pair of identically instrumented spacecraft. Their orbit and instru-  
 766 mentation are uniquely configured to enrich our understanding of the particles and  
 767 waves in the inner magnetosphere. The RBSP spacecraft are in highly elliptical, low-  
 768 inclination orbit, with perigee of  $\sim$ 600 km and apogee of  $\sim$ 30,000 km altitude. Their  
 769 attitude is maintained by spin-stabilization with a period of  $\sim$ 11 s and the spin axis is  
 770 roughly sun-pointing. In this analysis, energetic electron measurements from MagEIS  
 771 (Blake et al., 2013) and RBSPICE (Mitchell et al., 2013) were used, complemented by  
 772 magnetic field and wave measurements from Electric and Magnetic Field Instrument  
 773 and Integrated Science (EMFISIS) (Kletzing et al., 2013).

774 We observed these microbursts with RBSP-A's MagEIS low energy instrument  
 775 (MagEIS-A) which measures 20-240 keV electrons. It has an angular acceptance  
 776 of  $3^\circ - 10^\circ$  in the spacecraft spin plane, and  $20^\circ$  perpendicular to the spin plane.  
 777 MagEIS-A has a high rate data mode which samples at 1000 angular sectors per  
 778 spacecraft spin (11 ms cadence). MagEIS low on RBSP-B on the other hand samples  
 779 at 64 angular sectors per spacecraft spin (172 ms cadence), so it was only used for  
 780 context.

781 To expand the PA coverage of MagEIS-A, we used the RBSPICE-A time-of-  
 782 flight instrument. RBSPICE-A measures electron energies in the range of 19 keV -  
 783 1 MeV with a fan of six telescopes (the sixth telescope is used only for calibration  
 784 and was excluded from this analysis). These telescopes have an overall acceptance

785 angle of  $160^\circ$  by  $12^\circ$  which allows them to simultaneously sample a substantial part  
 786 of the Pitch Angle Distribution (PAD). RBSPICE-A gathers data over 32 sectors  
 787 per spacecraft spin ( $\approx 310$  ms cadence) and each sector is divided into three sub-  
 788 sectors corresponding to three measurement modes (Manweiler and Zwiener, 2018).  
 789 At the time of the observation, the sub-sector used for electron measurements had  
 790 an accumulation time of 77 ms. We used RBSPICE-A's Electron Basic Rate (EBR)  
 791 telemetry data in this analysis which is not averaged, though it is an integral energy  
 792 channel.

793 To understand the dynamics of the local magnetic field, we used the EMFISIS  
 794 instrument. EMFISIS provides measurements of the DC magnetic field with flux gate  
 795 magnetometers. In addition, it measures electromagnetic waves from 10 Hz to 500  
 796 kHz with search coil magnetometers. The spectral matrix and burst data products  
 797 used in this analysis were from the EMFISIS waveform receiver (WFR) (10 Hz - 12  
 798 kHz) and the high frequency receiver (10 kHz - 500 kHz). Burst data were selectively  
 799 captured at a 35 kHz sample rate, and the survey mode spectral matrix data was  
 800 captured every 6s.

801

### Observations

802 MagEIS-A and RBSPICE-A observed the microburst-like signatures on March  
 803 31st, 2017 at  $L^* \approx 6$  and  $MLT \approx 19$ , calculated with the Tsyganenko 2004 magnetic  
 804 field model (Tsyganenko and Sitnov, 2005). The magnetosphere was in the recovery  
 805 phase of a storm, with minimum Dst of -75 nT observed on March 27th. The local  
 806 electron number density was on the order of  $1 \text{ cm}^{-3}$  at this time, so both RBSP  
 807 spacecraft were located outside the plasmasphere. The two spacecraft were separated  
 808 by 1700 km, at magnetic latitudes  $\lambda \approx -19^\circ$  and  $\lambda \approx -18^\circ$  for RBSP-A and RBSP-B,  
 809 respectively.

810 MagEIS-A observed microburst electron flux ( $J$ ) at energies  $\geq 92$  keV around  
 811 11:17 UT as shown in panel (a) in Fig. 2.1. For directional information, panel (b)  
 812 in Fig. 2.1 shows flux as a function of local pitch angle ( $\alpha_L$ ) and time for 46-66 keV  
 813 electrons. Electrons that traveled towards the northern hemisphere had  $\alpha_L < 90^\circ$  and  
 814 southern hemisphere had  $\alpha_L > 90^\circ$ . The interval between the two vertical dashed  
 815 black lines contain the four microbursts examined in this study. We observed these  
 816 microbursts at  $\alpha_L < 50^\circ$ , but MagEIS-A did not sample into the  $0^\circ$  loss cone.

817 Figure 2.1 panel (c) shows the EMFISIS WFR data from RBSP-A. Between  
 818 11:17:05 and 11:17:10 UT, we observed an isolated burst of whistler mode wave power  
 819 in the frequency range  $0.1 < \omega < 0.3 \Omega_{ce0}$ , where  $\Omega_{ce0}$  is the equatorial electron  
 820 gyrofrequency. No individual rising or falling tone elements were observed during  
 821 this period, and the waves appeared more “hiss-like” (e.g. Li et al., 2012). This wave  
 822 was near-parallel propagating (evidence shown in Appendix A) and about 10 minutes  
 823 later, weak chorus rising tone elements were observed (not shown).

824 Panels (d)-(f) in Fig. 2.1 are in the same format as panels (a)-(c), but for RBSP-  
 825 B. An injection or boundary was observed with RBSP-B at 11:16:50 UT and RBSP-A  
 826 observed a similar feature soon after 11:18 UT (not shown).

827 A zoomed-in version of Fig. 2.1 panels (a) and (b) is shown in Fig. 2.2. Panel  
 828 (a) shows the four microburst-like signatures observed between 11:17:10 and 11:17:12  
 829 UT, at energies up to 92 keV. The observed duration of the microbursts was 150  
 830 - 500 ms, and they did not arrive dispersed in energy, which indicates that they  
 831 were recently scattered near the spacecraft location. We use IRBEM-Lib, a library  
 832 dedicated to radiation belt modeling (Boscher et al., 2012), to calculate the mirror  
 833 point altitudes, which were found to be above LEO. Panel (b) shows the RBSPICE-  
 834 A EBR time series with the group of microbursts observed at the same time as  
 835 in panel (a). To understand the timing relationship between the MagEIS-A and

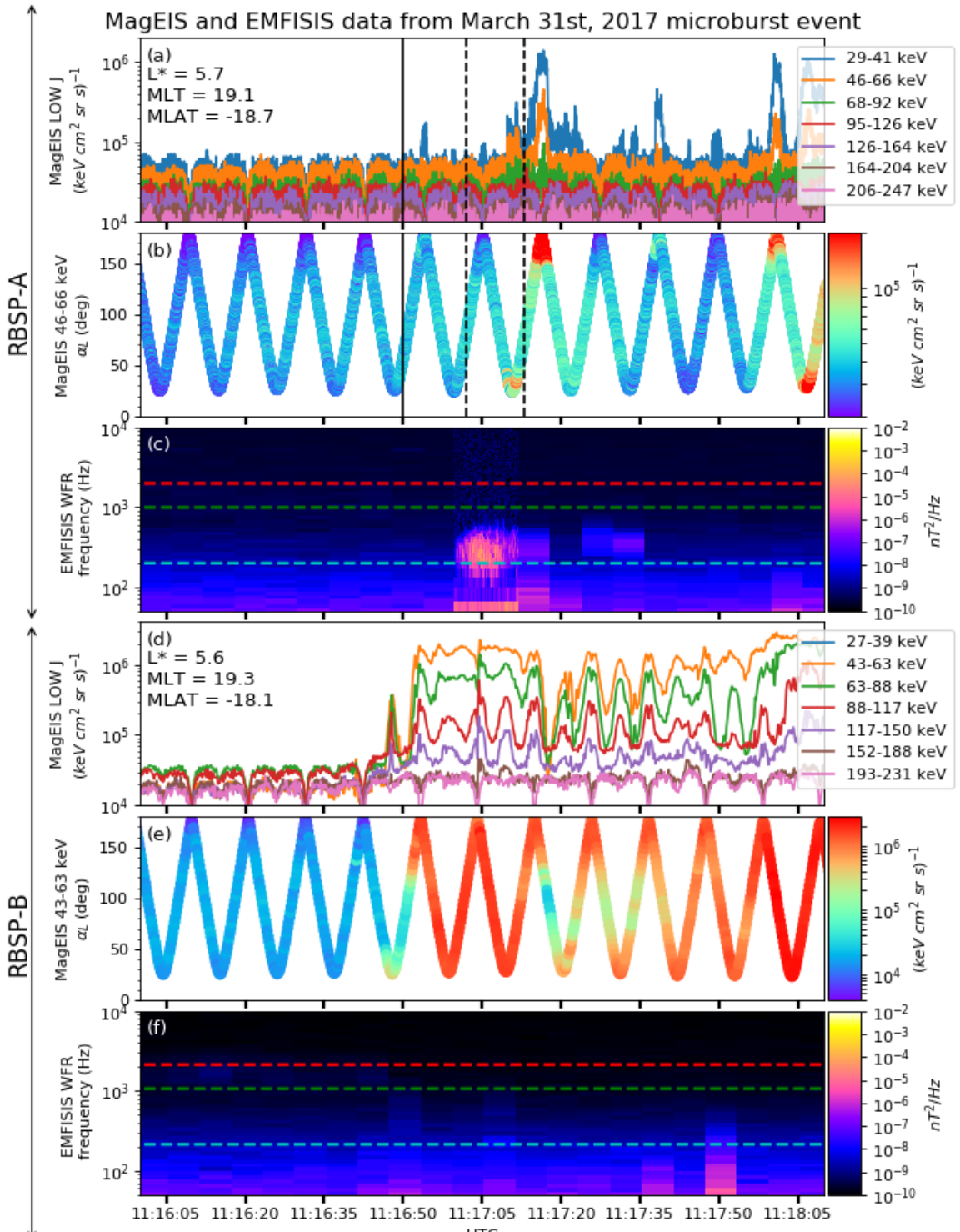


Figure 2.1: Electron and wave conditions from the MagEIS-A and EMFISIS WFR sensors for the microburst time interval. Panels (a), (b), and (c) are from RBSP-A with its position information annotated in panel (a). Panels (d), (e), and (f) are from RBSP-B with its position information annotated in panel (d). Panel (a) is the MagEIS-A high rate timeseries. Panels (b) and (e) show the evolution of the MagEIS-A  $J$  as a function of  $\alpha_L$  from the  $\sim 40$  to  $\sim 60$  keV channel. Every 10th point is shown in panel (b). The solid black line in panels (a) and (b) mark the end of the time period used for the PSD fit extrapolation analysis explained in section

836 RBSPICE-A observations, we marked the times when MagEIS-A observed the four  
 837 microbursts by vertical black arrows in panels (a) and (b). MagEIS-A observed the  
 838 first microburst  $\sim 0.5$  s before RBSPICE-A. The bounce period of locally mirroring,  
 839 100 keV electrons was  $\sim 0.8$  s, so this was unlikely to have been a returning bounce.  
 840 This evidence confirms that these microburst signatures are packets of electrons and  
 841 not a boundary moving back and forth at RBSP-A's location. To understand the  
 842 PA extent of these microbursts, panel (c) shows the 29-41 keV MagEIS-A  $J$  and  
 843 RBSPICE-A EBR as a function of  $\alpha_L$  and time. The microburst  $J$  was observed  
 844 by MagEIS-A between  $25^\circ < \alpha_L < 50^\circ$  and RBSPICE-A between  $100^\circ < \alpha_L < 160^\circ$ ,  
 845 with the highest intensities close to  $\alpha_L = 90^\circ$ . RBSPICE-A observed a 10-80%  
 846 enhancement in count rate over those PAs with the evidence presented in Appendix  
 847 A.  
 848

### Analysis

849 First, we estimated the microburst energy spectra. For each microburst shown in  
 850 Fig. 2.2, its flux was averaged and baseline subtracted using the method from O'Brien  
 851 et al. (2004) and then fit with an exponential function. The calculated exponential  
 852 E-folding energy was found to vary between 25 and 35 keV, which is consistent with  
 853 spectra derived from prior measurements (Datta et al., 1997; Lee et al., 2012, 2005).

854 We then tested the hypothesis that the microburst electrons were transported  
 855 in energy and PA by a single chorus wave. We used a procedure similar to sections  
 856 3.1 and 4.5 in Meredith et al. (2002) which we describe below.

### Microburst and Source PSD

857 We estimated the electron PSD,  $f(p_\perp, p_\parallel)$  where  $p_\perp$  and  $p_\parallel$  are the perpendicular  
 858 and parallel components of the electron momentum relative to the local magnetic field,

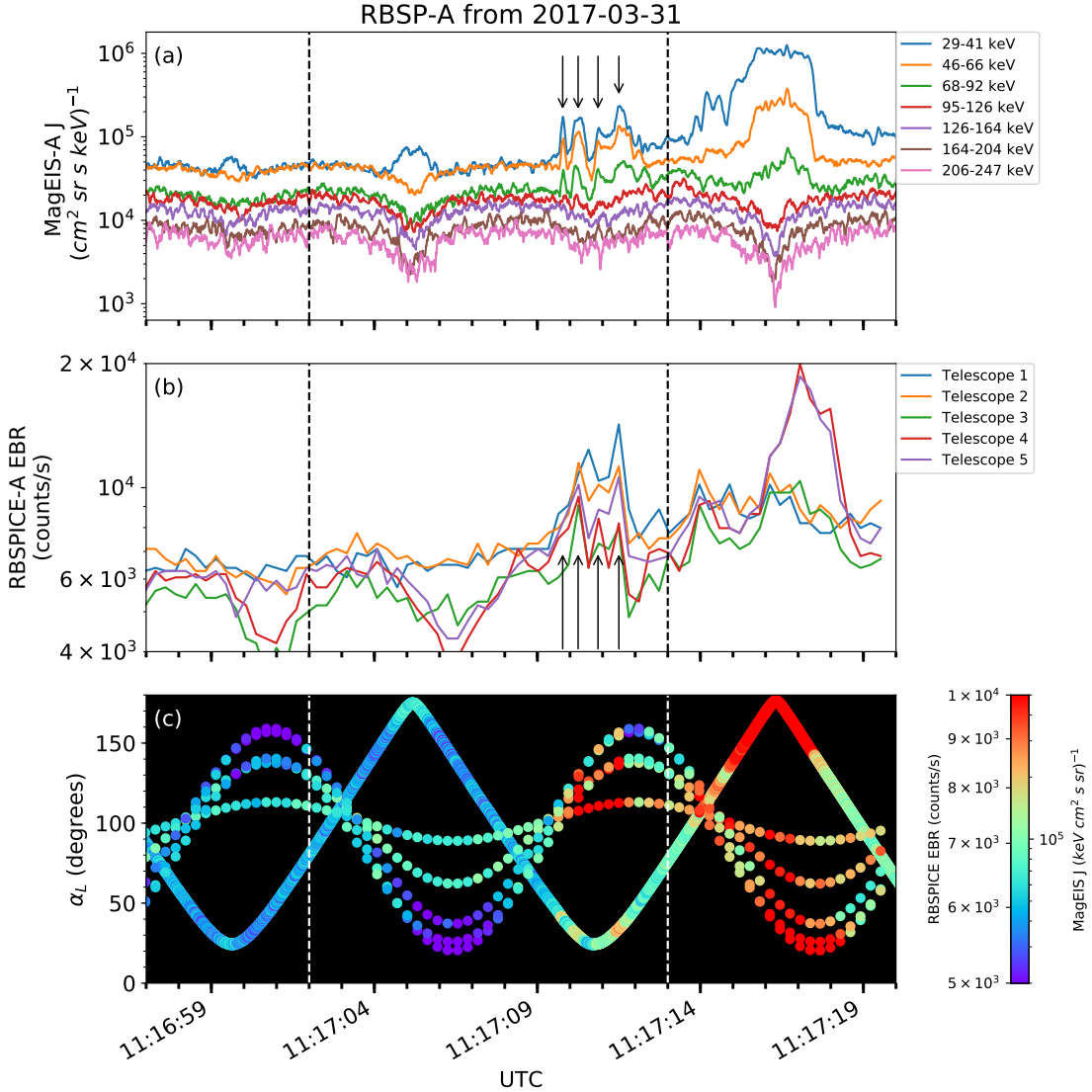


Figure 2.2: Panel (a) shows the MagEIS-A high rate timeseries. Panel (b) shows the RBSPIKE EBR count rate timeseries for  $\zeta = 19$  keV electrons. The microbursts were observed between 11:17:10 - 11:17:12 UT and are indicated with the vertical black arrows in panels (a) and (b) for MagEIS-A times. Panel (c) shows the RBSPIKE EBR (family of relatively sparse sampled curves) and MagEIS-A  $J$  from the 29-41 keV energy channel (single curve) as a function of  $\alpha_L$ . The vertical dashed lines show the time interval for the PSD analysis.

for the microburst time period. MagEIS-A  $J(E, \alpha_L)$  was averaged between 11:17:02 and 11:17:13 UT and binned by  $\alpha_L$  into  $5^\circ$  bins. Then, we assumed the conservation of the first adiabatic invariant and mapped  $\alpha_L$  to equatorial PA,  $\alpha_{eq}$ . The binned  $J(E, \alpha_{eq})$  was then converted to  $f(p_\perp, p_\parallel)$  via

$$f(p_\perp, p_\parallel) = \frac{J(E, \alpha_{eq})}{p^2}, \quad (2.1)$$

where  $p = \sqrt{p_\perp^2 + p_\parallel^2}$ . Lastly,  $\alpha_{eq}$  was used to separate  $p$  into  $p_\perp$  and  $p_\parallel$  via

$$\frac{p_\parallel}{m_e c} = \frac{\sqrt{E(E + 2E_0)} \cos(\alpha_{eq})}{E_0} \quad (2.2)$$

$$\frac{p_\perp}{m_e c} = \frac{\sqrt{E(E + 2E_0)} \sin(\alpha_{eq})}{E_0} \quad (2.3)$$

where  $c$  is the speed of light,  $E$  is the kinetic energy,  $m_e$  is the electron mass, and  $E_0$  is the electron rest energy. The observed  $f(p_\perp, p_\parallel)$  in dimensionless momentum space is shown in Fig. 2.3 in all panels between the  $p_\parallel$  axis and the white dotted lines. The bright spot in  $f(p_\perp, p_\parallel)$  in the upper  $p_\parallel$  plane represents the four microbursts. Along with the observed PSD, we use Fig. 2.3 to explore the various PSD extrapolation and diffusion model assumptions which are described below.

We proceed under the assumption that the source of the microburst electrons is not likely to be at the latitude of the observation, and is closer to the magnetic equator. To look for a source of microburst electrons, we extrapolate the unobserved  $f(p_\perp, p_\parallel)$  of electrons with  $|\lambda_m| < 19^\circ$  using two cases with a  $90^\circ$ -peaked PAD of the form

$$f(E, \alpha_{eq}) = f_0(E) \sin^n(\alpha_{eq}) \quad (2.4)$$

where  $f_0(E)$  is a scaling parameter and  $n$  is a power parameter. Similarly to the

872 in-situ  $f(p_{\perp}, p_{||})$ , the  $f(E, \alpha_{eq}) \mapsto f(p_{\perp}, p_{||})$  conversion was applied.

873 In the first case, we fitted Eq. 2.4 to the quiet time  $J(E, \alpha_{eq})$  from 11:15:00 to  
 874 11:16:50 UT (end time shown as the black vertical line in Fig. 2.1). The fitted  
 875 PAD was relatively flat with  $0.4 < n < 0.5$  and highest magnitude of  $f_0$  was  
 876  $0.05 \text{ cm}^3/(\text{cm MeV})^3$ . This extrapolated  $f(p_{\perp}, p_{||})$  is shown in Fig. 2.3 panels (A) and  
 877 (E), between the dotted white lines for scattering at  $\lambda = 0^\circ$  and  $20^\circ$ , respectively.  
 878 To confirm the relatively low  $n$  parameter, we found times where RBSP-A was in  
 879 a similar L-MLT location, but closer to the magnetic equator. At 2 and 19 UT on  
 880 the same day, we fit the  $J(E, \alpha_{eq})$ , and the fit parameters were very similar to the  
 881 pre-microburst  $f(p_{\perp}, p_{||})$  at 11 UT. Thus it is a reasonable assumption that  $f(p_{\perp}, p_{||})$   
 882 was relatively flat near the equator.

883 In the other case, we estimate how large  $n$  would have to be in order to find  
 884 sufficient PSD in MagEIS-A's energy range to be a source of the microburst electrons.  
 885 We used  $n \in \{1, 2, 4\}$  and we forced the  $f_0(E)$  parameter to match the observed  
 886  $f(p_{\perp}, p_{||})$  at the most equatorial PAs observed by MagEIS-A. These extrapolations  
 887 are shown in columns 2-4 in Fig. 2.3. There was enough source PSD anywhere in  
 888 MagEIS-A's energy range only if  $n \geq 2$ .

889 Motion of resonant electrons in phase space

To calculate the motion of resonant electrons in momentum space, we used the relativistic theory of wave-particle resonant diffusion developed by Walker (1993) and Summers et al. (1998) and applied in Meredith et al. (2002). The chorus wave can modify  $f(p_{\perp}, p_{||})$  when a resonance condition is satisfied. The cyclotron resonance condition between an electron with velocity  $v = \sqrt{v_{||}^2 + v_{\perp}^2}$  and a parallel propagating

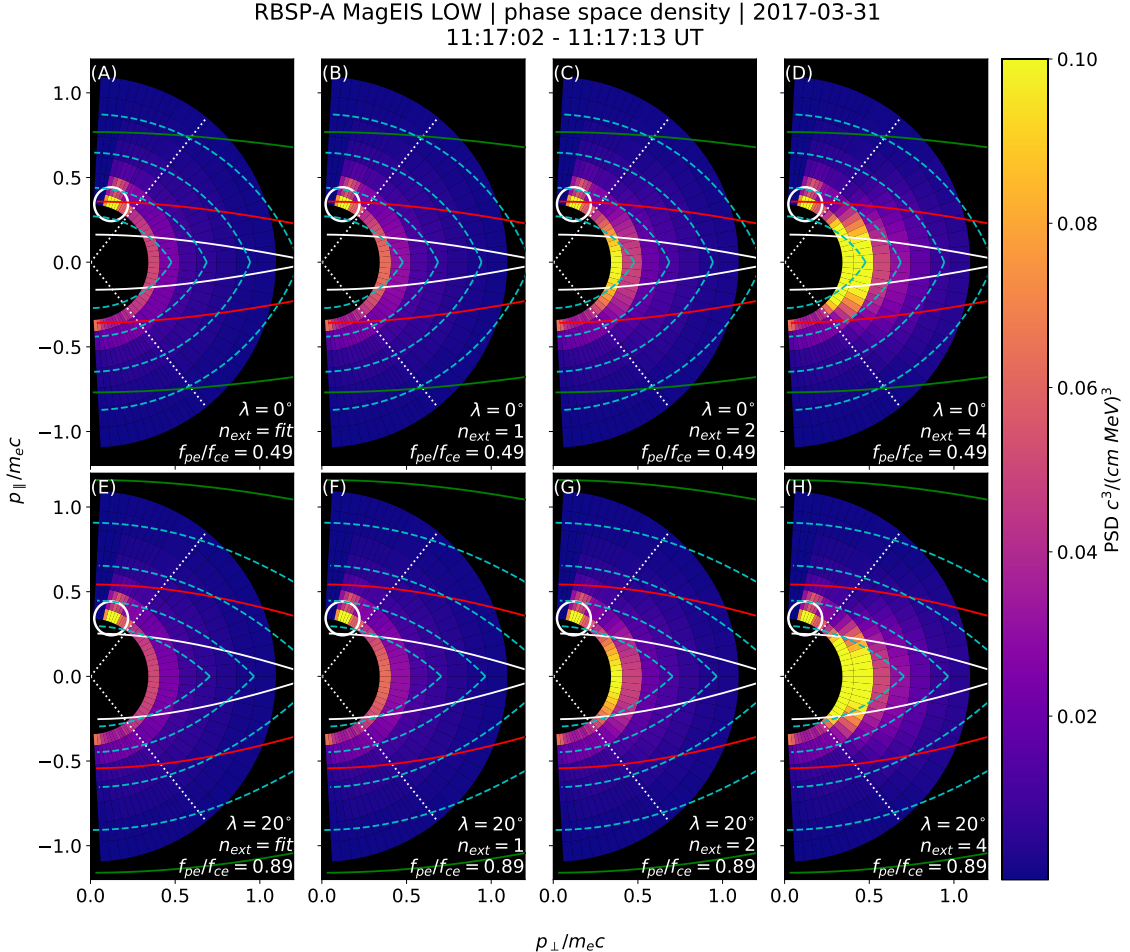


Figure 2.3: The colored annulus represents  $f(p_{\perp}, p_{\parallel})$  in normalized momentum space, parallel and perpendicular to the background magnetic field. The microburst  $f(p_{\perp}, p_{\parallel})$  is highlighted with the white circle. The columns show different powers of the sine extrapolation, and rows show the different magnetic latitudes of the scattering. The white dotted traces represent the boundary between the data and extrapolation. The green, red, and white solid traces are the resonance curves for  $\omega = 0.2\Omega_{ce}$ ,  $0.4\Omega_{ce}$ ,  $0.6\Omega_{ce}$ , respectively. The cyan dashed traces are the diffusion curves for a  $\omega = 0.4\Omega_{ce}$  wave (waves of other frequency have similar diffusion curves). The magnetic latitude of the scattering, the ratio of the plasma to the cyclotron frequency, and the power of the sine extrapolation is annotated in each panel. For the resonance and diffusion curves, the density model assumed a  $n_L = 1 e^-/cm^3$  and  $\psi = -1$ .

wave of frequency  $\omega$  and wave number  $k_{\parallel}$  is given by

$$\omega - v_{\parallel} k_{\parallel} = \frac{\Omega_{ce}}{\gamma}, \quad (2.5)$$

where  $\Omega_{ce}$  is the electron gyrofrequency at the scattering location, and  $\gamma$  is the relativistic correction. Assuming the cold plasma approximation,

$$k_{\parallel} = \frac{\omega}{c} \sqrt{1 - \frac{\omega_{pe}^2}{\omega(\omega - |\Omega_{ce}|)}}, \quad (2.6)$$

where  $\omega_{pe}$  is the plasma frequency. For a particular set of parameters, Eq. 2.5 defines a curve in momentum space that describes which electrons will resonate with a monochromatic wave.

To calculate  $k_{\parallel}$ , we approximated the electron number density,  $n_e(\lambda)$  locally and at the magnetic equator. Locally, the plasma density was approximately  $n_e(\lambda = -20^\circ) = n_L \approx 1 \text{ cm}^{-3}$ . We used magnetospheric seismology techniques (e.g. Takahashi and Denton, 2007) to parameterize  $n_e(\lambda)$  elsewhere along the field line with

$$n_e(\lambda) = n_e(0) \left( \frac{LR_e}{R(\lambda)} \right)^{\psi} \quad (2.7)$$

where  $R_e$  is the Earth's radius,  $R(\lambda)$  is the radial distance from the Earth to the spacecraft, and  $\psi$  is the exponent parameter. Assuming a dipole magnetic field for which  $R(\lambda) = LR_e \cos^2 \lambda$  (e.g. Schulz and Lanzerotti, 1974), we can express Eq. 2.7 in terms of  $n_L$  via

$$n_e(\lambda) = n_L \left( \frac{\cos \lambda_L}{\cos \lambda} \right)^{2\psi} \quad (2.8)$$

where we used  $\psi = -1$  (higher density at the magnetic equator) in this analysis. We chose this exponent parameter because it is a realistic best case scenario for the

900 electrons to be transported along the diffusion curves (described below).

Walker (1993) and Summers et al. (1998) argued that a resonant electron will move along diffusion curves in momentum space. A diffusion curve is derived as follows. In the reference frame moving with a monochromatic chorus wave's phase velocity (wave frame), the chorus wave is stationary and there is no electric field. Thus in the wave frame, the electron's kinetic energy is conserved, and the electron's velocity in the wave frame can be expressed in differential form as

$$v_{\parallel}dv_{\parallel} + v_{\perp}dv_{\perp} = 0. \quad (2.9)$$

After a Lorentz transformation of Eq. 2.9 into the magnetosospheric frame, kinetic energy will no longer be conserved. After integration and manipulation of Eq. 2.9, we obtain:

$$\left(1 - \frac{u_0^2 v_0^2}{c^4}\right)v_{\parallel}^2 - 2u_0\left(1 - \frac{v_0^2}{c^2}\right)v_{\parallel} + \left(1 - \frac{u_0^2}{c^2}\right)v_{\perp}^2 = v_0^2 - u_0^2 \quad (2.10)$$

901 where  $u_0 = \omega/k_{\parallel}$  is the phase velocity, and  $v_0$  is a constant of integration (Summers  
 902 et al., 1998; Walker, 1993). Equation 2.10 defines a family of diffusion curves in  
 903 momentum space on which resonant electrons will move. The distance that an  
 904 electron moves along a diffusion curve is a function of wave and plasma parameters,  
 905 and is estimated from the magnitude of the diffusion coefficients and the resonance  
 906 time.

907 Comparing the microburst PSD to diffusion theory

908 Superposed on the PSD plots in Fig. 2.3 are resonance curves for chorus waves  
 909 of  $\omega = 0.2\Omega_{ce}$ ,  $0.4\Omega_{ce}$ ,  $0.6\Omega_{ce}$  and a few diffusion curves for a  $\omega = 0.4\Omega_{ce}$  wave.  
 910 These curves were parameterized by  $\lambda$  using a dipole magnetic field for  $\lambda = 0^\circ$

(Fig. 2.3, panels A-D) and  $\lambda = 20^\circ$  (Fig. 2.3, panels E-H). If the transport of microburst electrons is consistent with gyro-resonant diffusion, a diffusion curve that passes through the microburst  $f(p_\perp, p_\parallel)$  must also pass through another region with at least the same magnitude PSD ( $f(p_\perp, p_\parallel) \geq 0.1 \text{ c}^3/(\text{cm MeV})^3$ ) e.g. Fig. 2.3, panel (D). With this constraint, an artificially high extrapolated  $f(p_\perp, p_\parallel)$  with  $n > 2$  (5 times larger than calculated from the fits) must be assumed for there to have been a sufficient source of PSD anywhere in MagEIS-A's energy range.

We now show that by comparing MagEIS observations with theory, that the minimum wave amplitude necessary to scatter these electrons is much higher than was observed by EMFISIS-A. If we assume a unrealistic PAD with enough PSD just equatorward of RBSP-A, we can use MagEIS-A observations to calculate the minimum  $\Delta\alpha_{eq}$  that the electrons were transported. We then used diffusion theory to calculate the necessary wave amplitude. For microbursts with larger PAs, MagEIS-A observed a transport of  $\Delta\alpha_{eq} = 9^\circ$  and for microbursts with smaller PAs, the observed transport was  $\Delta\alpha_{eq} = 24^\circ$ . The required wave amplitude was calculated with Eq. 3 from Thorne and Andreoli (1981) assuming a maximum resonance period of a quarter bounce. The observed change in PA requires a wave amplitude  $0.2 < |B_w| < 0.5 \text{ nT}$ . For a few brief moments, the EMFISIS-A WFR waveform data showed  $0.1 < |B_w| < 0.15 \text{ nT}$ , so a transport of  $9^\circ$  is plausible, but not likely for  $24^\circ$ .

Another source of microburst electrons may be from energies below MagEIS-A's range. The Helium, Oxygen, Proton, and Electron mass spectrometer (Funsten et al., 2013) on RBSP-A observed  $f(p_\perp, p_\parallel) \geq 0.1 \text{ c}^3/(\text{cm MeV})^3$  for  $\gtrsim 23 \text{ keV}$  electrons at this time. We then assumed the wave amplitude derived above to predict the transport in energy. We used the fact that the momentum and pitch angle diffusion coefficients,  $D_{pp}$  and  $D_{\alpha\alpha}$  are related via  $D_{pp}/p^2 \sim D_{\alpha\alpha}$  or equivalently,  $\Delta p/p \sim \Delta\alpha$ . The observed PA transport corresponds to an energy transport of  $6 < \Delta E < 16$

937 keV. Therefore, this wave can transport 23 keV electrons from smaller pitch angles  
 938 to larger pitch angles and would be observed in the 29 – 41 keV MagEIS-A channel.  
 939 However, this wave is insufficient to transport electrons to the 68 – 92 keV channel  
 940 in one interaction. Therefore we conclude that quasi-linear diffusion cannot explain  
 941 the observed microbursts.

942

### Discussion and Conclusions

943 These novel observations of impulsive electron signatures reported here fall  
 944 well within the broad definition of a microburst as described in section 3. Their  
 945 properties were similar to microbursts observed in LEO, with an E-folding energy of  
 946  $25 < E_0 < 35$  keV (Datta et al., 1997; Lee et al., 2012, 2005), duration of 150-500  
 947 ms (Lorentzen et al., 2001a), observed upper energy limit of 92 keV, and a lack of  
 948 clear energy dispersion (Breneman et al., 2017). With MagEIS-A’s high time and  
 949 energy resolution, we conclude that these dispersionless microbursts were recently  
 950 scattered near the spacecraft. Furthermore, RBSPICE-A’s PA coverage suggests  
 951 that these electrons were scattered over a substantial range of PAs, with the highest  
 952 intensities near  $\alpha_L = 90^\circ$ . Overall, our observational evidence suggests that on time  
 953 scales shorter than one bounce period, the chorus wave effectively accelerated trapped  
 954 electrons over a broad PA range.

955 In the theoretical framework of wave-particle resonant diffusion applied to the  
 956 observed PSD in section 3, we determine that the observed scattering is not consistent  
 957 with the quasi-linear approximation. The nearest source of sufficient PSD is too  
 958 far away in phase space to have been transported by the hypothesized quasi-linear  
 959 process over a timescale shorter than one bounce period (one interaction). A similar  
 960 conclusion was made by Mozer et al. (2018) who used quasi-linear theory constrained  
 961 by RBSP wave measurements. They successfully modeled the one second average

962 precipitating flux observed with AeroCube-6 (AC-6) CubeSats during a conjunction,  
 963 but they were unable to model the AC-6 fluxes on smaller time scales.

964 To put these microburst observations into a wider magnetospheric perspective,  
 965 we observed them during the recovery phase of a minimum Dst of -75 nT storm, a  
 966 statistically favorable time period for microbursts (O'Brien et al., 2003). Furthermore,  
 967 during the same storm on March 27th, the Arase spacecraft observed highly correlated  
 968 lower band chorus with 10-50 keV electron precipitation inside the loss cone. At  
 969 that time, Arase's magnetic field footprint was near The Pas All-Sky Imager (part  
 970 of the THEMIS mission) which simultaneously observed pulsating auroral patches  
 971 (Kasahara et al., 2018). While microbursts and pulsating auroral patches have not  
 972 been clearly connected, they are both believed to be a product of electron scattering  
 973 by whistler mode waves (e.g. Lorentzen et al., 2001a; Nishimura et al., 2011; O'Brien  
 974 et al., 2003; Ozaki et al., 2012).

975 The combined capabilities of the various RBSP wave and particle instruments  
 976 enable comprehensive studies of wave-particle scattering and the resulting microburst  
 977 precipitation. From a preliminary search by the authors, other microburst-like  
 978 signatures have been found with RBSP. Similar to previous studies (e.g. Blum et al.,  
 979 2015; O'Brien et al., 2003), a statistical study of high-altitude microbursts in L-MLT  
 980 space needs to be conducted before we can verify that these microbursts are the  
 981 counterpart of the microbursts observed in LEO and the upper atmosphere.

982 Acknowledgments

983 The authors acknowledge the technicians, engineers, and scientists who made the  
 984 RBSP and AC-6 missions possible. One author (Shumko) would like to acknowledge  
 985 Dana Longcope for his help in understanding the quasi-linear diffusion theory. Dr.  
 986 Gkioulidou was supported by JHU/APL subcontract 131803 to the NJIT under NASA

987 Prime contract NNN06AA01C. EMFISIS work was supported by JHU/APL contract  
988 no. 921647 under NASA Prime contract No. NAS5-01072. The MagEIS instrument  
989 was funded by NASA's Prime contract no. NAS5-01072. The level 3 MagEIS-A  
990 "high rate" data is available in the Supporting Information, level 1 RBSPICE EBR  
991 data is archived at <http://rbspicea.ftecs.com/>, and the EMFISIS level 2 spectral  
992 matrix and burst data as well as the level 3 magnetometer data is archived at  
993 <http://emfisis.physics.uiowa.edu/data/index>. The IRBEM Library can be obtained  
994 at [irbem.sf.net](http://irbem.sf.net).

## 995 CHAPTER THREE

996 MICROBURST SCALE SIZE DERIVED FROM MULTIPLE BOUNCES OF A  
997 MICROBURST SIMULTANEOUSLY OBSERVED WITH THE FIREBIRD-II  
998 CUBESATS

999 Contribution of Authors and Co-Authors

1000 Manuscript(s) in Chapter(s) 1

1001

1002 Author: [type author name here]

1003 Contributions: [list contributions here, single-spaced]

1004 Co-Author: [type co-author name here]

1005 Contributions: [list contributions here, single-spaced]

1006 Co-Author: [type co-author name here]

1007 Contributions: [list contributions here, single-spaced]

1008

1009

Manuscript Information

1010 [Type Author and Co-author(s) Names Here]

1011 Geophysical Research Letters

1012 Status of Manuscript: Published in a peer-reviewed journal

1013 Wiley

1014 Volume 45, Issue 17

1015

1016 This article is available under the terms of the Creative Commons Attribution  
1017 Non-Commercial No Derivatives License CC BY-NC-ND (which may be updated  
1018 from time to time) and permits non-commercial use, distribution, and reproduction  
1019 in any medium, without alteration, provided the original work is properly cited and  
1020 it is reproduced verbatim.

1021

Key Points

1022

- Multiple bounces from a microburst were observed by the two FIREBIRD-II CubeSats at LEO.
- The lower bounds on the microburst scale size at LEO were  $29 \pm 1$  km (latitudinal) and  $51 \pm 11$  km (longitudinal).
- Deduced lower bound equatorial scale size was similar to the whistler-mode chorus source scale.

1028

Abstract

1029

We present the observation of a spatially large microburst with multiple bounces made simultaneously by the FIREBIRD-II CubeSats on February 2nd, 2015. This is the first observation of a microburst with a subsequent decay made by two co-orbiting but spatially separated spacecraft. From these unique measurements, we place estimates on the lower bounds of the spatial scales as well as quantify the electron bounce periods. The microburst's lower bound latitudinal scale size was  $29 \pm 1$  km and the longitudinal scale size was  $51 \pm 1$  km in low earth orbit. We mapped these scale sizes to the magnetic equator and found that the radial and azimuthal scale sizes were at least  $500 \pm 10$  km and  $530 \pm 10$  km, respectively. These lower bound equatorial scale sizes are similar to whistler-mode chorus wave source scale sizes, which supports the hypothesis that microbursts are a product of electron scattering by chorus waves. Lastly, we estimated the bounce periods for 200-800 keV electrons and found good agreement with four common magnetic field models.

1042

Introduction

1043       The dynamics of radiation belt electrons are complex, and are driven by  
 1044 competition between source and loss processes. A few possible loss processes are  
 1045 radial diffusion (Shprits and Thorne, 2004), magnetopause shadowing (Ukhorskiy  
 1046 et al., 2006), and pitch angle and energy diffusion due to scattering of electrons by  
 1047 plasma waves (e.g. Abel and Thorne, 1998; Horne and Thorne, 2003; Meredith et al.,  
 1048 2002; Mozer et al., 2018; Selesnick et al., 2003; Summers et al., 1998; Thorne et al.,  
 1049 2005). There are a variety of waves that cause pitch angle scattering, including  
 1050 electromagnetic ion cyclotron waves, plasmaspheric hiss, and chorus (Millan and  
 1051 Thorne, 2007; Thorne, 2010). Chorus predominantly occurs in the dawn sector (6-12  
 1052 magnetic local times (MLT)) (Li et al., 2009b) where it accelerates electrons with  
 1053 large equatorial pitch angles and scatters electrons with small equatorial pitch angles  
 1054 (Horne and Thorne, 2003). Some of these electrons may be impulsively scattered  
 1055 into the loss cone, where they result in short-duration ( $\sim 100$  ms) enhancements in  
 1056 precipitating flux called microbursts.

1057       Anderson and Milton (1964) coined the term microburst to describe high altitude  
 1058 balloon observations of  $\sim 100$  ms duration enhancements of bremsstrahlung X-  
 1059 rays emitted from scattered microburst electrons impacting the atmosphere. Since  
 1060 then, non-relativistic (less than a few hundred keV) microbursts have been routinely  
 1061 observed with other balloon missions (e.g. Anderson et al., 2017; Parks, 1967; Woodger  
 1062 et al., 2015). A review of the literature shows no reports of microbursts above a few  
 1063 hundred keV observed by balloons (Millan et al., 2002; Woodger et al., 2015). This  
 1064 lack of observation may be explained by relatively weaker pitch angle scattering of  
 1065 relativistic electrons by chorus (Lee et al., 2012).

1066       In addition to the X-ray signature for bursts of electron precipitation, the

1067 precipitating relativistic and non-relativistic electrons have been measured in situ by  
 1068 spacecraft orbiting in low earth orbit (LEO). Hereinafter, we refer to these electron  
 1069 signatures observed by LEO spacecraft also as microbursts. Microbursts have been  
 1070 observed with, e.g. the Solar Anomalous and Magnetospheric Particle Explorer's  
 1071 (SAMPEX)  $\gtrsim$  150 keV and  $\gtrsim$  1 MeV channels (Blake et al., 1996; Blum et al., 2015;  
 1072 Lorentzen et al., 2001a,b; Nakamura et al., 1995, 2000; O'Brien et al., 2004, 2003) and  
 1073 Focused Investigation of Relativistic Electron Bursts: Intensity, Range, and Dynamics  
 1074 (FIREBIRD-II) with its  $\gtrsim$  200 keV energy channels (Anderson et al., 2017; Breneman  
 1075 et al., 2017; Crew et al., 2016).

1076 Understanding microburst precipitation and its scattering mechanism is impor-  
 1077 tant to radiation belt dynamics. The scattering mechanism has been observationally  
 1078 studied by e.g. Lorentzen et al. (2001b) who found that microbursts and chorus  
 1079 waves predominantly occur in the dawn sector and Breneman et al. (2017) made  
 1080 a direct observational link between individual microbursts and chorus elements.  
 1081 Microbursts have been modeled and empirically estimated to be capable of depleting  
 1082 the relativistic electron population in the outer radiation belt on the order of a day  
 1083 (Breneman et al., 2017; O'Brien et al., 2004; Shprits et al., 2007; Thorne et al., 2005).  
 1084 An important parameter in this estimation of instantaneous radiation belt electron  
 1085 losses due to microbursts is their scale size. Parks (1967) used balloon measurements  
 1086 of bremsstrahlung X-rays to estimate the high altitude scale size of predominantly low  
 1087 energy microbursts to be  $40 \pm 14$  km. In Blake et al. (1996) a microburst with multiple  
 1088 bounces was observed by SAMPEX, and the microburst's latitudinal scale size in LEO  
 1089 was estimated to have been "at least a few tens of kilometers". Blake et al. (1996)  
 1090 concluded that typically microbursts are less than a few tens of electron gyroradii in  
 1091 size (at  $L = 5$  at LEO, the gyroradii of 1 MeV electrons is on the order of 100 m).  
 1092 Dietrich et al. (2010) used SAMPEX along with ground-based very low frequency

1093 stations to conclude that during one SAMPEX pass, the observed microbursts had  
1094 scale sizes less than 4 km.

1095 Since February 1st, 2015, microbursts have been observed by FIREBIRD-II, a  
1096 pair of CubeSats in LEO. Soon after launch, when the two FIREBIRD-II spacecraft  
1097 were at close range, a microburst with a scale size greater than 11 km was observed  
1098 (Crew et al., 2016). On the same day, FIREBIRD-II simultaneously observed a  
1099 microburst with multiple bounces. The microburst decay was observed over a period  
1100 of a few seconds, while the spacecraft were traveling predominantly in latitude. Here  
1101 we present the analysis and results of the latitude and longitude scale sizes and  
1102 bounce periods of the first microburst with multiple bounces observed with the two  
1103 FIREBIRD-II spacecraft.

1104 Spacecraft and Observation

1105 The FIREBIRD missions are comprised of a pair of identically-instrumented  
1106 1.5U CubeSats (15 x 10 x 10 cm) that are designed to measure electron precipitation  
1107 in LEO (Klumpar et al., 2015; Spence et al., 2012). The second mission, termed  
1108 FIREBIRD-II, was launched on January 31st 2015. The two FIREBIRD-II CubeSats,  
1109 identified as Flight Unit 3 (FU3) and Flight Unit 4 (FU4), were placed in a 632 km  
1110 apogee, 433 km perigee, and 99° inclination orbit (Crew et al., 2016). FU3 and FU4  
1111 are orbiting in a string of pearls configuration with FU4 ahead, to resolve the space-  
1112 time ambiguity of microbursts. Each FIREBIRD-II unit has two solid state detectors:  
1113 one is mounted essentially at the spacecraft surface, covered only by a thin foil acting  
1114 as a sun shade, with a field of view of 90° (surface detector), and the other is beneath  
1115 a collimator which restricts the field of view to 54° (collimated detector). Only FU3  
1116 has a functioning surface detector, so this analysis utilizes the collimated detectors.  
1117 FU3's surface and collimated detectors, as well as FU4's collimated detector observe

1118 electron fluxes in six energy channels from  $\sim 230$  keV to  $> 1$  MeV. FIREBIRD-II's  
 1119 High Resolution (HiRes) electron flux data is gathered with an adjustable sampling  
 1120 period of 18.75 ms by default and can be as fast as 12.5 ms.

1121 On February 2nd, 2015 at 06:12 UT, both FIREBIRD-II spacecraft simulta-  
 1122 neously observed an initial microburst, followed by subsequent periodic electron  
 1123 enhancements of diminishing amplitude shown in Fig. 3.1. This is thought to be  
 1124 the signature of a single burst of electrons, some of which precipitate, but the rest  
 1125 mirror near the spacecraft then bounce to the conjugate hemisphere where they mirror  
 1126 again and the subsequent bounces produce a train of decaying peaks (Blake et al.,  
 1127 1996; Thorne et al., 2005). This bounce signature occurred during the transition  
 1128 between the main and recovery phases of a storm with a minimum Dst of -44 nT  
 1129 ( $K_p = 4$ , and  $AE \approx 400$  nT). At this time, the HiRes data was sampled at 18.75 ms.  
 1130 Five peaks were observed by both spacecraft. The fifth peak observed by FU4 was  
 1131 comparable to the Poisson noise and was not used in this analysis. This microburst  
 1132 was observed from the first energy channel ( $\approx 200 - 300$  keV), to the fourth energy  
 1133 channel ( $\approx 500 - 700$  keV), and FU3's surface detector observed the microburst up  
 1134 to the fifth energy channel (683 - 950 keV).

1135 The HiRes data in Fig. 3.1 shows signs of energy dispersion, characterized by  
 1136 higher energy electrons arriving earlier than the lower energies. This time of flight  
 1137 energy dispersion tends to smear out the initial sharp burst upon each subsequent  
 1138 bounce. The first peak does not appear to be dispersed, and subsequent peaks show  
 1139 a dispersion trend consistent across energy channels. The black vertical bars have  
 1140 been added to Fig. 3.1 to highlight this energy dispersion. This dispersion signature  
 1141 and amplitude decay implies that the first peak was observed soon after the electrons  
 1142 were scattered, followed by decaying bounces.

1143 At this time, in magnetic coordinates, FIREBIRD-II was at McIlwain  $L = 4.7$

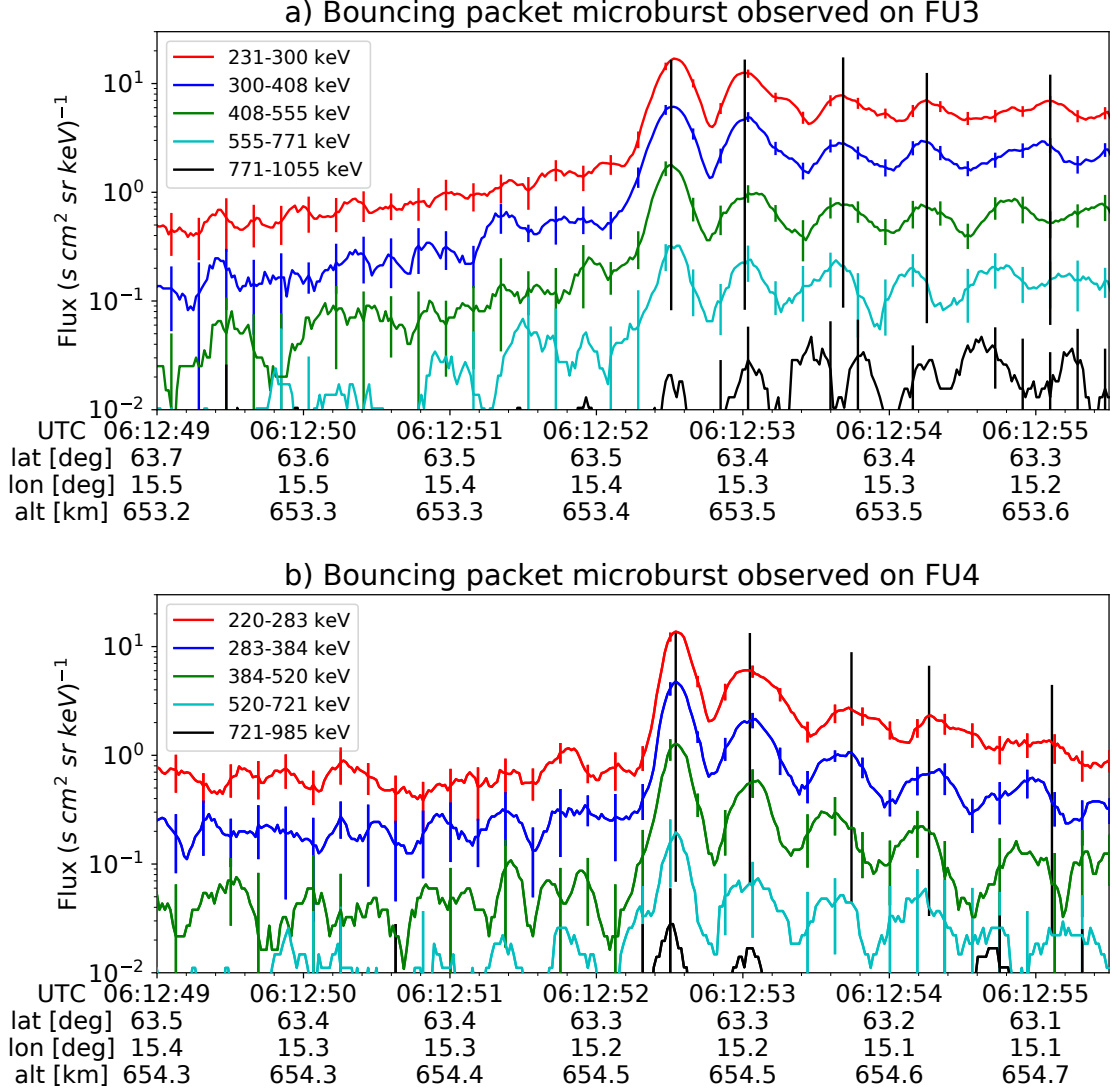


Figure 3.1: HiRes data of the microburst observed at February 2nd, 2015 at 06:12:53 UT, smoothed with a 150 ms rolling average. The subsequent bounces showed some energy dispersion. As discussed in Appendix B, a time correction of -2.28 s was applied to FU3. While the flux from five energy channels is shown, only channels with reasonable counting statistics were used for the spatial scale analysis. Vertical colored bars show the  $\sqrt{N}$  error every 10th data point and vertical black bars are lined up with the peaks in the 220-283 keV energy channel to help identify dispersion.

and MLT = 8.3, calculated with the Tsyganenko 1989 (T89) magnetic field model (Tsyganenko, 1989) using IRBEM-Lib (Boscher et al., 2012). Geographically, they were above Sweden, latitude = 63°N, longitude = 15°E, altitude = 650 km. This geographic location is magnetically conjugate to the east of the so-called South Atlantic Anomaly (SAA). The SAA is the location where the mirror points of electrons tend to occur at locations deeper in the atmosphere owing to the offset of the dipole magnetic field from the Earth's center. Electrons with pitch angles within the drift loss cone (DLC) will encounter the SAA and be removed from their eastward longitudinal drift paths (Comess et al., 2013; Dietrich et al., 2010). FU3 and FU4 are therefore both in regions where the particles in the DLC have recently precipitated, leaving only particles that were recently scattered. At the spacecraft location, locally mirroring electrons would have mirrored at 95 km in the opposite hemisphere, with more field aligned electrons mirroring at even lower altitudes. From the analysis done by Fang et al. (2010), the peak in the total ionization rate in the atmosphere for 100 keV electrons is around 80 km altitude, while the total ionization rate from 1 MeV electrons peaks around 60 km altitude. It is, therefore, expected that a fraction of the microburst electrons will survive each encounter with the atmosphere. By plotting the peak flux as a function of bounce (not shown), it was found that 40 - 60 % of the microburst electrons were lost on the first bounce, similar to the 33% loss per bounce observed for a bouncing microburst observed by SAMPEX (Thorne et al., 2005).

1164

### Analysis

At the beginning of the FIREBIRD-II mission, two issues prevented the proper analysis of the microburst's spatial scale size: the spacecraft clocks were not synchronized, and their relative positions were not accurately known. We addressed these issues with a cross-correlation time lag analysis described in detail in Appendix

1169 B. From this analysis, the time correction was  $2.28 \pm 0.12$  s (applied to Fig. 3.1) and  
 1170 the separation was  $19.9 \pm 0.9$  km at the time of the microburst observation.

1171 Electron Bounce Period

1172 We used this unique observation of bouncing electrons to calculate the bounce  
 1173 period,  $t_b$  as a function of energy and compare it to the energy-dependent  $t_b$  curves  
 1174 derived from four magnetic field models, the results of which are shown in Fig. 3.2.  
 1175 The observed  $t_b$  and uncertainties were calculated by fitting the baseline-subtracted  
 1176 HiRes flux. The baseline flux used in this analysis is given in O'Brien et al. (2004)  
 1177 as the flux at the 10th percentile over a specified time interval, which in this analysis  
 1178 was taken to be 0.5 seconds. The flux was fitted with a superposition of Gaussians  
 1179 for each energy channel, and the uncertainty in flux was calculated using the Poisson  
 1180 error from the microburst and baseline fluxes summed in quadrature. Using the fit  
 1181 parameters, the mean  $t_b$  for the lowest four energy channels is shown in Fig. 3.2. The  
 1182 trend of decreasing  $t_b$  as a function of energy is evident in Fig. 3.2, which further  
 1183 supports the assumption that the subsequent peaks are bounces, and not a train of  
 1184 microbursts scattered by bouncing chorus.

1185 The decaying peaks in the 231-408 keV electron flux observed by FU3's lowest  
 1186 two energy channels (see Fig. 3.1) were right-skewed. One explanation is that there  
 1187 was in-channel energy dispersion within those channels. Since  $t_b$  of higher energy  
 1188 electrons is shorter, a right-skewed peak implies that higher energy electrons were  
 1189 more abundant within that channel e.g. in FU3's 231-300 keV channel, the 300 keV  
 1190 electrons will arrive sooner than the 231 keV electrons, but will they will be binned  
 1191 in the same channel. A Gaussian fit cannot account for this in-channel dispersion,  
 1192 and as a first order correction, minima between peaks was used to calculate  $t_b$ , and  
 1193 is shown in Fig. 3.2. The observed energy-dependent dispersion shown in Fig. 3.2

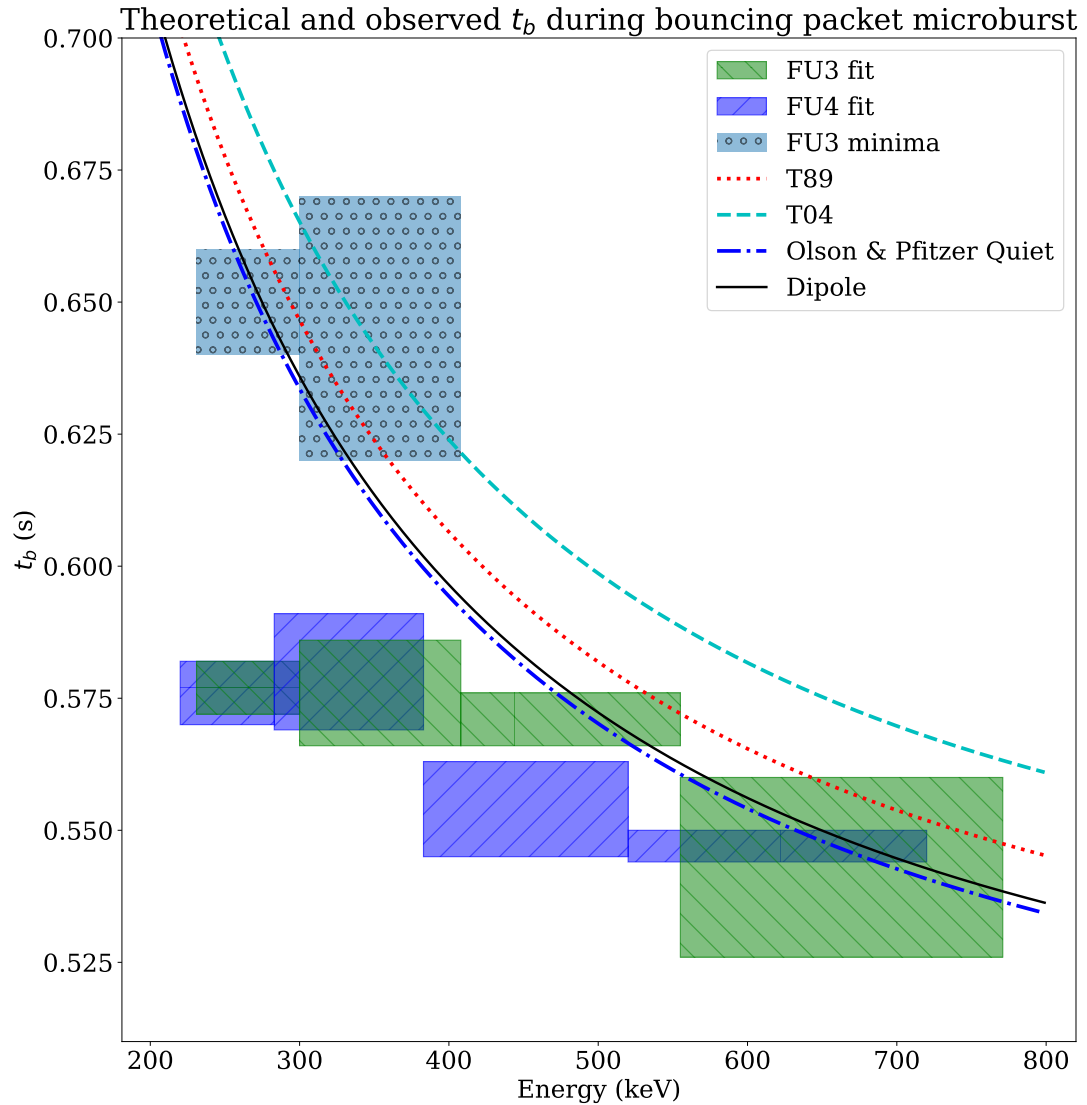


Figure 3.2: Observed and theoretical  $t_b$  for electrons of energies from 200 to 770 keV. The solid black line is  $t_b$  in a dipole magnetic field, derived in Schulz and Lanzerotti (1974). The red dotted and cyan dashed lines are the  $t_b$  derived using the T89, and T04 magnetic field models with IRBEM-Lib. Lastly, the blue dot-dash curve is the  $t_b$  derived using the Olson & Pfitzer Quiet model. The green and purple rectangles represent the observed  $t_b$  for FU3 and FU4 using a Gaussian fit, respectively. The blue rectangles represent the observed  $t_b$  calculated with the minima between the bounces. The width of the boxes represent the width of those energy channels, and the height represents the uncertainty from the fit.

1194 is consistent with higher energy peaks returning sooner. This dispersion consistency  
 1195 further supports the assumption that the subsequent peaks are bounces, and not a  
 1196 train of microbursts scattered by bouncing chorus.

1197 To compare the observed and modeled  $t_b$ , we superposed  $t_b$  curves for various  
 1198 models including an analytical solution in a dipole (Schulz and Lanzerotti, 1974), and  
 1199 numerical models: T89, Tsyganenko 2004 (T04) (Tsyganenko and Sitnov, 2005), and  
 1200 Olson & Pfitzer Quiet (Olson and Pfitzer, 1982) in Fig. 3.2. The numerical  $t_b$  curves  
 1201 were calculated using a wrapper for IRBEM-Lib. This code traces the magnetic field  
 1202 line between mirror points, and calculates  $t_b$  assuming conservation of energy and the  
 1203 first adiabatic invariant for electrons mirroring at FIREBIRD-II. With the empirical  
 1204  $t_b$ , the models agree within FIREBIRD-II's uncertainties, but the T04 model has the  
 1205 largest discrepancy compared to the other models.

1206 Microburst Energy Spectra

1207 Next, we investigated the energy spectra of this microburst. The energy spectra  
 1208 was modeled with an exponential that was fit to the peak flux derived from the  
 1209 Gaussian fit parameters in section 3 to all but the highest energy channel. We found  
 1210 that the E-folding energy,  $E_0 \sim 100$  keV. This spectra is similar to spectra show  
 1211 by Lee et al. (2005) from STSAT-1 and Datta et al. (1997) from sounding rocket  
 1212 measurements. The energy spectra is soft for a typical microburst observed with  
 1213 FIREBIRD-II and there was no statistically significant change in  $E_0$  for subsequent  
 1214 bounces.

1215 Microburst Scale Sizes

1216 Lastly, after we applied the time and separation corrections detailed in Appendix  
 1217 B, we mapped the locations of FU3 and FU4 in Fig. 3.3. The locations where FU3 saw  
 1218 peaks 1-5 and where FU4 saw peaks 1-4 are shown as P1-5 and P1-4, respectively.

1219 The lower bound on the latitudinal extent of the microburst was the difference in  
 1220 latitude between P1 on FU3 and P4 on FU4 and was found to be  $29 \pm 1$  km. The  
 1221 uncertainty was estimated from the spacecraft separation uncertainty described in  
 1222 Appendix B. This scale size is the largest reported by FIREBIRD-II.

1223 In section 3, we showed that the observed decaying peaks were likely due to  
 1224 bouncing, so we assume that the observed electrons in subsequent bounces were the  
 1225 drifted electrons from the initial microburst. Under this assumption, the scattered  
 1226 electrons observed in the last bounce by FIREBIRD-II, must have drifted east from  
 1227 their initial scattering longitude, allowing us to calculate the minimum longitudinal  
 1228 scale size. Following geometrical arguments, the distance that electrons drift east in  
 1229 a single bounce is a product of the circumference of the drift shell foot print, and the  
 1230 fraction of the total drift orbit traversed in a single bounce and is given by,

$$d_{az} = 2\pi(R_E + A) \cos(\lambda) \frac{t_b}{\langle T_d \rangle} \quad (3.1)$$

where  $R_E$  is the Earth's radius,  $A$  is the spacecraft altitude,  $\lambda$  is the magnetic latitude,  
 $t_b$  is the electron bounce period, and  $\langle T_d \rangle$  is the electron drift period. Parks (2003)  
derived  $\langle T_d \rangle$  to be,

$$\langle T_d \rangle \approx \begin{cases} 43.8/(L \cdot E) & \text{if } \alpha_0 = 90^\circ \\ 62.7/(L \cdot E) & \text{if } \alpha_0 = 0^\circ \end{cases} \quad (3.2)$$

1231 where  $E$  is the electron energy in MeV,  $L$  is the L shell, and  $\alpha_0$  is the equatorial pitch  
 1232 angle. Electrons mirroring at FIREBIRD-II have  $\alpha_0 \approx 3.7^\circ$  and so the  $\alpha_0 = 0^\circ$  limit  
 1233 was used.

1234 The microburst's longitudinal scale size is defined as the distance the highest  
 1235 energy electrons drifted in the time between the observations of the first and last  
 1236 peaks. This scale size is given by  $D_{az} = n d_{az}$  where  $n$  is the number of bounces

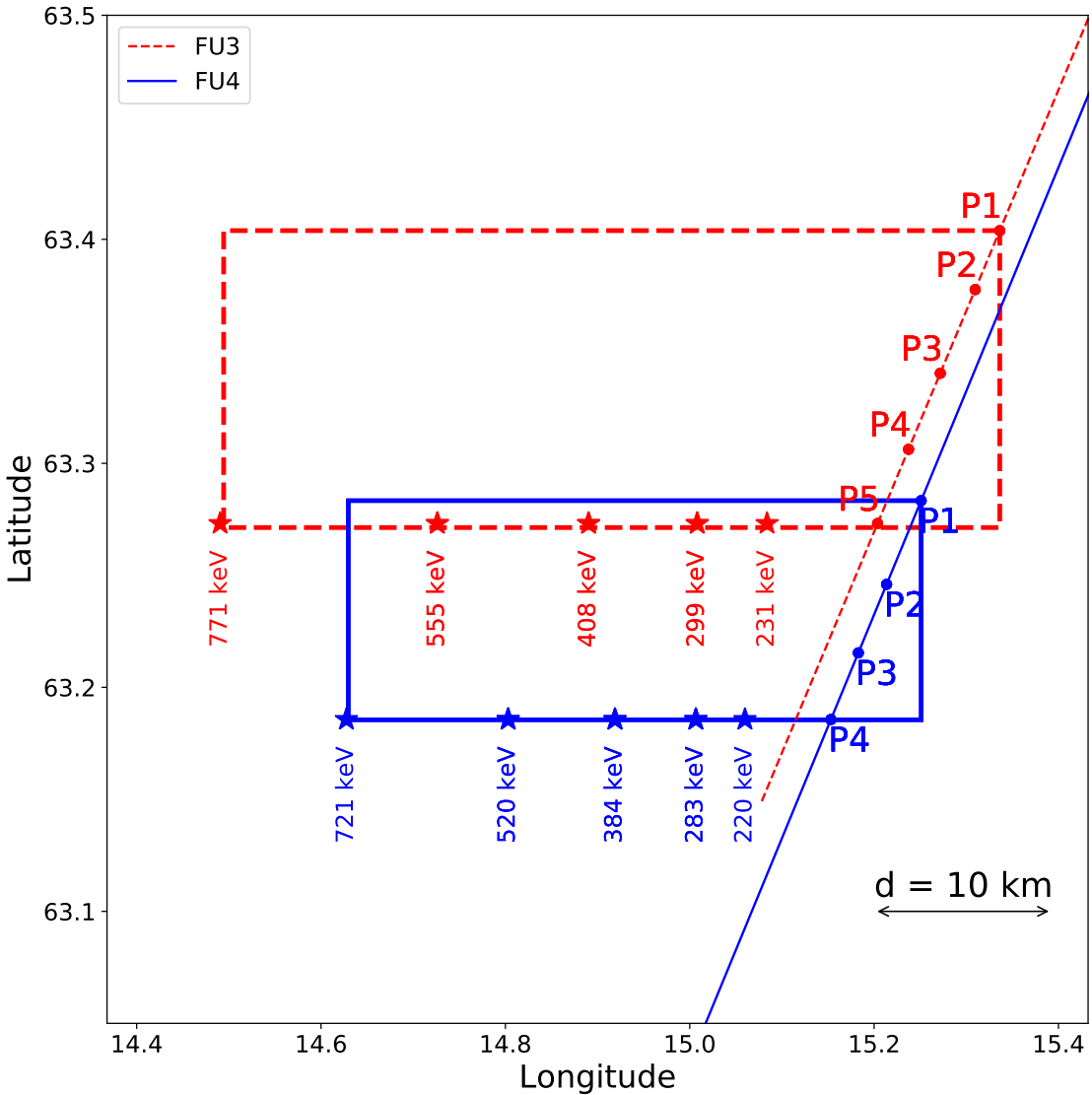


Figure 3.3: The topology of the FIREBIRD-II orbit and the multiple bounces of the microburst projected onto latitude and longitude with axis scaled to equal distance. Attributes relating to FU3 shown in red dashed lines, and FU4 with blue solid lines. The spacecraft path is shown with the diagonal lines, starting at the upper right corner. The labels P1-4 for FU4 and P1-5 for FU3 indicate where the spacecraft were when the  $N^{th}$  peak was seen in the lowest energy channel in the HiRes data. The stars with the accompanying energy labels represent the locations of the electrons with that energy that started at time of P1, and were seen at the last peak on each spacecraft. The rectangles represent the lower bound of the microburst scale size, assuming that the majority of the electrons were in the upper boundary of energy channel 4.

1237 observed. The stars in Fig. 3.3 (with labels corresponding to energy channel  
 1238 boundaries) represent the locations when the microburst was observed at P1, such  
 1239 that an electron of that energy would drift eastward to be seen at P5 for FU3 and P4  
 1240 for FU4. Since FU3 observed more peaks it observed the larger longitudinal scale size  
 1241 which is shown with the red dashed box in Fig. 3.3. FU3's fourth energy channel's  
 1242 bounds are 555 keV and 771 keV, which correspond to longitudinal distances of  $39 \pm 1$   
 1243 km and  $51 \pm 1$ , respectively. The uncertainty was estimated by propagating the  
 1244 uncertainty in the bounce time Eq. 3.1. While the observed minimum longitudinal  
 1245 scale size is dependent on FIREBIRD-II's energy channels, the true scale size may  
 1246 not be.

1247 To investigate how the microburst scale size compares to the scale sizes of chorus  
 1248 waves near the magnetic equator, the microburst's longitudinal and latitudinal scale  
 1249 sizes and their uncertainties in LEO were mapped to the magnetic equator with T89.  
 1250 The radial scale size (latitudinal scale mapped from LEO) was greater than  $500 \pm 10$   
 1251 km. The azimuthal scale size (longitudinal scale mapped from LEO) of 555 keV  
 1252 electrons was greater than  $450 \pm 10$  km and for the 771 keV electrons it was greater  
 1253 than  $530 \pm 10$  km. The lower bound microburst scale size is similar to the chorus  
 1254 scale sizes derived by Agapitov et al. (2017, 2011), and is discussed below.

1255

### Discussion and Conclusions

1256 We presented the first observation of a large microburst with multiple bounces  
 1257 made possible by the twin FIREBIRD-II CubeSats. The microburst's lower bound  
 1258 LEO latitudinal and longitudinal scale sizes of  $29 \pm 1$  km and  $51 \pm 1$  km make  
 1259 it one of the largest observed. The microburst's LEO scale size was larger than  
 1260 the latitudinal scale sizes of typical  $> 1$  MeV microbursts reported in Blake et al.  
 1261 (1996), approximately 10 times larger than reported in Dietrich et al. (2010), and

1262 approximately 2.6 times larger than other simultaneous microbursts observed by  
 1263 FIREBIRD-II (Crew et al., 2016). Lastly, the scale sizes derived here were similar to  
 1264 the scale sizes of  $\sim$  15 keV microbursts observed with a high altitude balloon (Parks,  
 1265 1967). No energy dependence on the minimum latitudinal scale size was observed,  
 1266 while the observed energy dependence of the minimum longitudinal scale size is an  
 1267 artifact of the technique we used to estimate their drift motion.

1268 The microburst scale size obtained in Section 3 and scaled to the geomagnetic  
 1269 equator can be compared with the scales of chorus waves presumably responsible for  
 1270 the rapid burst electron precipitation. Early direct estimates of the chorus source  
 1271 scales were made by the coordinated measurement by ISEE-1, 2. The wave power  
 1272 correlation scale was estimated to be about several hundred kilometers across the  
 1273 background magnetic field (Gurnett et al., 1979). Furthermore, Santolik et al. (2003)  
 1274 determined the correlation lengths of chorus-type whistler waves to be around 100  
 1275 km based on multipoint CLUSTER Wide Band Data measurements near the chorus  
 1276 source region at  $L \approx 4$ , during the magnetic storm of 18 April 2002. Agapitov et al.  
 1277 (2017, 2011, 2010) recently showed that the spatial extent of chorus source region can  
 1278 be larger, ranging from 600 km in the outer radiation belt to more than 1000 km in  
 1279 the outer magnetosphere. The lower bound azimuthal and latitudinal scales obtained  
 1280 in Section 3 and scaled to the magnetic equator, are similar to the whistler-mode  
 1281 chorus source scale sizes reported in Agapitov et al. (2017, 2011).

1282 No wave measurements from nearby spacecraft were available at this time.  
 1283 Nevertheless, during the hours before and after this observation, the Van Allen Probes'  
 1284 (Mauk et al., 2013) Electric and Magnetic Field Instrument and Integrated Science  
 1285 (Kletzing et al., 2013) observed strong wave power in the lower band chorus frequency  
 1286 range, inside the outer radiation belt between 22 and 2 MLT. Furthermore, AE  $\sim 400$   
 1287 nT at this time, and relatively strong chorus waves were statistically more likely to

1288 be present at FIREBIRD-II's MLT (Li et al., 2009b).

1289 The empirically estimated and modeled  $t_b$  in this study agree within FIREBIRD-  
 1290 II's uncertainties, confirming that the energy-dependent dispersion was due to  
 1291 bouncing. The  $t_b$  curves are a proxy for field line length, and this agreement implies  
 1292 that they are comparable. This is expected since the magnetosphere is not drastically  
 1293 compressed at 8 MLT, but we expect a larger discrepancy near midnight, where the  
 1294 magnetosphere is more stretched and difficult to accurately model. In future studies,  
 1295 this analysis can be used as a diagnostic tool to validate field line lengths, and improve  
 1296 magnetic field models.

1297 The similarity of the microburst and chorus source region scale sizes, as well  
 1298 as magnetospheric location and conditions, further support the causal relationship  
 1299 between microbursts and chorus.

1300

### Acknowledgments

1301 This work was made possible with help from the FIREBIRD team, and the  
 1302 members of the Space Sciences and Engineering Laboratory at Montana State  
 1303 University for their hard work to make this mission a success. In addition, M.  
 1304 Shumko acknowledges Drew Turner for his suggestions regarding the bounce period  
 1305 calculations, and Dana Longcope for his proofreading feedback. The FIREBIRD-II  
 1306 data are available at [http://solar.physics.montana.edu/FIREBIRD\\_II/](http://solar.physics.montana.edu/FIREBIRD_II/). This analysis  
 1307 is supported by the National Science Foundation under Grant Numbers 0838034 and  
 1308 1339414. Furthermore, the work of O. Agapitov was supported by the NASA grant  
 1309 NNX16AF85G.

1310

## CHAPTER FOUR

1311

## MICROBURST SIZE DISTRIBUTION DERIVED WITH AEROCUBE-6

1312

Contribution of Authors and Co-Authors

1313 Manuscript(s) in Chapter(s) 1

1314

1315 Author: [type author name here]

1316 Contributions: [list contributions here, single-spaced]

1317 Co-Author: [type co-author name here]

1318 Contributions: [list contributions here, single-spaced]

1319 Co-Author: [type co-author name here]

1320 Contributions: [list contributions here, single-spaced]

1321

1322

Manuscript Information

1323 [Type Author and Co-author(s) Names Here]

1324 Journal of Geophysical Research

1325 Status of Manuscript: **Officially submitted to a peer-reviewed journal**

1326 Wiley

1327

1328

## CONCLUSIONS AND FUTURE WORK

1329

- 1330     1. Microburst scattering mechanism and relation to prior work
- 1331     2. Microburst sizes and the elliptical shape, mention the curtain-microburst  
1332       ambiguity.
- 1333     3. In future work mention how curtains should be studied and outline that project.  
1334       Mention the SAA and amplitude idea.
- 1335     4. Mention REAL and how it plans to look at the microburst flux in PA space.
- 1336     5. Mention BOOMS and how it plans to image microbursts to determine their  
1337       shape without ambiguity.

- 1339 Abel, B. and Thorne, R. M. (1998). Electron scattering loss in earth's inner  
1340 magnetosphere: 1. dominant physical processes. *Journal of Geophysical Research: Space Physics*, 103(A2):2385–2396.
- 1342 Agapitov, O., Blum, L. W., Mozer, F. S., Bonnell, J. W., and Wygant, J. (2017).  
1343 Chorus whistler wave source scales as determined from multipoint van allen probe  
1344 measurements. *Geophysical Research Letters*, pages n/a–n/a. 2017GL072701.
- 1345 Agapitov, O., Krasnoselskikh, V., Dudok de Wit, T., Khotyaintsev, Y., Pickett,  
1346 J. S., Santolik, O., and Rolland, G. (2011). Multispacecraft observations of chorus  
1347 emissions as a tool for the plasma density fluctuations' remote sensing. *Journal of Geophysical Research: Space Physics*, 116(A9):n/a–n/a. A09222.
- 1349 Agapitov, O., Krasnoselskikh, V., Zaliznyak, Y., Angelopoulos, V., Le Contel, O.,  
1350 and Rolland, G. (2010). Chorus source region localization in the earth's outer  
1351 magnetosphere using themis measurements. *Annales Geophysicae*, 28(6):1377–  
1352 1386.
- 1353 Anderson, B., Shekhar, S., Millan, R., Crew, A., Spence, H., Klumpar, D., Blake, J.,  
1354 O'Brien, T., and Turner, D. (2017). Spatial scale and duration of one microburst  
1355 region on 13 August 2015. *Journal of Geophysical Research: Space Physics*.
- 1356 Anderson, K. A. and Milton, D. W. (1964). Balloon observations of X rays in the  
1357 auroral zone: 3. High time resolution studies. *Journal of Geophysical Research*,  
1358 69(21):4457–4479.
- 1359 Barcus, J., Brown, R., and Rosenberg, T. (1966). Spatial and temporal character of  
1360 fast variations in auroral-zone x rays. *Journal of Geophysical Research*, 71(1):125–  
1361 141.
- 1362 Baumjohann, W. and Treumann, R. A. (1997). *Basic space plasma physics*. World  
1363 Scientific.
- 1364 Blake, J., Carranza, P., Claudepierre, S., Clemons, J., Crain, W., Dotan, Y.,  
1365 Fennell, J., Fuentes, F., Galvan, R., George, J., et al. (2013). The magnetic electron  
1366 ion spectrometer (MagEIS) instruments aboard the radiation belt storm probes  
1367 (RBSP) spacecraft. *Space Science Reviews*, 179(1-4):383–421.
- 1368 Blake, J.,Looper, M., Baker, D., Nakamura, R., Klecker, B., and Hovestadt, D.  
1369 (1996). New high temporal and spatial resolution measurements by sampex of the  
1370 precipitation of relativistic electrons. *Advances in Space Research*, 18(8):171 – 186.
- 1371 Blake, J. B. and O'Brien, T. P. (2016). Observations of small-scale latitudinal  
1372 structure in energetic electron precipitation. *Journal of Geophysical Research: Space Physics*, 121(4):3031–3035. 2015JA021815.

- 1374 Blum, L., Li, X., and Denton, M. (2015). Rapid MeV electron precipitation as  
 1375 observed by SAMPEX/HILT during high-speed stream-driven storms. *Journal of*  
 1376 *Geophysical Research: Space Physics*, 120(5):3783–3794. 2014JA020633.
- 1377 Bortnik, J., Thorne, R., and Inan, U. S. (2008). Nonlinear interaction of energetic  
 1378 electrons with large amplitude chorus. *Geophysical Research Letters*, 35(21).
- 1379 Boscher, D., Bourdarie, S., O'Brien, P., Guild, T., and Shumko, M. (2012). Irbem-lib  
 1380 library.
- 1381 Breneman, A., Crew, A., Sample, J., Klumpar, D., Johnson, A., Agapitov, O.,  
 1382 Shumko, M., Turner, D., Santolik, O., Wygant, J., et al. (2017). Observations  
 1383 directly linking relativistic electron microbursts to whistler mode chorus: Van allen  
 1384 probes and FIREBIRD II. *Geophysical Research Letters*.
- 1385 Breneman, A. W., Halford, A., Millan, R., McCarthy, M., Fennell, J., Sample, J.,  
 1386 Woodger, L., Hospodarsky, G., Wygant, J. R., Cattell, C. A., et al. (2015). Global-  
 1387 scale coherence modulation of radiation-belt electron loss from plasmaspheric hiss.  
 1388 *Nature*, 523(7559):193.
- 1389 Brown, R., Barcus, J., and Parsons, N. (1965). Balloon observations of auroral zone  
 1390 x rays in conjugate regions. 2. microbursts and pulsations. *Journal of Geophysical*  
 1391 *Research (U.S.)*.
- 1392 Capannolo, L., Li, W., Ma, Q., Shen, X.-C., Zhang, X.-J., Redmon, R., Rodriguez,  
 1393 J., Engebretson, M., Kletzing, C., Kurth, W., et al. (2019). Energetic electron  
 1394 precipitation: multi-event analysis of its spatial extent during emic wave activity.  
 1395 *Journal of Geophysical Research: Space Physics*.
- 1396 Claudepierre, S., O'Brien, T.,Looper, M., Blake, J., Fennell, J., Roeder, J.,  
 1397 Clemons, J., Mazur, J., Turner, D., Reeves, G., et al. (2019). A revised look  
 1398 at relativistic electrons in the earth's inner radiation zone and slot region. *Journal*  
 1399 *of Geophysical Research: Space Physics*, 124(2):934–951.
- 1400 Comess, M., Smith, D., Selesnick, R., Millan, R., and Sample, J. (2013). Duskside  
 1401 relativistic electron precipitation as measured by sampex: A statistical survey.  
 1402 *Journal of Geophysical Research: Space Physics*, 118(8):5050–5058.
- 1403 Crew, A. B., Spence, H. E., Blake, J. B., Klumpar, D. M., Larsen, B. A., O'Brien,  
 1404 T. P., Driscoll, S., Handley, M., Legere, J., Longworth, S., Mashburn, K.,  
 1405 Mosleh, E., Ryhajlo, N., Smith, S., Springer, L., and Widholm, M. (2016). First  
 1406 multipoint in situ observations of electron microbursts: Initial results from the  
 1407 NSF FIREBIRD II mission. *Journal of Geophysical Research: Space Physics*,  
 1408 121(6):5272–5283. 2016JA022485.

- 1409 Datta, S., Skoug, R., McCarthy, M., and Parks, G. (1997). Modeling of microburst  
 1410 electron precipitation using pitch angle diffusion theory. *Journal of Geophysical*  
 1411 *Research: Space Physics*, 102(A8):17325–17333.
- 1412 Dietrich, S., Rodger, C. J., Clilverd, M. A., Bortnik, J., and Raita, T. (2010).  
 1413 Relativistic microburst storm characteristics: Combined satellite and ground-based  
 1414 observations. *Journal of Geophysical Research: Space Physics*, 115(A12).
- 1415 Douma, E., Rodger, C. J., Blum, L. W., and Clilverd, M. A. (2017). Occurrence  
 1416 characteristics of relativistic electron microbursts from SAMPEX observations.  
 1417 *Journal of Geophysical Research: Space Physics*, 122(8):8096–8107. 2017JA024067.
- 1418 Dungey, J. W. (1961). Interplanetary magnetic field and the auroral zones. *Phys.*  
 1419 *Rev. Lett.*, 6:47–48.
- 1420 Fang, X., Randall, C. E., Lummerzheim, D., Wang, W., Lu, G., Solomon, S. C., and  
 1421 Frahm, R. A. (2010). Parameterization of monoenergetic electron impact ionization.  
 1422 *Geophysical Research Letters*, 37(22).
- 1423 Funsten, H., Skoug, R., Guthrie, A., MacDonald, E., Baldonado, J., Harper, R.,  
 1424 Henderson, K., Kihara, K., Lake, J., Larsen, B., et al. (2013). Helium, Oxygen,  
 1425 Proton, and Electron (HOPE) mass spectrometer for the radiation belt storm  
 1426 probes mission. *Space Science Reviews*, 179(1-4):423–484.
- 1427 Greeley, A., Kanekal, S., Baker, D., Klecker, B., and Schiller, Q. (2019). Quantifying  
 1428 the contribution of microbursts to global electron loss in the radiation belts. *Journal*  
 1429 *of Geophysical Research: Space Physics*.
- 1430 Gurnett, D., Anderson, R., Scarf, F., Fredricks, R., and Smith, E. (1979). Initial  
 1431 results from the isee-1 and-2 plasma wave investigation. *Space Science Reviews*,  
 1432 23(1):103–122.
- 1433 Hendry, A. T., Rodger, C. J., and Clilverd, M. A. (2017). Evidence of sub-mev  
 1434 emic-driven electron precipitation. *Geophysical Research Letters*, 44(3):1210–1218.
- 1435 Hoots, F. R. and Roehrich, R. L. (1980). Models for propagation of norad element  
 1436 sets. Technical Report 3, Spacetrack.
- 1437 Horne, R., Glauert, S., Meredith, N., Boscher, D., Maget, V., Heynderickx, D., and  
 1438 Pitchford, D. (2013). Space weather impacts on satellites and forecasting the earth’s  
 1439 electron radiation belts with spacecast. *Space Weather*, 11(4):169–186.
- 1440 Horne, R., Thorne, R., Meredith, N., and Anderson, R. (2003). Diffuse auroral  
 1441 electron scattering by electron cyclotron harmonic and whistler mode waves during  
 1442 an isolated substorm. *Journal of Geophysical Research: Space Physics*, 108(A7).

- 1443 Horne, R. B. and Thorne, R. M. (2003). Relativistic electron acceleration and  
 1444 precipitation during resonant interactions with whistler-mode chorus. *Geophysical*  
 1445 *Research Letters*, 30(10). 1527.
- 1446 Horne, R. B., Thorne, R. M., Shprits, Y. Y., Meredith, N. P., Glauert, S. A., Smith,  
 1447 A. J., Kanekal, S. G., Baker, D. N., Engebretson, M. J., Posch, J. L., et al.  
 1448 (2005). Wave acceleration of electrons in the van allen radiation belts. *Nature*,  
 1449 437(7056):227.
- 1450 Kasahara, S., Miyoshi, Y., Yokota, S., Mitani, T., Kasahara, Y., Matsuda, S.,  
 1451 Kumamoto, A., Matsuoka, A., Kazama, Y., Frey, H., et al. (2018). Pulsating  
 1452 aurora from electron scattering by chorus waves. *Nature*, 554(7692):337.
- 1453 Kletzing, C., Kurth, W., Acuna, M., MacDowall, R., Torbert, R., Averkamp, T.,  
 1454 Bodet, D., Bounds, S., Chutter, M., Connerney, J., et al. (2013). The electric and  
 1455 magnetic field instrument suite and integrated science (EMFISIS) on RBSP. *Space*  
 1456 *Science Reviews*, 179(1-4):127–181.
- 1457 Klumpar, D., Springer, L., Mosleh, E., Mashburn, K., Berardinelli, S., Gunderson,  
 1458 A., Handly, M., Ryhajlo, N., Spence, H., Smith, S., Legere, J., Widholm, M.,  
 1459 Longworth, S., Crew, A., Larsen, B., Blake, J., and Walmsley, N. (2015). Flight  
 1460 system technologies enabling the twin-cubesat firebird-ii scientific mission.
- 1461 Lee, J. J., Parks, G. K., Lee, E., Tsurutani, B. T., Hwang, J., Cho, K. S., Kim, K.-H.,  
 1462 Park, Y. D., Min, K. W., and McCarthy, M. P. (2012). Anisotropic pitch angle  
 1463 distribution of 100 keV microburst electrons in the loss cone: measurements from  
 1464 STSAT-1. *Annales Geophysicae*, 30(11):1567–1573.
- 1465 Lee, J.-J., Parks, G. K., Min, K. W., Kim, H. J., Park, J., Hwang, J., McCarthy,  
 1466 M. P., Lee, E., Ryu, K. S., Lim, J. T., Sim, E. S., Lee, H. W., Kang, K. I., and  
 1467 Park, H. Y. (2005). Energy spectra of 170–360 keV electron microbursts measured  
 1468 by the korean STSAT-1. *Geophysical Research Letters*, 32(13). L13106.
- 1469 Li, W., Thorne, R., Angelopoulos, V., Bonnell, J., McFadden, J., Carlson, C.,  
 1470 LeContel, O., Roux, A., Glassmeier, K., and Auster, H. (2009a). Evaluation of  
 1471 whistler-mode chorus intensification on the nightside during an injection event  
 1472 observed on the THEMIS spacecraft. *Journal of Geophysical Research: Space*  
 1473 *Physics*, 114(A1).
- 1474 Li, W., Thorne, R., Bortnik, J., Tao, X., and Angelopoulos, V. (2012). Characteristics  
 1475 of hiss-like and discrete whistler-mode emissions. *Geophysical Research Letters*,  
 1476 39(18).
- 1477 Li, W., Thorne, R. M., Angelopoulos, V., Bortnik, J., Cully, C. M., Ni, B., LeContel,  
 1478 O., Roux, A., Auster, U., and Magnes, W. (2009b). Global distribution of whistler-  
 1479 mode chorus waves observed on the THEMIS spacecraft. *Geophysical Research*  
 1480 *Letters*, 36(9). L09104.

- 1481 Li, X., Selesnick, R., Schiller, Q., Zhang, K., Zhao, H., Baker, D. N., and Temerin,  
 1482 M. A. (2017). Measurement of electrons from albedo neutron decay and neutron  
 1483 density in near-earth space. *Nature*, 552(7685):382.
- 1484 Lorentzen, K. R., Blake, J. B., Inan, U. S., and Bortnik, J. (2001a). Observations  
 1485 of relativistic electron microbursts in association with VLF chorus. *Journal of*  
 1486 *Geophysical Research: Space Physics*, 106(A4):6017–6027.
- 1487 Lorentzen, K. R.,Looper, M. D., and Blake, J. B. (2001b). Relativistic electron  
 1488 microbursts during the GEM storms. *Geophysical Research Letters*, 28(13):2573–  
 1489 2576.
- 1490 Lyons, L. R. and Thorne, R. M. (1973). Equilibrium structure of radiation belt  
 1491 electrons. *Journal of Geophysical Research*, 78(13):2142–2149.
- 1492 Manweiler, J. W. and Zwiener, H. M. (2018). Science Operations Center (SOC)  
 1493 RBSPICE Science Data Handbook Revision: e. Technical report, Fundamental  
 1494 Technologies, LLC.
- 1495 Mauk, B., Fox, N. J., Kanekal, S., Kessel, R., Sibeck, D., and Ukhorskiy, A. (2013).  
 1496 Science objectives and rationale for the radiation belt storm probes mission. *Space*  
 1497 *Science Reviews*, 179(1-4):3–27.
- 1498 Meredith, N., Horne, R., Summers, D., Thorne, R., Iles, R., Heynderickx, D., and  
 1499 Anderson, R. (2002). Evidence for acceleration of outer zone electrons to relativistic  
 1500 energies by whistler mode chorus. In *Annales Geophysicae*, volume 20, pages 967–  
 1501 979.
- 1502 Millan, R. and Thorne, R. (2007). Review of radiation belt relativistic electron losses.  
 1503 *Journal of Atmospheric and Solar-Terrestrial Physics*, 69(3):362 – 377.
- 1504 Millan, R. M., Lin, R., Smith, D., Lorentzen, K., and McCarthy, M. (2002). X-  
 1505 ray observations of mev electron precipitation with a balloon-borne germanium  
 1506 spectrometer. *Geophysical research letters*, 29(24).
- 1507 Mitchell, D., Lanzerotti, L., Kim, C., Stokes, M., Ho, G., Cooper, S., Ukhorskiy, A.,  
 1508 Manweiler, J., Jaskulek, S., Haggerty, D., et al. (2013). Radiation belt storm probes  
 1509 ion composition experiment (RBSPICE). *Space Science Reviews*, 179(1-4):263–308.
- 1510 Mozer, F. S., Agapitov, O. V., Blake, J. B., and Vasko, I. Y. (2018). Simultaneous  
 1511 observations of lower band chorus emissions at the equator and microburst  
 1512 precipitating electrons in the ionosphere. *Geophysical Research Letters*.
- 1513 Nakamura, R., Baker, D. N., Blake, J. B., Kanekal, S., Klecker, B., and Hovestadt,  
 1514 D. (1995). Relativistic electron precipitation enhancements near the outer edge of  
 1515 the radiation belt. *Geophysical Research Letters*, 22(9):1129–1132.

- 1516 Nakamura, R., Isowa, M., Kamide, Y., Baker, D., Blake, J., and Looper, M. (2000).  
 1517 Observations of relativistic electron microbursts in association with VLF chorus.  
 1518 *J. Geophys. Res.*, 105:15875–15885.
- 1519 Nishimura, Y., Bortnik, J., Li, W., Thorne, R., Chen, L., Lyons, L., Angelopoulos,  
 1520 V., Mende, S., Bonnell, J., Le Contel, O., et al. (2011). Multievent study of the  
 1521 correlation between pulsating aurora and whistler mode chorus emissions. *Journal*  
 1522 *of Geophysical Research: Space Physics*, 116(A11).
- 1523 O'Brien, T., Claudepierre, S., Blake, J., Fennell, J. F., Clemons, J., Roeder, J.,  
 1524 Spence, H. E., Reeves, G., and Baker, D. (2014). An empirically observed pitch-  
 1525 angle diffusion eigenmode in the earth's electron belt near  $\lambda^* = 5.0$ . *Geophysical*  
 1526 *Research Letters*, 41(2):251–258.
- 1527 O'Brien, T., Claudepierre, S., Guild, T., Fennell, J., Turner, D., Blake, J., Clemons,  
 1528 J., and Roeder, J. (2016). Inner zone and slot electron radial diffusion revisited.  
 1529 *Geophysical Research Letters*, 43(14):7301–7310.
- 1530 O'Brien, T. and Moldwin, M. (2003). Empirical plasmapause models from magnetic  
 1531 indices. *Geophysical Research Letters*, 30(4).
- 1532 O'Brien, T. P., Looper, M. D., and Blake, J. B. (2004). Quantification of relativistic  
 1533 electron microburst losses during the GEM storms. *Geophysical Research Letters*,  
 1534 31(4). L04802.
- 1535 O'Brien, T. P., Lorentzen, K. R., Mann, I. R., Meredith, N. P., Blake, J. B., Fennell,  
 1536 J. F., Looper, M. D., Milling, D. K., and Anderson, R. R. (2003). Energization of  
 1537 relativistic electrons in the presence of ULF power and MeV microbursts: Evidence  
 1538 for dual ULF and VLF acceleration. *Journal of Geophysical Research: Space*  
 1539 *Physics*, 108(A8).
- 1540 Olson, W. P. and Pfitzer, K. A. (1982). A dynamic model of the magnetospheric  
 1541 magnetic and electric fields for july 29, 1977. *Journal of Geophysical Research:*  
 1542 *Space Physics*, 87(A8):5943–5948.
- 1543 Ozaki, M., Miyoshi, Y., Shiokawa, K., Hosokawa, K., Oyama, S.-i., Kataoka, R.,  
 1544 Ebihara, Y., Ogawa, Y., Kasahara, Y., Yagitani, S., et al. (2019). Visualization of  
 1545 rapid electron precipitation via chorus element wave-particle interactions. *Nature*  
 1546 *communications*, 10(1):257.
- 1547 Ozaki, M., Yagitani, S., Ishizaka, K., Shiokawa, K., Miyoshi, Y., Kadokura, A.,  
 1548 Yamagishi, H., Kataoka, R., Ieda, A., Ebihara, Y., Sato, N., and Nagano, I. (2012).  
 1549 Observed correlation between pulsating aurora and chorus waves at Syowa Station  
 1550 in Antarctica: A case study. *Journal of Geophysical Research: Space Physics*,  
 1551 117(A8).

- 1552 Parks, G. (2003). *Physics Of Space Plasmas: An Introduction, Second Edition.*  
 1553 Westview Press.
- 1554 Parks, G. K. (1967). Spatial characteristics of auroral-zone X-ray microbursts. *Journal  
 1555 of Geophysical Research*, 72(1):215–226.
- 1556 Reeves, G., Spence, H. E., Henderson, M., Morley, S., Friedel, R., Funsten, H., Baker,  
 1557 D., Kanekal, S., Blake, J., Fennell, J., et al. (2013). Electron acceleration in the  
 1558 heart of the van allen radiation belts. *Science*, 341(6149):991–994.
- 1559 Reeves, G. D., McAdams, K. L., Friedel, R. H. W., and O'Brien, T. P. (2003). Ac-  
 1560 celeration and loss of relativistic electrons during geomagnetic storms. *Geophysical  
 1561 Research Letters*, 30(10):n/a–n/a. 1529.
- 1562 Santolik, O., Gurnett, D., Pickett, J., Parrot, M., and Cornilleau-Wehrlin, N. (2003).  
 1563 Spatio-temporal structure of storm-time chorus. *Journal of Geophysical Research:  
 1564 Space Physics*, 108(A7).
- 1565 Santolk, O., Parrot, M., and Lefevre, F. (2003). Singular value decomposition  
 1566 methods for wave propagation analysis. *Radio Science*, 38(1):n/a–n/a. 1010.
- 1567 Schulz, M. and Lanzerotti, L. J. (1974). *Particle Diffusion in the Radiation Belts.*  
 1568 Springer.
- 1569 Selesnick, R. S., Blake, J. B., and Mewaldt, R. A. (2003). Atmospheric losses of  
 1570 radiation belt electrons. *Journal of Geophysical Research: Space Physics*, 108(A12).  
 1571 1468.
- 1572 Shprits, Y. Y., Meredith, N. P., and Thorne, R. M. (2007). Parameterization  
 1573 of radiation belt electron loss timescales due to interactions with chorus waves.  
 1574 *Geophysical Research Letters*, 34(11):n/a–n/a. L11110.
- 1575 Shprits, Y. Y. and Thorne, R. M. (2004). Time dependent radial diffusion modeling  
 1576 of relativistic electrons with realistic loss rates. *Geophysical Research Letters*,  
 1577 31(8):n/a–n/a. L08805.
- 1578 Spence, H. E., Blake, J. B., Crew, A. B., Driscoll, S., Klumpar, D. M., Larsen,  
 1579 B. A., Legere, J., Longworth, S., Mosleh, E., O'Brien, T. P., Smith, S., Springer,  
 1580 L., and Widholm, M. (2012). Focusing on size and energy dependence of electron  
 1581 microbursts from the van allen radiation belts. *Space Weather*, 10(11).
- 1582 Summers, D., Thorne, R. M., and Xiao, F. (1998). Relativistic theory of wave-particle  
 1583 resonant diffusion with application to electron acceleration in the magnetosphere.  
 1584 *Journal of Geophysical Research: Space Physics*, 103(A9):20487–20500.

- 1585 Takahashi, K. and Denton, R. E. (2007). Magnetospheric seismology using multi-  
 1586 harmonic toroidal waves observed at geosynchronous orbit. *Journal of Geophysical*  
 1587 *Research: Space Physics*, 112(A5).
- 1588 Thorne, R. M. (2010). Radiation belt dynamics: The importance of wave-particle  
 1589 interactions. *Geophysical Research Letters*, 37(22). L22107.
- 1590 Thorne, R. M. and Andreoli, L. J. (1981). *Mechanisms for Intense Relativistic*  
 1591 *Electron Precipitation*, pages 381–394. Springer Netherlands, Dordrecht.
- 1592 Thorne, R. M., O'Brien, T. P., Shprits, Y. Y., Summers, D., and Horne, R. B. (2005).  
 1593 Timescale for MeV electron microburst loss during geomagnetic storms. *Journal*  
 1594 *of Geophysical Research: Space Physics*, 110(A9). A09202.
- 1595 Trefall, H., Bjordal, J., Ullaland, S., and Stadsnes, J. (1966). On the extension of  
 1596 auroral-zone x-ray microbursts. *Journal of Atmospheric and Terrestrial Physics*,  
 1597 28(2):225–233.
- 1598 Tsurutani, B. T. and Lakhina, G. S. (1997). Some basic concepts of wave-particle  
 1599 interactions in collisionless plasmas. *Reviews of Geophysics*, 35(4):491–501.
- 1600 Tsyganenko, N. (1989). A solution of the chapman-ferraro problem for an ellipsoidal  
 1601 magnetopause. *Planetary and Space Science*, 37(9):1037 – 1046.
- 1602 Tsyganenko, N. A. and Sitnov, M. I. (2005). Modeling the dynamics of the inner  
 1603 magnetosphere during strong geomagnetic storms. *Journal of Geophysical Research:*  
 1604 *Space Physics*, 110(A3).
- 1605 Turner, D., Claudepierre, S., Fennell, J., O'Brien, T., Blake, J., Lemon, C.,  
 1606 Gkioulidou, M., Takahashi, K., Reeves, G., Thaller, S., et al. (2015). Energetic  
 1607 electron injections deep into the inner magnetosphere associated with substorm  
 1608 activity. *Geophysical Research Letters*, 42(7):2079–2087.
- 1609 Ukhorskiy, A. Y., Anderson, B. J., Brandt, P. C., and Tsyganenko, N. A. (2006).  
 1610 Storm time evolution of the outer radiation belt: Transport and losses. *Journal of*  
 1611 *Geophysical Research: Space Physics*, 111(A11):n/a–n/a. A11S03.
- 1612 Van Allen, J. A. (1959). The geomagnetically trapped corpuscular radiation. *Journal*  
 1613 *of Geophysical Research*, 64(11):1683–1689.
- 1614 Vernov, S. and Chudakov, A. (1960). Investigation of radiation in outer space. In  
 1615 *International Cosmic Ray Conference*, volume 3, page 19.
- 1616 Walker, A. D. M. (1993). *Plasma waves in the magnetosphere*, volume 24. Springer  
 1617 Science & Business Media.

- 1618 Woodger, L., Halford, A., Millan, R., McCarthy, M., Smith, D., Bowers, G., Sample,  
1619 J., Anderson, B., and Liang, X. (2015). A summary of the BARREL campaigns:  
1620 Technique for studying electron precipitation. *Journal of Geophysical Research:*  
1621 *Space Physics*, 120(6):4922–4935.

## APPENDIX: APPENDIX A

1623 This appendix contains Figs. A.1 and A.2. Figure A.1 shows evidence that  
1624 supports our claim that the “hiss-like” chorus wave observed at 11:17:03 UT with  
1625 EMFISIS WFR instrument on RBSP-A was parallel propagating. The polar angle  
1626 of the wave vector and the supporting planarity of the magnetic field polarization  
1627 shown in Fig. A.1 was calculated using the singular value decomposition (SVD)  
1628 method (Santolk et al., 2003).

1629 Figure A.2 supports the claim that RBSPICE-A observed a 10-80% increase in  
1630 the count rates at the microburst times and pitch angles. Figure A.2 shows the ratio  
1631 of the RBSPICE-A’s EBR count rates during the four microbursts to the quiet time  
1632 one spin before, at the same pitch angles.

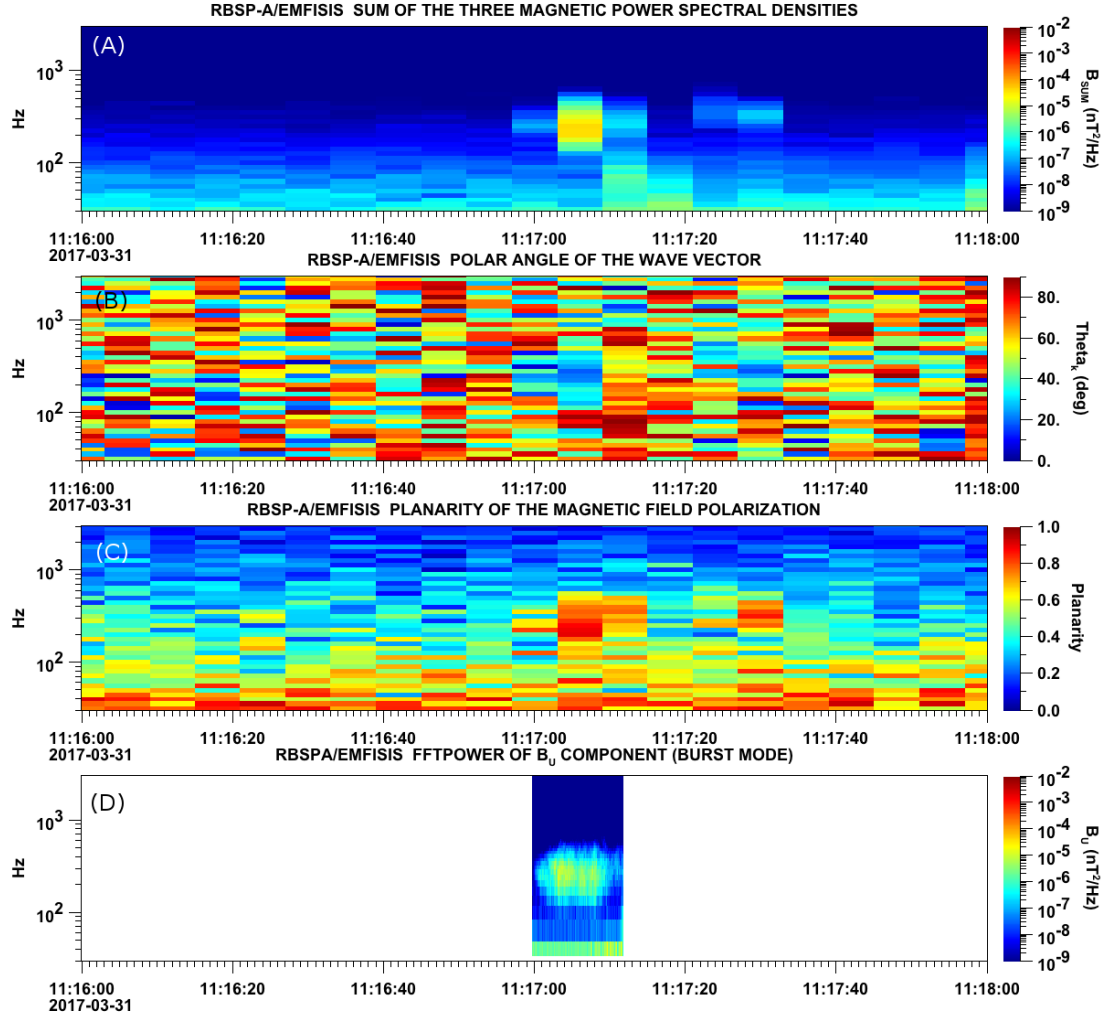


Figure A.1: Panel (A) shows the magnetic power spectral density as a function of frequency and time from the EMFISIS WFR instrument on board RBSP-A. The “hiss-like” wave used for the resonant diffusion analysis was observed starting at 11:17:03 UT. In the same format as panel (A), panel (B) shows the polar angle of the wave vector for this time period. The wave of interest had a normal wave vector,  $\theta_k < 30^\circ$ . Since the results in panel (B) are valid only for high planarity, panel (C) shows planarity in the same format as panels (A) and (B). The wave of interest was found to have a planarity of  $> 0.8$ . Lastly, panel (D) shows the available burst mode data.

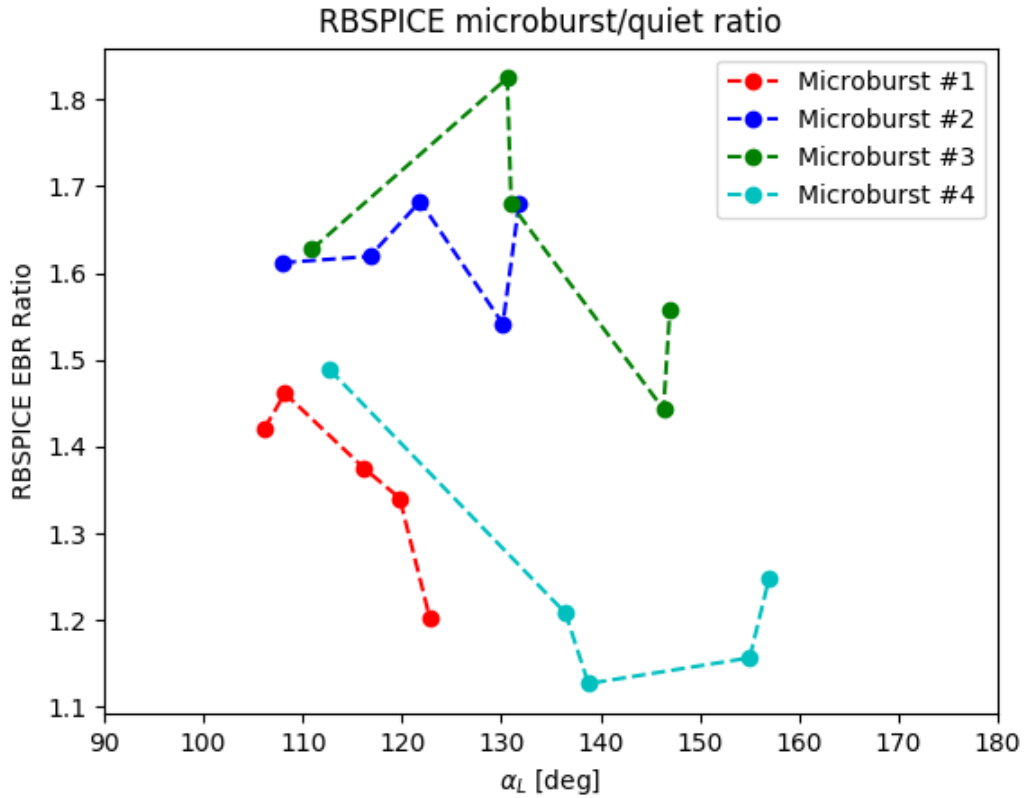


Figure A.2: Ratio of the RBSPICE EBR at microburst times indicated with the black vertical arrows in Fig. 2, to the EBR at the same pitch angles one spin prior (quiet time). The microburst flux was enhanced by 10-80% across  $100^\circ < \alpha_L < 160^\circ$  PA, and appear to be peaked closer to  $\alpha_L = 90^\circ$ .

1633

## APPENDIX: APPENDIX B

1634 This appendix describes the method we used to calculate the time difference and  
 1635 separation between FU3 and FU4 at 06:12 UT on February 2nd, 2015. We used the  
 1636 following method to calculate the clock difference,  $\delta t_c$  and separation,  $d$  between FU3  
 1637 and FU4 at 06:12 UT on February 2nd, 2015.

1638 The relative clock difference was calculated with a cross-correlation time  
 1639 lag analysis on uniquely-identified trains of microbursts that hit both spacecraft  
 1640 simultaneously. Four time periods with coincident microbursts were hand-picked on  
 1641 February 2nd, 2015 and are shown in Figs. B.1-B.4, panels (a) and (b). The cross-  
 1642 correlation time lag analysis was applied to the HiRes time series in panels (a) and  
 1643 (b), and the resulting normalized cross-correlation coefficient as a function of time is  
 1644 shown in panel (c). To validate the peak lag identified in panel (c), FU3's time series  
 1645 was shifted by that lag and is shown in panel (d).

1646 The clock differences from the simultaneous microbursts in Figs. B.1-B.4 were  
 1647 linearly fit to account for the relative clock drift ( $\approx 20$  ms/hour at this time), giving  
 1648 a value of  $\delta t_c = 2.28 \pm 0.12$  s at the time of the microburst analyzed here. This time  
 1649 shift was applied to the HiRes data in Fig. 1. A clock difference of  $\delta t_c = 2.45^{+0.51}_{-0.98}$  s  
 1650 was independently calculated with the FIREBIRD-II telemetry beacon time stamps  
 1651 that were downlinked during operational passes.

1652 We calculate the spacecraft separation, by applying same the cross-correlation  
 1653 time lag analysis on structures assumed to be spatial and are shown in Figs. B.5  
 1654 and B.6. The lag from the peak cross-correlation between these events is a sum of  
 1655 the clock difference and time lag due to the spacecraft separation. We interpret the  
 1656 time lag due to the spacecraft separation as the time difference between when the  
 1657 leading satellite observed a stationary spatial feature, to when the trailing satellite  
 1658 observed the same stationary spatial feature. With the method described above, we  
 1659 find the spatial time lag to be  $\delta t_d = 2.64 \pm 0.12$  s (after we account for the clock  
 1660 difference and its uncertainty). To convert from a spatial time lag to a spacecraft  
 1661 separation, we calculate the satellite velocity. We calculate the velocity using a Two  
 1662 Line Element (TLE), a data format containing the orbit parameters that are used  
 1663 for orbit propagation. With the TLE derived spacecraft velocity,  $v = 7.57$  km/s, the  
 1664 spacecraft separation was  $d = 19.9 \pm 0.9$  km.

1665 An independent method to calculate the spacecraft separation was developed.  
 1666 The separation was calculated using TLEs. The TLE from February 2nd was  
 1667 anomalous and was not used in this analysis. Instead, seven TLEs released up to  
 1668 five days after the microburst event were backpropagated, using the SGP-4 algorithm  
 1669 (Hoots and Roehrich, 1980) that calculates orbital state vectors with perturbations  
 1670 such as Earth's atmosphere, as well as gravitational effects from the moon and sun.  
 1671 Then the predicted spacecraft separations at the time of the microburst event were

<sub>1672</sub> averaged to derive a separation of  $d = 18.4 \pm 1.5$  km. These two methods give  
<sub>1673</sub> similar separations, which implies that the stationary event assumption used in the  
<sub>1674</sub> cross-correlation time lag analysis is reasonable.

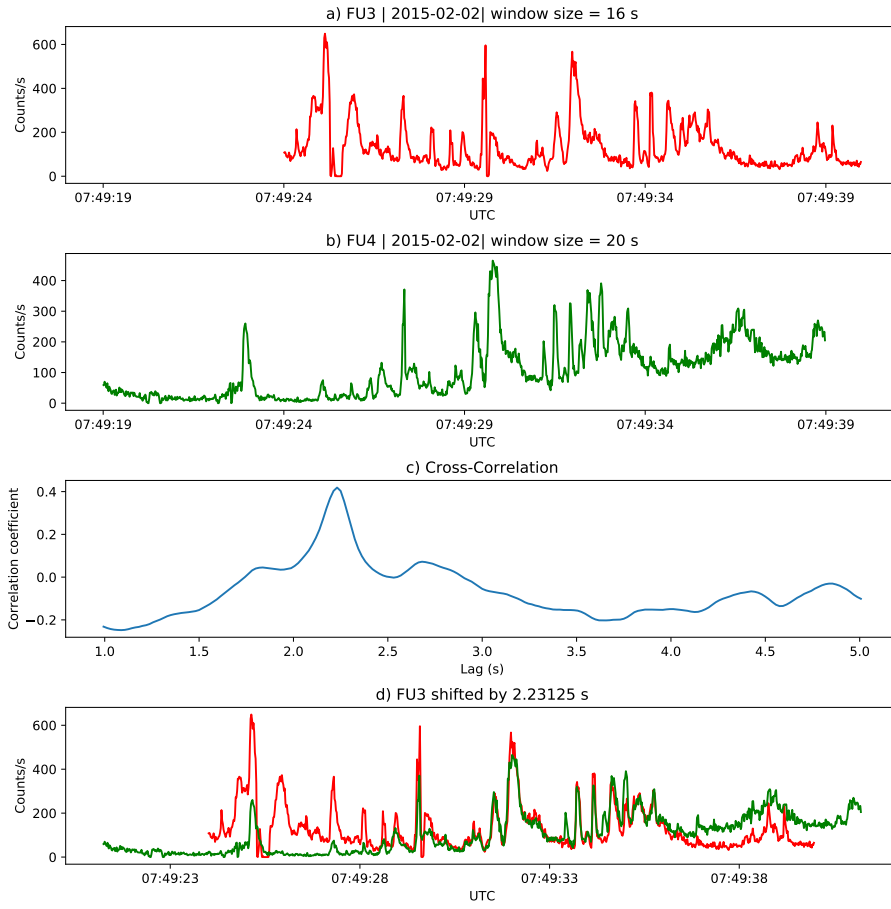


Figure B.1: Cross-correlation time lag analysis applied to a train of microbursts. Panel (a) and (b) show the count rate from the lowest energy channel. Panel (c) shows the cross-correlation coefficient as a function of time lag. Panel (d) shows the shifted timeseries. Clock difference was 2.23 s.

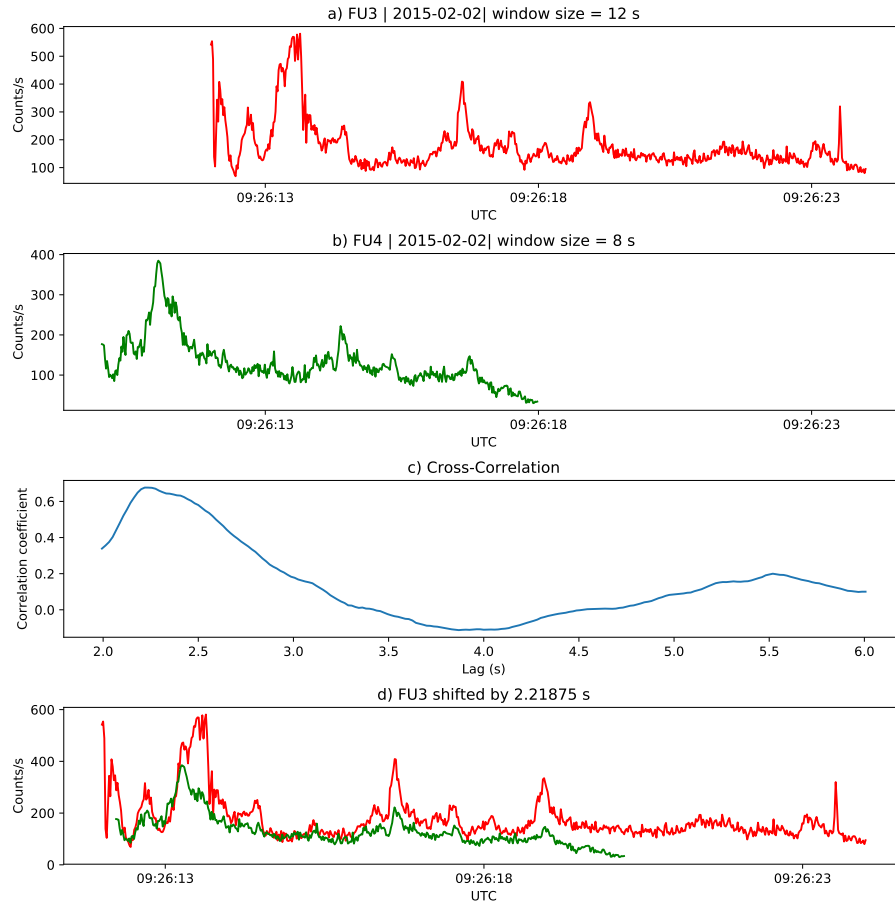


Figure B.2: Same analysis as Fig. B.1 on a different time period. Clock difference was 2.21 s.

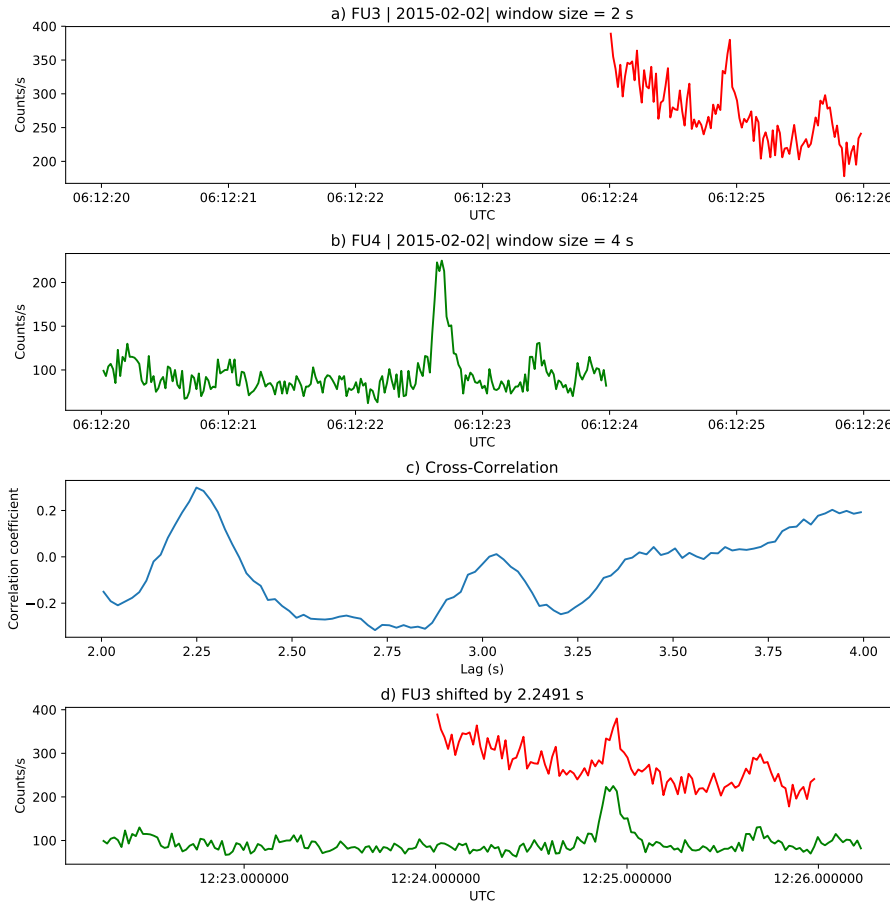


Figure B.3: Same analysis as Fig. B.1 on a different time period. Clock difference was 2.25 s.

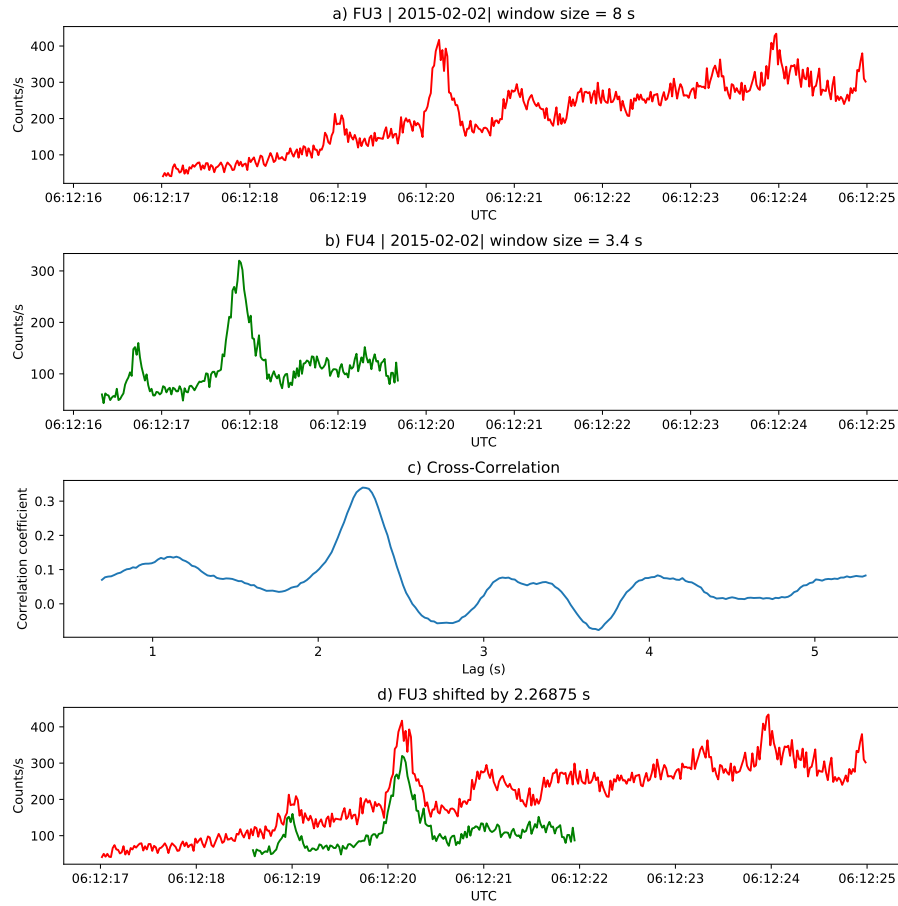


Figure B.4: Same analysis as Fig. B.1 on a different time period. Clock difference was 2.27 s.

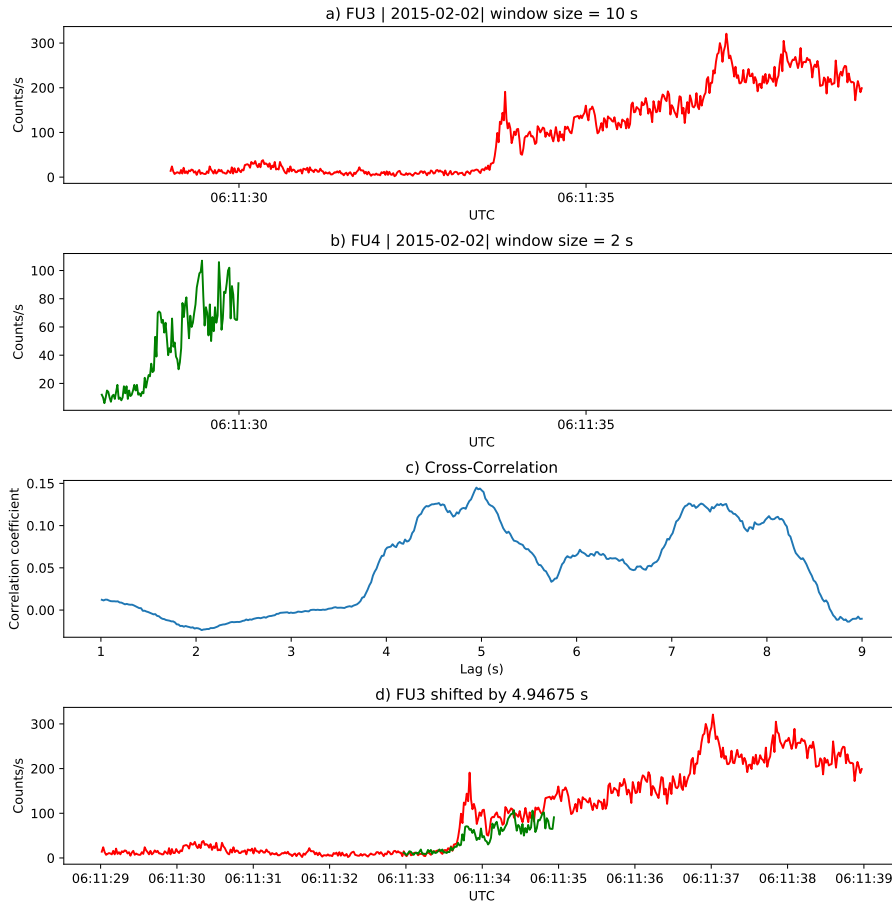


Figure B.5: Same cross-correlation time lag analysis applied to stationary spatial structures. The cross-correlation lag between these events is a sum of the clock difference and time lag due to the spacecraft separation. The lag derived at this time was 4.95 s.

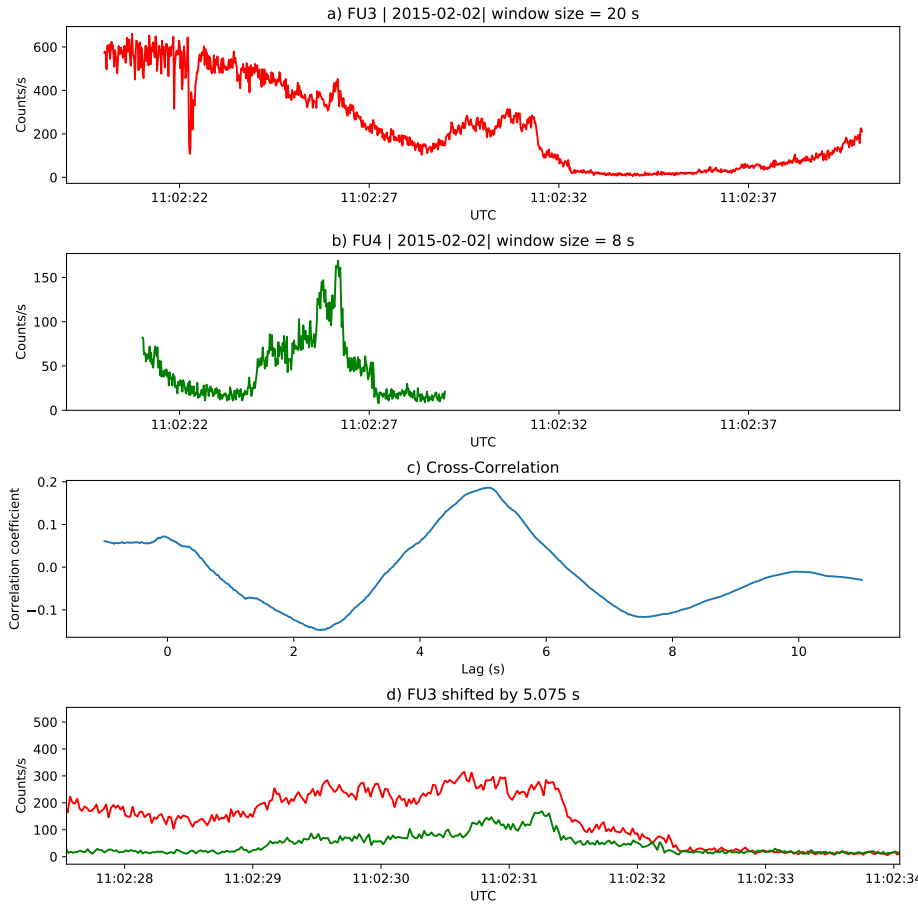


Figure B.6: Same analysis as Fig. B.5 applied to a different stationary spatial feature. The lag derived at this time was 5.01 s.